

GRADUATE AERONAUTICAL LABORATORIES
CALIFORNIA INSTITUTE of TECHNOLOGY
Pasadena, California 91125

Chemical Reactions in Turbulent Mixing Flows

Paul E. Dimotakis* and Anthony Leonard**

Air Force Office of Scientific Research
Grant No. F949620-92-J-0290

Annual Technical Report: Period ending 31 May 1993

15 July 1993

* Professor, Aeronautics & Applied Physics.

** Professor, Aeronautics.

REPORT DOCUMENTATION PAGE

Form Approved
OMB No. 0704-0188

Public reporting burden for this collection of information is estimated to average 1 hour per response, including the time for reviewing instructions, searching existing data sources, gathering and maintaining the data needed, and completing and reviewing the collection of information. Send comments regarding this burden estimate or any other aspect of this collection of information, including suggestions for reducing this burden, to Washington Headquarters Services, Directorate for Information Operations and Reports, 1215 Jefferson Davis Highway, Suite 1204, Arlington, VA 22202-4302, and to the Office of Management and Budget, Paperwork Reduction Project (0704-0188), Washington, DC 20503.

1. AGENCY USE ONLY (Leave blank)		2. REPORT DATE 15 July 1993	3. REPORT TYPE AND DATES COVERED Annual Technical Report: 1June92-31May93	
4. TITLE AND SUBTITLE Chemical Reactions in Turbulent Mixing Flows			5. FUNDING NUMBERS PE - 61102F PR - 2308 SA - BS G - F949620-92-J-0290	
6. AUTHOR(S) Paul E. Dimotakis Anthony Leonard				
7. PERFORMING ORGANIZATION NAME(S) AND ADDRESS(ES) California Institute of Technology 1201 E. California Blvd., MC 301-46 Pasadena, CA 91125			8. PERFORMING ORGANIZATION REPORT NUMBER	
9. SPONSORING/MONITORING AGENCY NAME(S) AND ADDRESS(ES) AFOSR/NA Building 410 Bolling AFB DC 20332-6448			10. SPONSORING/MONITORING AGENCY REPORT NUMBER	
11. SUPPLEMENTARY NOTES				
12a. DISTRIBUTION/AVAILABILITY STATEMENT Approved for public release; distribution is unlimited			12b. DISTRIBUTION CODE	
13. ABSTRACT (Maximum 200 words) In the course of this research we have conducted investigations of turbulent mixing, chemical reaction and combustion processes in turbulent, subsonic and supersonic flows. The program was comprised of several parts: (i) an experimental effort, (ii) a theoretical and numerical simulation effort, and (iii) a development of instrumentation and diagnostics; an upgrade of flow and combustion facilities; and the development of data-acquisition sub-systems. We have carried out a series of theoretical and experimental studies of turbulent mixing in primarily in two, well-defined, fundamentally important flow fields: free-shear layers and axisymmetric jets. To elucidate molecular transport effects, experiments and theory have dealt with both reacting and non-reacting flows of liquids and gases, in fully-developed turbulent flows. A criterion for fully-developed turbulence was recently developed. The computational studies are, at present, focused at fundamental formulation and implementation issues pertaining to the simulation of both compressible and incompressible flows characterized by strong fronts, such as shock waves and flames. In our diagnostic development efforts we have improved the signal-to-noise ratio of flow images, in both gas- and liquid-phase flows, as well as continued with the development of data-acquisition electronics to meet very high-speed, high-volume data requirements; the acquisition of single, or pairs, of two-dimensional images in rapid succession; and the acquisition of data from arrays of supersonic flow sensors.				
14. SUBJECT TERMS: Turbulent mixing, supersonic turbulence, shear layers, jets, turbulent mixing transition, image correlation velocimetry, heat release effects, turbulent diffusion flames.			15. NUMBER OF PAGES 132	
			16. PRICE CODE	
17. SECURITY CLASSIFICATION OF REPORT Unclassified	18. SECURITY CLASSIFICATION OF THIS PAGE Unclassified	19. SECURITY CLASSIFICATION OF ABSTRACT Unclassified	20. LIMITATION OF ABSTRACT UL	

Abstract

The purpose of this research is to conduct fundamental investigations of turbulent mixing, chemical reaction and combustion processes in turbulent, subsonic and supersonic flows. The program during this reporting period was comprised of several parts:

- a. an experimental effort,
- b. a numerical simulation effort,

and

- c. an effort to develop instrumentation and diagnostics; flow and combustion facilities; and data-acquisition systems.

The latter as dictated by the specific needs of the experimental part of the program.

Our approach in this research has been to carry out a series of detailed theoretical and experimental studies of turbulent mixing in primarily in two, well-defined, fundamentally important flow fields: free-shear layers and axisymmetric jets. To elucidate molecular transport effects, experiments and theory concern themselves with both reacting and non-reacting flows of liquids and gases, in fully-developed turbulent flows, *i.e.*, in moderate to high Reynolds number flows. A criterion for fully-developed turbulence was recently developed and will be presented below.

The computational studies are, at present, focused at fundamental formulation and implementation issues pertaining to the computational simulation of both compressible and incompressible flows characterized by strong fronts, such as shock waves and flames.

Our diagnostic development efforts have recently been focused on improving the signal-to-noise ratio of flow images, in both gas- and liquid-phase flows, as well as the continuing development of data-acquisition electronics to meet very high-speed, high-volume data requirements; the acquisition of single, or pairs, of two-dimensional images in rapid succession; and the acquisition of data from arrays of supersonic flow sensors.

1. Introduction

Progress made under the sponsorship of this Grant, for the period ending 31 May 1993, has taken place in several focus areas. This is discussed in the corresponding sections below. Additional documentation can be found in the recent reports and publications included as appendices to this report, as well as in the reference list (Sec. 8). Additional copies of any of this material are available on request.

Work in preliminary stages, at this writing, and not documented in the discussion below, includes:

- a. progress and advances in signal-to-noise ratio in gas-phase, supersonic-flow imaging;[†]
- b. calculations and design for an upgrade of the Supersonic Shear Layer (S³L) combustion facility scheduled during the next twelve months;
- c. an analytical effort to understand mixed (super-/sub-sonic) flow;

and

- d. advances in computer-aided-design and fabrication of electronic circuitry.

Parts of this effort were cosponsored by an ARPA/ONR contract, the Gas Research Institute, and JPL.

[†] Related work in liquid-phase jets is discussed in Sec. 4.2.

2. A criterion for fully-developed turbulence

Recent data on turbulent mixing suggest that the mixing transition, previously documented to occur in shear layers, also occurs in the far field ($x/d > 30$) of turbulent jets, as well as other flows. Specifically, a transition to a more well-mixed state has been observed experimentally in,

- a. pipe flow,
- b. in the near-field ($x/d < 15$) of round jets,
- c. in cylinder wakes,
- d. in grid turbulence,
- e. in thermal convection,
- f. in Couette-Taylor flow (between concentric cylinders),

as well as

- g. in recent numerical simulations of turbulence in a spatially periodic cube.

The resulting, fully-developed turbulent flow requires a minimum Reynolds number of $Re \approx 10^4$, or a minimum Taylor Reynolds number of $Re_T \approx 10^2$, to be sustained. The transition itself must be regarded as a more-or-less universal phenomenon.

Turbulent mixing in this fully-developed state does not appear to be universal, however, with a qualitatively different behavior between shear layers and jets. See also discussion in Miller & Dimotakis (1992).[†] These observations were presented at the Turbulence Symposium in honor of W. C. Reynolds's 60th birthday, 22–23 March 1993 (Monterey, CA).

A GALCIT report documenting this discussion is included as part of this report as Appendix B.

[†] Included in this report as Appendix A.

3. Mixing and combustion in supersonic, turbulent shear layers

Several “flip” (Koochesfahani & Dimotakis 1986), chemically-reacting, supersonic shear-layer flow experiments have been performed in the last year. These are part of an attempt to separate Reynolds number effects from compressibility (Mach number) effects. In our previous compressible work (Hall *et al.* 1991), Reynolds number effects were acknowledged, but could not be specifically addressed.

The recent results indicate that Reynolds number effects are the probable primary cause of lower mixing (rate), at moderate compressibility, relative to that documented on the basis of previous data in incompressible reacting shear layers, at lower Reynolds numbers, as opposed to compressibility. This is an important issue, not only theoretically but also from an applications point of view.[‡]

Previously available, chemically-reacting flow data fall in the Reynolds number range of 10^4 to 10^5 . The minimum Reynolds number for the compressible cases is around 10^6 . Important constraints, requiring that chemical reactions proceed at atmospheric pressure to ensure that they are in the fast-kinetic regime, preclude compressible runs to be performed at Reynolds numbers similar to those of the incompressible data. It is possible to extrapolate the incompressible data to these higher Reynolds numbers, but the uncertainty of these estimates is quite high.

In Hall *et al.* (1991), the primary compressibility effect observed was between the medium and high compressibility cases. Those experiments, however, could not distinguish between Reynolds number and Mach number effects and, as a consequence, it was not possible to make definitive statements regarding compressibility effects, at medium compressibility.

Figure 1 depicts the normalized product thicknesses at low stoichiometric ratios, ϕ , for the compressible flow cases of Hall *et al.* (1991) as well as the incompressible flow cases of Mungal & Dimotakis (1984), Mungal *et al.* (1985), and Frieler (1992).[#] The gap in Reynolds number, between the compressible and incompressible flow data is clear. The recent flip experiment pairs were designed to reduce the uncertainty in the Reynolds number effects at moderate compressibility ($M_c \approx 0.6$).

The flip experiment pairs were made with H_2/NO and F_2 reactants in the

[‡] D. Bushnell (private communication).

[#] See also Dimotakis (1993), included here as Appendix B, for additional discussion.

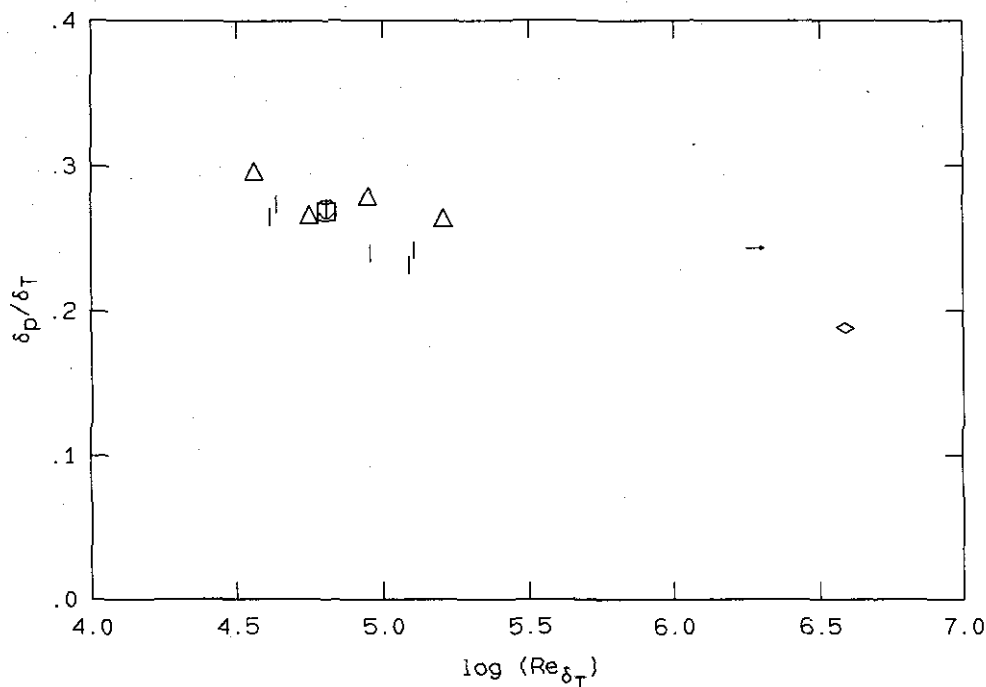


FIG. 1 Normalized product thickness for low ϕ . Squares and circles: Mungal & Dimotakis (1984); vertical bar: Mungal *et al.* (1985); triangles: Frierler (1992); arrow and diamond: Hall *et al.* (1991).

high- and low-speed streams, respectively, with mixtures of He and Ar as diluents. Separate chemical kinetic numerical simulations and experimental investigations were conducted to ascertain that the data were acquired in the kinetically-fast regime. Four conditions were arranged in two pairs. In each pair, the compressibility (Mach number), density, velocity and specific heat ratios were kept fixed. Within each pair, the two Reynolds numbers were separated by a factor of about 2.5, *i.e.*, nearly a half decade in Reynolds number. These experiments were designed such that Reynolds number would be the only cause of changes in the chemical product and mixed fluid thicknesses.

Our preliminary recent results can be compared with each other, as well as with the existing body of data, both compressible and incompressible. In this comparison, the other differences in the data must be noted. Most of the incompressible flow pair data were recorded at stoichiometric mixture ratios of $\phi = 8, 1/8$. The flows at medium compressibility were run with $\phi = 4, 1/4$. The best assessment of the difference can be made in terms of the two incompressible flow points from Mungal & Dimotakis. These are runs at identical conditions except that $\phi = 8, 1/8$

for the squares, and $\phi = 4, 1/4$ for the circles.

Another issue to consider is that different data-processing used on the different sets of data might result in differences between sets of data. To this end, the raw temperature measurements from Hall *et al.* and Frieler were reprocessed using the same procedures. Comparisons of these three sets of points will have no systematic error.

The normalized product thicknesses for low ϕ 's is shown in Fig. 2. No evidence of a Reynolds number dependence is discernible within the Reynolds number span of the new (caret and star) data. This suggests that any differences between compressible flows at these Reynolds numbers is not due to a change in Reynolds number. There is little difference between the product thicknesses extrapolated on the basis of the incompressible flow experiments and the medium compressibility cases. This implies that the reduction of product thickness for the compressible cases, relative to the previous, incompressible flow, experiments, is due to differences in Reynolds number and not to compressibility.

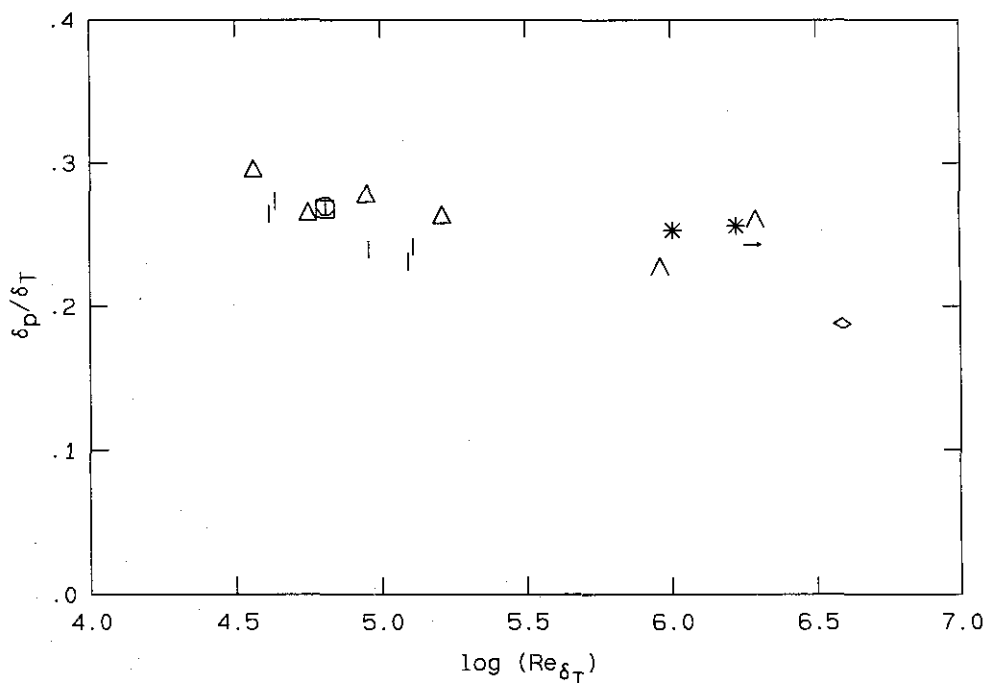


FIG. 2 Normalized product thickness for low ϕ . Square and circle: Mungal & Dimotakis (1984); vertical bars: Mungal *et al.* (1985); triangles: Frieler (1992); arrow and diamond: Hall *et al.* (1991); carets and stars: recent experiments.

The normalized product thicknesses derived from flows at high ϕ are shown in Fig. 3. No Reynolds number effect is discernible in the four new data points. Differences between the compressible experiments are probably not attributable to the difference in Reynolds numbers. The product thicknesses from the highest Reynolds number incompressible flow data are comparable to the medium compressibility cases. Again, the implication is that the effect of compressibility on molecular mixing is slight, if any, at medium compressibility.

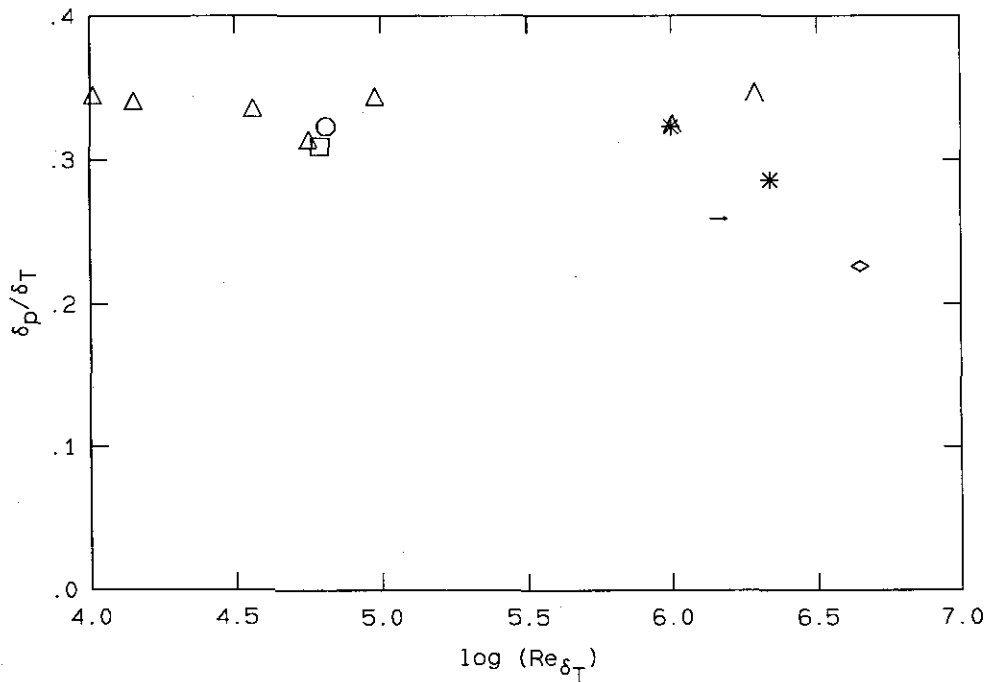


FIG. 3 Normalized product thickness for high ϕ . Square and circle: Mungal & Dimotakis (1984); triangles: Frieler (1992); arrow and diamond: Hall *et al.* (1991); carets and stars: recent experiments.

The normalized mixed fluid fraction data, derived from the high- and low- ϕ “flip” flow pairs are shown in Fig. 4. The four new points provide no clear evidence of a Reynolds number dependence for the clustered, compressible flow data. In comparisons with the incompressible data, it is important to note the two points from Mungal & Dimotakis. As was noted for the product thickness results, it seems that there is no real reduction in mixing due to compressibility.

Our recent preliminary data indicate that no strong dependence on Reynolds number exists between the new, low and high Reynolds number, compressible flow

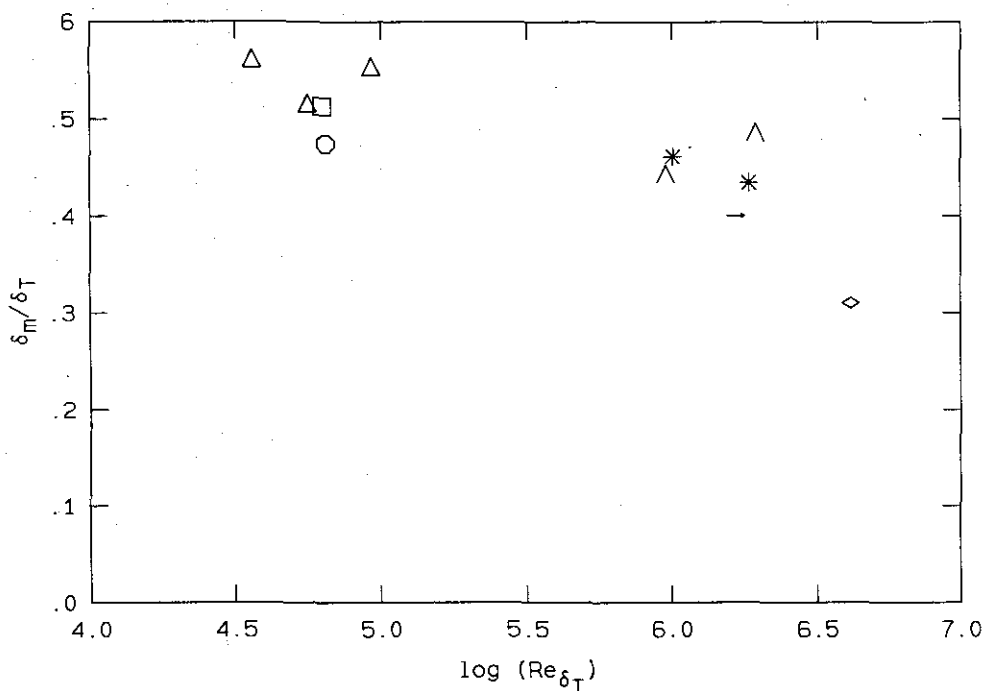


FIG. 4 Normalized mixed fluid thickness. Squares and circles: Mungal & Dimotakis (1984); triangles: Frierer (1992); arrow and diamond: Hall *et al.* (1991); carets and stars: recent experiments.

cases. This indicates that differences between compressible flows, as with the two cases of Hall *et al.*, would not be due to Reynolds number. Extrapolation of the incompressible results produces a reasonable estimate of the mixed fluid thickness values of the new data. This implies that the documented reduction in the mixed fluid fraction, at moderate compressibility, is due to the higher Reynolds numbers and not the higher Mach number in the latter flows.

We appreciate that this conclusion must be regarded as preliminary, in view of the data-less decade, or so, in Reynolds number across which the extrapolation has been made. We hope to be in a position to address this deficiency in our future work.

This work is part of the Ph.D. research effort of Chris Bond.

4. Mixing and combustion in turbulent jets

The research effort on turbulent jet mixing, involving both the gas-phase, chemically reacting and liquid-phase, non-reacting jet investigations, has been cosponsored by the Gas Research Institute, GRI Contract No. 5087-260-1467.

4.1 Gas-phase chemically-reacting jets

Previous experiments conducted in the High Pressure Reacting Vessel (HPRV) have yielded significant information on the heat release distribution in a chemically-reacting, axisymmetric jet. Those experiments documented the flame length dependence on Reynolds number, in the range $1.0 \times 10^4 \leq Re \leq 15 \times 10^4$, as well as the existence of a Reynolds-number-dependent mixing virtual origin. In addition, Damköhler number effects on mixing and the heat release distribution were investigated. See Gilbrech (1991) Dimotakis *et al.* (1992), and Dimotakis (1993),* for a more complete discussion.

In order to characterize flame length behavior, these investigations were conducted on a jet in a purely momentum-dominated regime. Below are presented the preliminary results of an investigation conducted on turbulent non-premixed reacting jets in a flow regime that cannot be regarded as in the purely momentum-dominated regime. New and unsuspected results were found in both regions.

Specifically, in the region before the flame tip, there is experimental proof that the heat release occurring in the reacting zone of the flow enhances not only the entrainment, as had been known for some time, but also the mixing. In the post-flame region, the line-integrated temperature field is characterized by a smooth dependence on the adiabatic flame temperature rise, for a range of adiabatic flame temperatures.

This part of the effort was principally undertaken by Dr. Dominique Fourquette.

* Included in this report as Appendix B.

4.1.1 Heat release effects in the flame region

A detailed description of the experimental facility and the diagnostics can be found in the Gilbrech (1991) Ph.D. thesis, as well as in Gilbrech & Dimotakis (1992). A virtually unconfined, chemically-reacting axisymmetric jet (2.5 mm nozzle diameter) of F_2 , diluted in N_2 , is discharged into a vessel containing NO , also diluted in N_2 . The adiabatic flame temperature rise, ΔT_f , and the stoichiometric mixture ratio, ϕ , are set by the relative concentration of the reactants. The nozzle-exit Reynolds number can range over more than an order of magnitude by changing the HPRV ambient pressure, thus not modifying other flow conditions. The experimental results are in the form of time-averaged, line-integrated temperature measurements both in the flame region and in the post-flame region.

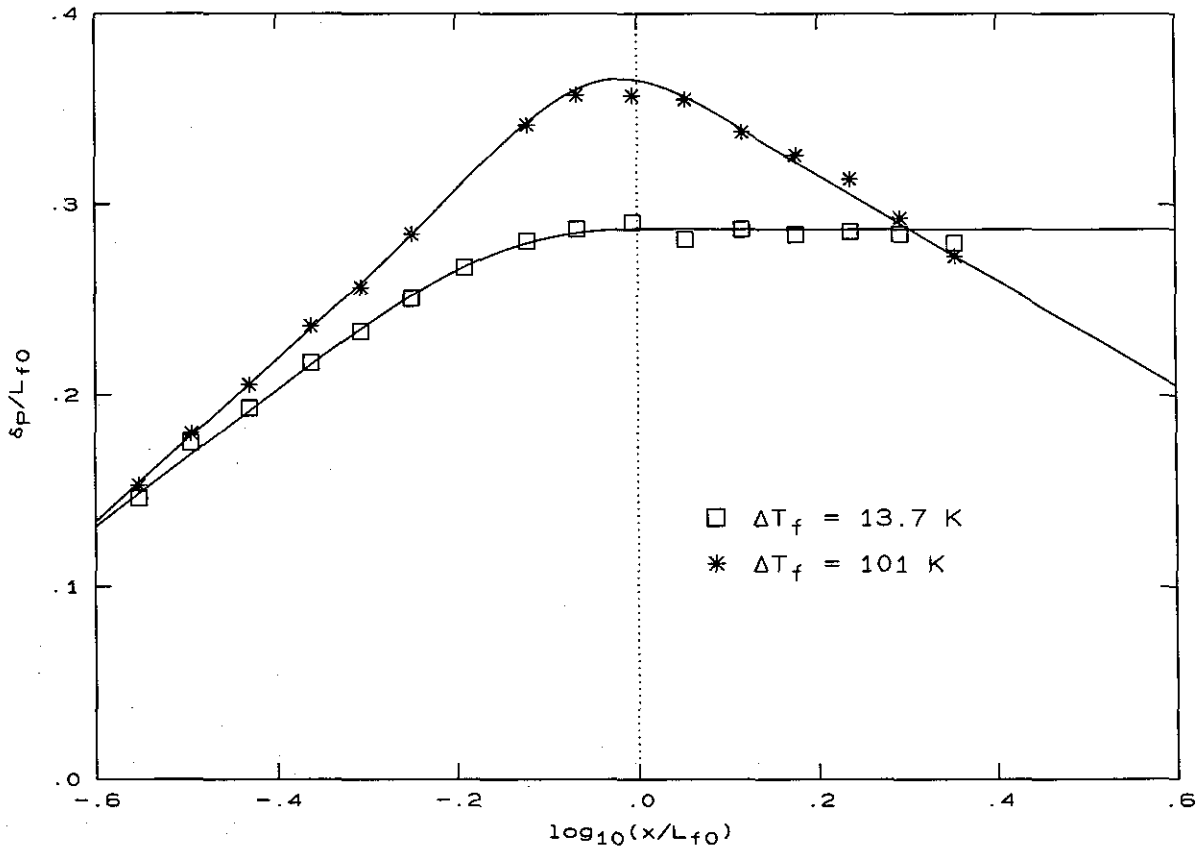


FIG. 5 Normalized product thickness for a purely and non-purely momentum-driven flame, $\phi = 14$ and $Re = 1.0 \times 10^4$.

Figure 5 shows the line-integrated temperature measurement performed in the purely momentum-dominated regime and in the case where heat release significantly affects the temperature distribution. Both axes are normalized by the flame length measured in the momentum-dominated regime. In the purely momentum-dominated case (very low heat release), $\Delta T_f = 13.7$ K, the heat release distribution is a logarithmic function of the axial distance up to the flame tip and is independent of the axial distance in the post-flame region (Gilbrech 1991). The logarithmic dependence is discussed in Dimotakis (1993), which is appended to this report (Appendix B).

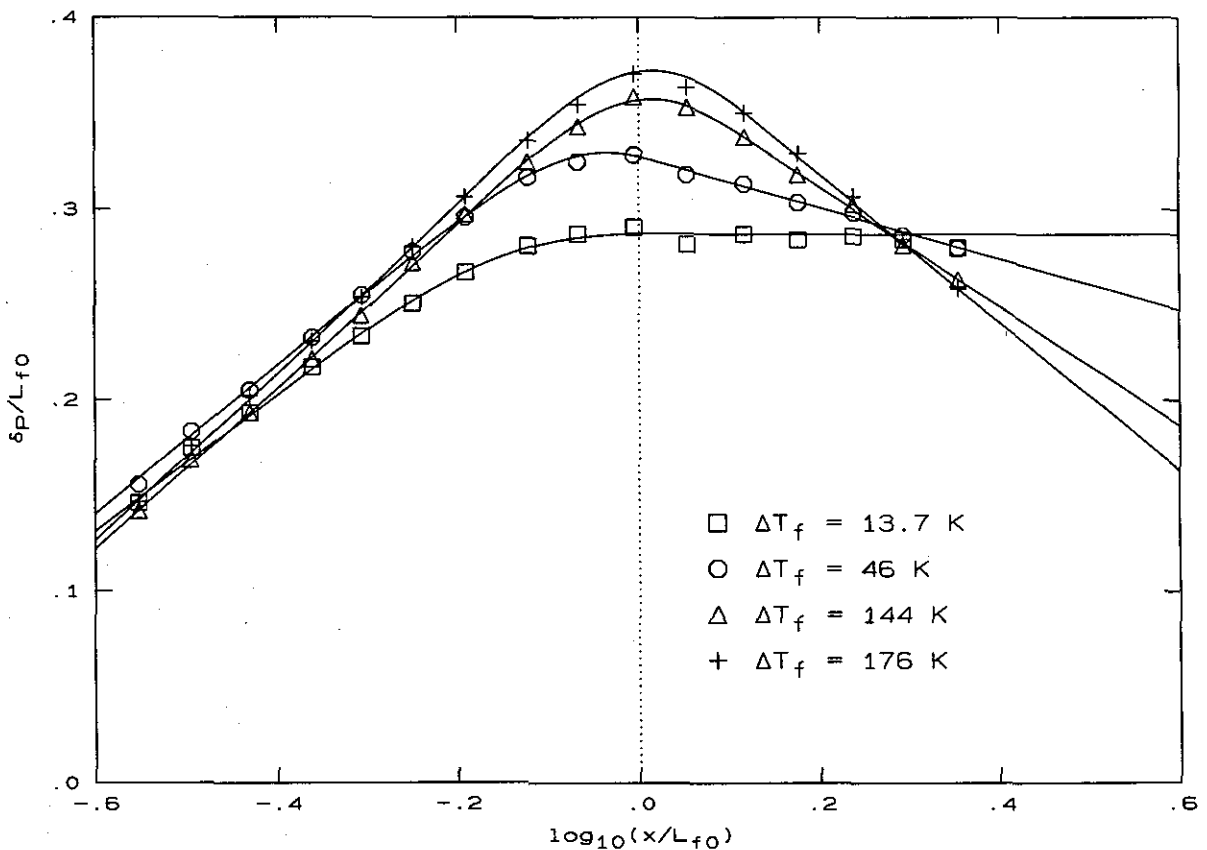


FIG. 6 Adiabatic flame temperature scan, $\phi = 14$ and $Re = 1.0 \times 10^4$.

At higher adiabatic flame temperatures (*cf.* Fig. 5 data at $\Delta T_f = 101$ K), the line-integrated measurements reveal a larger heat release in the flame region, as well as a significant excess temperature overshoot in the region of the flame tip. Higher entrainment (of cold reservoir fluid) alone would result in the same, or lower, temperatures in the flame region, and therefore cannot account for the larger heat

release. The higher line-integrals of the temperature rise observed represent a new result and indicate an enhanced mixing rate.

4.1.2 Post-flame region temperature field

The series of runs shown in Fig.6 reveal the existence of a point x_c in the post-flame region where the line-integrated temperature is independent of ΔT_f . For the case $\phi = 14$, this is located at $x_c/L_{f0} = 1.96$. In other words, at a distance downstream nearly twice the (reference) flame length, L_{f0} , *i.e.*, the flame-length measured in the (purely) momentum-dominated case. The relation, $x_c/L_{f0} \simeq 2$ holds for all ϕ 's measured, as can be seen in the following table. These data also suggest that the Reynolds number dependence of the normalized cross-over point, x_c/L_{f0} , is carried by L_{f0} .

ϕ	x_c	
	Re	x_c/L_{f0}
10	2.0×10^4	2.03
10	4.0×10^4	1.94
12	1.0×10^4	1.96
14	1.0×10^4	1.96
17.9	2.0×10^4	2.11

The consistency in the normalized cross-over point, x_c/L_{f0} , provides further credence to the method utilized to estimate flame length and that this estimate can provide a useful scaling length. Additional investigations are underway to probe further into the mixing and entrainment mechanisms.

4.2 Liquid-phase turbulent jet mixing

In our investigation of turbulent mixing and scalar interface geometry in liquid-phase jets, we have obtained two-dimensional image data, in a plane perpendicular to the jet axis, using laser-induced fluorescence techniques. High-resolution ($1,024 \times 1,024$), high signal-to-noise ratio ($\sim 250 : 1$) digital images over the full transverse extent, in the far field of the jet interior, have been recorded with a low-noise, cryogenically cooled, CCD camera. In work to date, such data have been acquired in the Reynolds number range $3.8 \times 10^3 < Re < 18 \times 10^3$. For these data, the imaging station is at $x/d = 300$. Each of the 10^6 pixels in the CCD-recording array is calibrated and normalized using ensemble averages of several background and illumination images. This allows the instantaneous, local jet-fluid concentration field, $c(y, z, t)$, to be measured at the fixed x -station imaged on the array.

Our preliminary data confirm that this range of Reynolds numbers spans a mixing transition in the far field of turbulent jets, as also documented elsewhere in this report (*cf.* Sec. 2 and Appendix B of this report). In work in progress, we are attempting to quantify this pre- and post-transition turbulent mixing state using a variety of measures.

5. Analytical and computational effort

Our work on the use of Lagrangian methods to compute unsteady, 1-D gasdynamic flows, with and without chemical reactions, was recently published (Lappas *et al.* 1993). A reprint is included as part of this report in Appendix C.

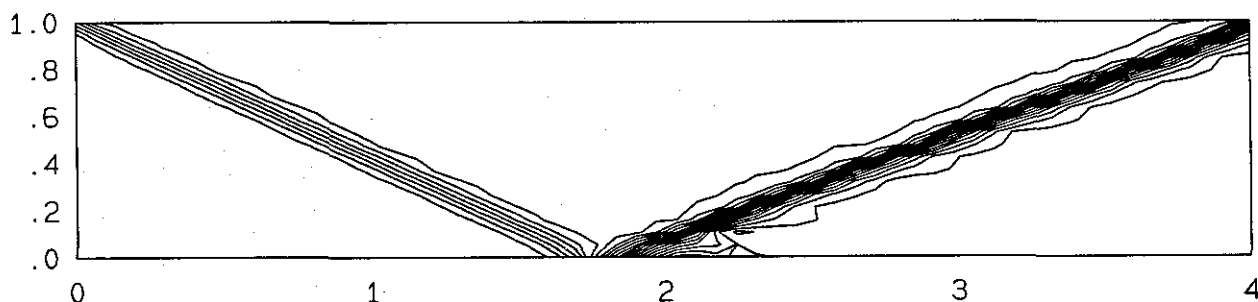


FIG. 7 Regular shock reflection. Pressure contour levels at time $t = 5$ (30 contour levels for $0.5 < p < 3.5$). Resolution: 60×20 cells.

In more recent work, a new approach for computing multidimensional flows has been developed as part of our on-going analytical and computational effort. The method of characteristics, which has been successful for hyperbolic systems in two independent variables, has been extended to the general case of several independent variables for the particular case of gas dynamics. This new approach was used to develop a numerical scheme capable of computing multidimensional flows without the arbitrary dimensional splitting that conventional methods employ. See discussion in Colella (1990), for example. A brief description of the new method was documented in a recent report (Dimotakis *et al.* 1992).

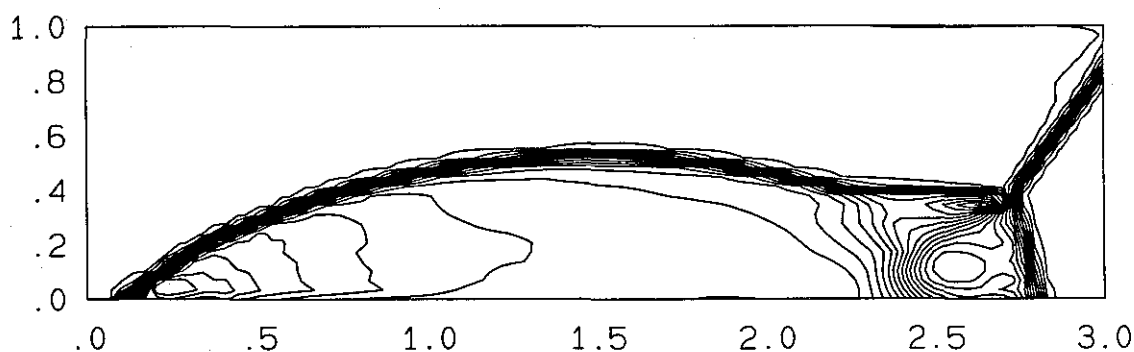


FIG. 8a Double Mach reflection. Density contour levels at $t = 0.20$ (30 contour levels for $1.7 < \rho < 18.5$). Resolution: 120×30 cells.

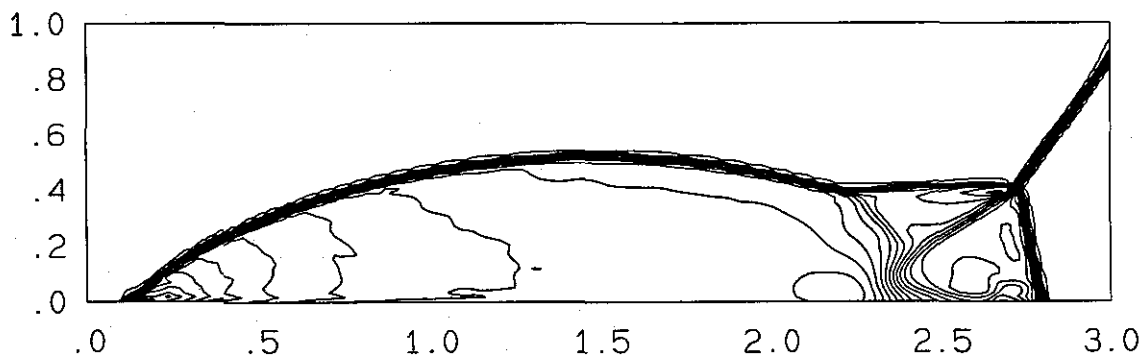


FIG. 8b Double Mach reflection. Density contour levels at $t = 0.20$ (30 contour levels in the range $1.73 < u < 21.0$). Resolution: 240×60 cells.

Part of our current effort has focused on testing this particular method and comparing it with other conventional schemes. We have developed our own version

of the Godunov scheme known as MUSCL, which is used for comparison purposes, and we have also compared our results with those of other simulations documented in the literature. In particular, test cases, such as those presented by Woodward and Colella (1984), were computed with very good results. These cases include a standard oblique shock reflection and a more interesting case of a Mach reflection. See Figs. 7, and 8a,b. These results are discussed in Lappas (1993).

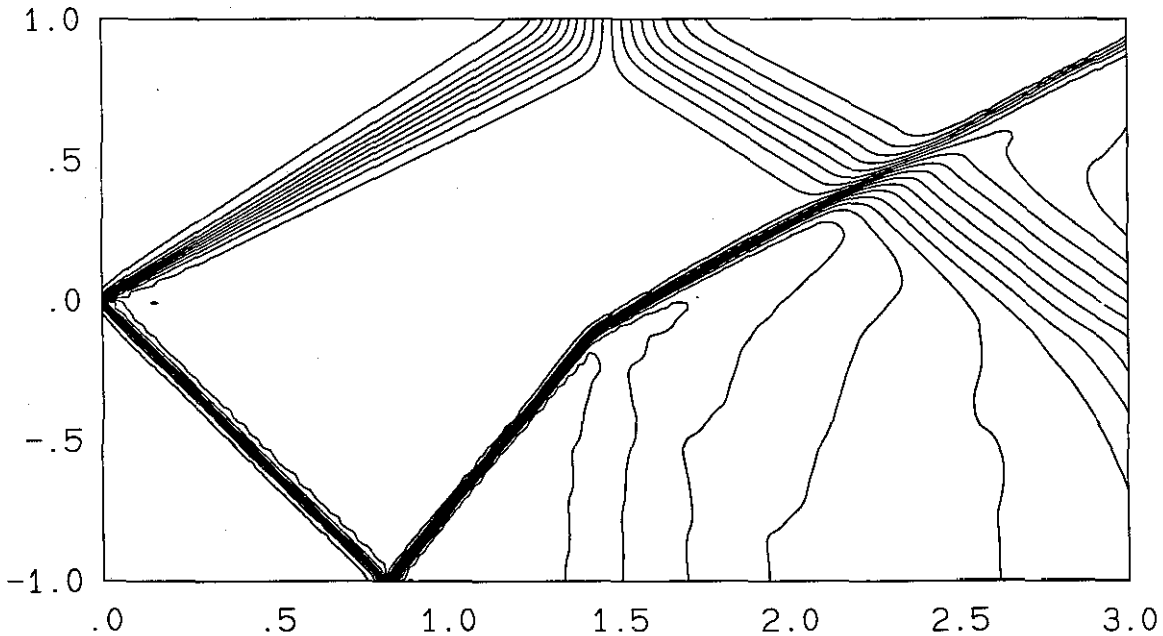


FIG. 9a Inviscid shear layer. Pressure contour levels at $t = 5.0$ (20 contour levels for $0.98 < p < 1.52$). Resolution: 200×100 cells.

In addition to validation runs, we are currently computing a variety of flows aimed at understanding the physics of the interaction of shock waves with a shear layer, or contact discontinuity. The computations are helping us understand the often complicated wave patterns that arise in such flows. This effort is helped by the adaptive gridding capability that we have developed. A hierarchy of overlapping grids can be used to compute different parts of the flow with different resolution. This is particularly important when computing regions of wave interaction where a higher resolution may be needed. See Figs. 9a,b,c.

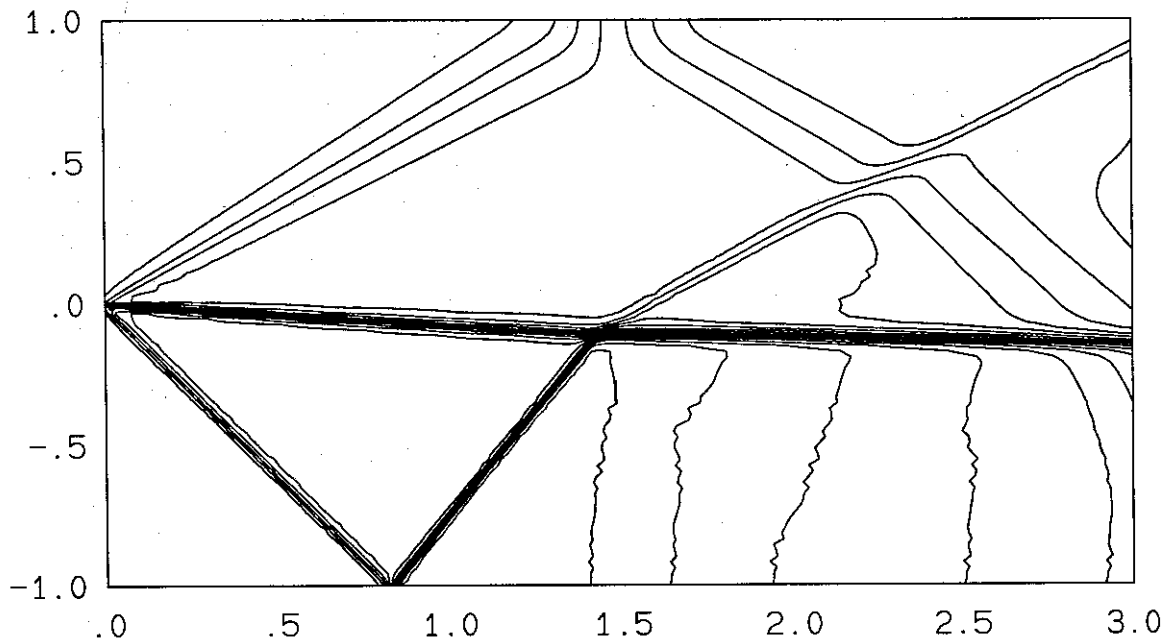


FIG. 9b Inviscid shear layer. u -velocity contour levels at $t = 5.0$ (20 contour levels for $1.38 < u < 1.85$). Resolution: 200×100 cells.

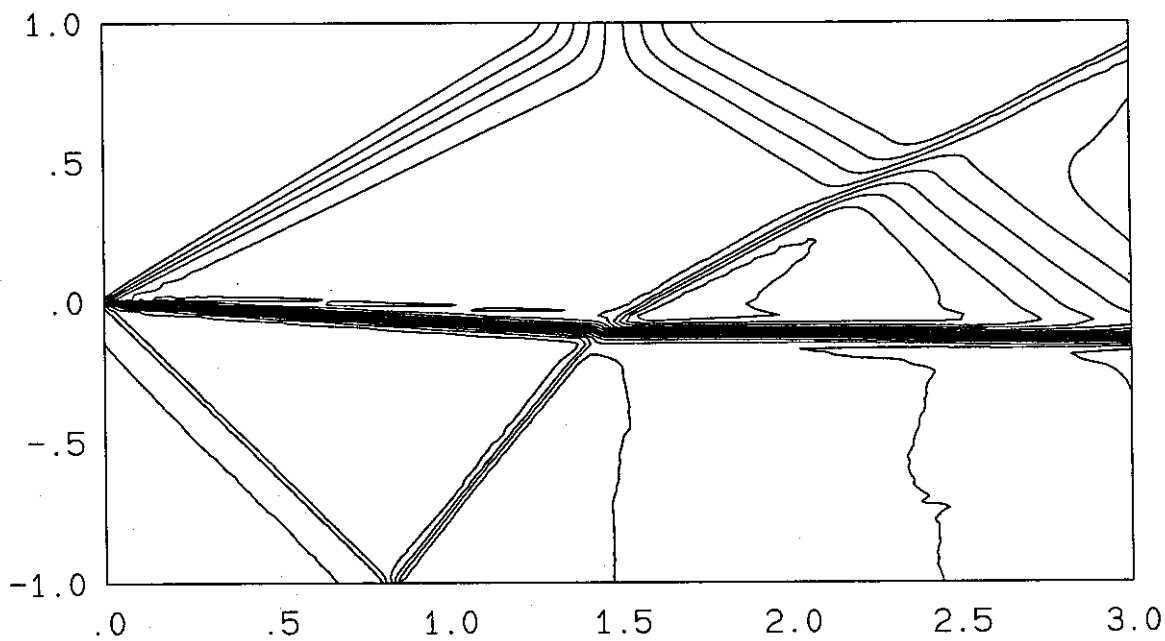


FIG. 9c Inviscid shear layer. Density contour levels at $t = 5.0$ (20 contour levels for $1.0 < \rho < 2.0$). Resolution: 200×100 cells.

6. Diagnostics, Instrumentation, & Experimental Techniques

Some of the work performed as part of this part of the effort is outlined below. The development of the image correlation velocimetry and dual-image CCD technology, in collaboration with JPL, has been cosponsored by ARPA/ONR Contract N00014-91-J-1968.

6.1 Image correlation velocimetry

Our effort in Image Correlation Velocimetry continues to refine the method, introduced in last year's report, for correlating two successive scalar images for the purpose of measuring imaged fluid velocity field information. Specifically, a method has been developed for deforming, or transforming, one image to another. Taylor-series expansions of the Lagrangian displacement field are used, in conjunction with an integral form of the equations of motion, to approximate this transformation. The method locally correlates images for displacements, rotations, deformations, and higher order displacement gradient fields. An integral form of the equations of motion is employed and, as a consequence, no spatial or temporal differentiation of the image data is required in estimating the displacement field. This improves our ability to handle data with finite signal-to-noise ratios. A significant addition to our method, over this past year, is the application of a global minimization procedure to insure a global consistency in the results. Successive, two-dimensional digital CCD images of fluid motion, marked with a passive scalar, are used to verify the capabilities of the method. The utility of the method is also illustrated using a pair of Voyager 2 images of Jupiter.

A detailed account of this effort to date can be found in Tokumaru & Dimotakis (1992), which is included as part of this report as Appendix D.

6.2 High-speed data/image acquisition developments

This part of the effort was principally undertaken by D. B. Lang, in collaboration with P. E. Dimotakis, as well as J. Janesick, T. Elliot, and S. A. Collins at JPL.

6.2.1 High-speed A/D system

We currently have two operational, high-speed A/D converter data acquisition boards for high-speed and high-resolution digital image as well as scalar data acquisition. The first board has two 12-bit 15 MHz A/D converters and can digitize two analog inputs at 15 MHz, or a single input at 30 MHz. The second board has two 12-bit 20 MHz A/D converters and can digitize two inputs at 20 MHz, or one input at 40 MHz. The two boards can be used in parallel for an aggregate data throughput, at this time, of 70×10^6 data samples/s.

Each board has 32 MB of local buffer memory and plugs into a standard VXI backplane. A VMEbus computer running the OS-9 real-time operating system controls the A/D units through a VME-to-VXI bus converter. We intend to upgrade this to an embedded VXI computer. This will eliminate the need for the VME backplane and will also permit the display of acquired images on the screen in real time for focusing and calibration purposes.

Each A/D subsystem is comprised of an analog section and a digital section. The A/D converter analog section has the following capabilities:

- a. two 12-bit 20 MHz A/D converters digitize two channels at 20 Msamples/s each, or one channel at 40 Msamples/s,
- b. programmable gain of ± 0.4 , ± 0.8 , or ± 1.6 V full scale,
- c. programmable offset of ± 0.5 , ± 1.0 , or ± 2.0 V,

and,

- d. Automatic calibration of A/D zero offset and full scale voltage.

The A/D converter digital section has the following capabilities:

- a. 32 MB of local buffer memory (70 MB/s/board throughput),
- b. word-packing logic saves memory and reduces data rate (reduces 12-bit data rate from 80 MB/s to 60 MB/s),

and,

- c. flexible triggering and scanning options, *i.e.*
 - i. trigger via front panel connectors,
 - ii. trigger via CCD controller board,

- iii. trigger via direct computer control,
- iv. 32-bit real-time counter allows event time-stamping,
- v. up to 8 scan/frame/calibration patterns,
- vi. framing words mark beginning/end of scan or frame,
- vii. optional interrupt at beginning/end of scan or frame,
- and,
- viii. programmable delay line allows conversion timing adjustments.

These first-generation boards were designed and fabricated using computer-controlled wire-wrapping technology to allow for small modifications, as dictated by their first use. The design can now be frozen and we are in the process of redesigning them, relying on multi-layer printed-circuit board technology to decrease unit costs. Following this development, four additional channels will be fabricated.

6.2.2 CCD controller board

We have recently completed the design and fabrication of a very flexible, CCD, focal plane array controller board that can control virtually any standard or custom CCD image array, including the dual-image Mach-CCD, presently under development in collaboration with James Janesick, Tom Elliot, and Andy Collins of JPL. The board has two microsequencers that can respond to external trigger events and generate the needed timing waveforms. The pixel microsequencer generates the complex waveforms needed by the Mach-CCD, or any other multiphase clock CCD, and also controls the A/D converter boards. The pixel microsequencer can be programmed to digitize a subset of the image (region of interest) in order to conserve memory and increase the framing rate. The event microsequencer is used to generate the timing waveforms for YAG lasers, the camera shutter, and other laboratory devices that must be synchronized to acquire. Both microsequencers can be triggered from an external control signal, or slaved to the other microsequencer. By way of example, the real-time microsequencer can:

- wait for an external trigger signal (*e.g.*, the start of a run),
- fire the first YAG laser,
- signal the pixel microsequencer to store the first image,

- fire the second YAG laser,

and finally

- signal the pixel microsequencer to start digitizing the two images.

The CCD controller board has the following features:

- a. internal programmable clock of up to 40 MHz (25 ns timing resolution),
- b. two external timing/pixel clock inputs/outputs,
- c. three event trigger inputs (two coax and one fiber optic),
- d. seven event trigger outputs (four coax and three fiber optic),

and,

- e. one 37-pin connector for the camera head that provides:
 - i. the CCD clock input,
 - ii. 3 CCD trigger inputs,
 and
 - iii. 14 CCD timing outputs.

The fiber optic input/outputs allow connecting to noisy devices such as the pulsed YAG lasers.

6.2.3 CCD camera head

We have designed and are currently fabricating a general-purpose use CCD camera head that can be used for the Mach-CCD. The first version uses a JPL camera head board modified to enable acquiring of two images as closely as $1 \mu\text{s}$ apart. This first version has two analog outputs providing up to 0.5 Mpixels/s each (limited by the JPL camera head board). This allows the readout of a pair of $1,024 \times 1,024$ images in two seconds.

A second generation camera head board is being designed to provide 4 analog outputs allowing a ten-fold increase to 5 Mpixels/s each, for an aggregate rate of 20 Mpixels/s. The current Mach-CCD has two analog outputs so it will be possible to acquire 10 pairs of $1,024 \times 1,024$ images per second.

The latter is a very significant development, and will permit a much better utilization of the experimental facilities used as part of this research effort. By way of example, the cost of some high Mach number, chemically-reacting runs in the supersonic shear layer facility can exceed \$2,000, each. At present, we can acquire only a single, high-quality image in such a run. The new generation of image-acquisition technology under development should permit higher signal-to-noise ratios, along with a 20-fold increase in the image framing rate.

7. Personnel

In addition to the Principal Investigators:

P. E. Dimotakis: Professor, Aeronautics & Applied Physics;

A. Leonard: Professor, Aeronautics;

other personnel who have participated in the effort during the current reporting period are listed below:

C. L. Bond: Graduate Research Assistant, Aeronautics;

H. J. Catrakis: Graduate Research Assistant, Aeronautics;

E. Dahl: Member of the Technical Staff, Div. of Engineering & Applied Science;

D. C. Fourquette: Post-doctoral Research Fellow, Aeronautics;

D. B. Lang: Staff Engineer, Div. of Engineering & Applied Science;

T. Lappas: Graduate Research Fellow, Aeronautics;

J. D. Melvin: Member of the Technical Staff, Div. of Engineering & Applied Science;

P. L. Miller: Presently, with Lawrence Livermore National Laboratories.

M. D. Slessor: Graduate Research Assistant, Aeronautics;

P. Svitek: Member of the Technical Staff, Div. of Engineering & Applied Science;

P. T. Tokumar: Post-doctoral Research Fellow, Aeronautics.

In addition,

T. Elliot: Member of the Technical Staff, JPL;

S. A. Collins: Member of the Technical Staff, JPL;

J. Janesick: Member of the Technical Staff, JPL;

have collaborated with us and are responsible for the dual-image Mach-CCD design effort at JPL.

8. References

Bibliographical references marked with a bullet (•) in the list below represent reports and publications of work performed under sponsorship of this Grant.

COLELLA, P. 1990 "Multidimensional Upwind Methods for Hyperbolic Conservation Laws," *J. Comp. Phys.* **87**, 171–200.

- DIMOTAKIS, P. E. 1993 "Some issues on turbulent mixing and turbulence," W. C. Reynolds' 60th birthday Turbulence Symposium (22–23 March 1993, Monterey, CA), GALCIT Report FM93–1. Included in this report as Appendix B.
- DIMOTAKIS, P. E., BROADWELL, J. E. & LEONARD, A. 1992 "Chemical Reactions in Turbulent Mixing Flows," California Institute of Technology, AFOSR–90–0304 Final Technical Report.
- FRIELER, C. E. 1992 *Mixing and Reaction in the Subsonic 2-D Turbulent Free Shear Layer*, Ph.D. thesis, California Institute of Technology.
- GILBRECH, R. J. 1991 *An Experimental Investigation of Chemically-Reacting, Gas-Phase Turbulent Jets*, Ph.D. thesis, California Institute of Technology.
- GILBRECH, R. J. & DIMOTAKIS, P. E. 1992 "Product Formation in Chemically-Reacting Turbulent Jets," *AIAA 30th Aerospace Sciences Meeting*, 6–9 January 1992 (Reno, Nevada), Paper 92–0581.
- HALL, J. L., DIMOTAKIS, P. E. & ROSEMAN, H. 1991 "Some measurements of molecular mixing in compressible turbulent mixing layers," *AIAA 22nd Fluid Dynamics, Plasma Dynamics and Lasers Conference*(Honolulu, 24–26 June 1991), Paper 91–1719.
- KOCHESFAHANI, M. M. & DIMOTAKIS, P. E. 1986 "Mixing and chemical reactions in a turbulent liquid mixing layer," *J. Fluid Mech.* **170**, 83–112.
- LAPPAS, T. 1993 *An Adaptive Lagrangian Method for Computing 1-D Reacting Flows and the Theory of Riemann Invariant manifolds for the Compressible Euler Equations*, Ph.D. thesis, California Institute of Technology.
- LAPPAS, T., LEONARD, A. & DIMOTAKIS, P. E. 1993 "An Adaptive Lagrangian Method for Computing 1-D Reacting and Non-Reacting Flows," *J. Comp. Phys.* **104**(2), 361–376. Included in this report as Appendix C.
- MILLER, P. L. & DIMOTAKIS, P. E. 1992 "Measurements of scalar power spectra in high Schmidt number turbulent jets," GALCIT Report FM92–3. Included in this report as Appendix A.

- MUNGAL, M. G. & DIMOTAKIS, P. E. 1984 "Mixing and combustion with low heat release in a turbulent mixing layer," *J. Fluid Mech.* **148**, 349-382.
- MUNGAL, M. G., HERMANSON, J. C. & DIMOTAKIS, P. E. 1985 "Reynolds Number Effects on Mixing and Combustion in a Reacting Shear Layer," *AIAA J.* **23**(9), 1418-1423.
- TOKUMARU, P. T. & DIMOTAKIS, P. E. 1992 "Image correlation velocimetry," GALCIT Report FM92-1. Included in this report as Appendix D.

WOODWARD, P. R. & COLELLA, P. 1984 "The Numerical Simulation of Two-Dimensional Fluid Flow with Strong Shocks," *J. Comp. Phys.* **54**, 115-173.

APPENDIX A

MILLER, P. L. & DIMOTAKIS, P. E. 1992 "Measurements of scalar power spectra in high Schmidt number turbulent jets," GALCIT Report FM92-3.

Measurements of scalar power spectra in high Schmidt number turbulent jets

Paul L. Miller and Paul E. Dimotakis

*Graduate Aeronautical Laboratories
California Institute of Technology
Pasadena, California 91125*

Abstract

Single-point, jet-fluid concentration measurements obtained from high Schmidt number ($Sc \simeq 1.9 \times 10^3$) turbulent jets permit an investigation of temporal scalar power spectra, for jet Reynolds numbers in the range of $1.25 \leq Re \times 10^{-4} \leq 7.2$. At intermediate scales, we find a spectrum with a logarithmic derivative (slope) that is increasing with Reynolds number, in absolute value, but less than $5/3$ at the highest Reynolds number in our experiments. At the smallest scales, our spectra exhibit no k^{-1} power-law behavior, possessing a log-normal region over a range of scales exceeding a factor of 40, in some cases.

9 November 1992

1. Introduction

We report here on an experimental investigation of temporal scalar power spectra of round, high Schmidt number, turbulent jets. It is part of a larger effort to better understand mixing in turbulent free shear flows, including jets and shear layers. In these experiments, we examined the jet fluid concentration (scalar) power spectra for several reasons. Spectra are sensitive diagnostics of the flow, providing information over a wide range of scales. Historically, they have been the object of a great deal of attention, partially because it is possible to extract predictions for spectral slopes from various turbulence theories and models.

Key among these turbulence theories are the 1941 paper by Kolmogorov,¹ with implications for the scalar field in the inertial range discussed by Corrsin,² Oboukhov,³ and, for higher wavenumbers, the theory by Batchelor.⁴ See, for example, discussions in Monin and Yaglom,⁵ as well as in the recent review by Gibson.⁶ Both the Corrsin and the Oboukhov theories yield predictions of power-law spectra and of the spectral power-law logarithmic derivative, or *slope*, as it will be subsequently referred to in this paper. Specifically, the Corrsin and Oboukhov theories predict a scalar spectrum proportional to $k^{-5/3}$ in the inertial range, as did the 1941 Kolmogorov theory for the energy spectrum.

For energy spectra, this has been observed experimentally under many conditions (*cf.* compilation of data by Chapman⁷). The situation is less clear concerning scalar spectra, with departures from the predicted behavior continuing to fuel debate about details and refinements of the theory.

Batchelor⁴ and Batchelor *et al.*⁸ recognized that for Schmidt, or Prandtl, numbers away from unity there exists an additional, scalar-diffusion, scale, now commonly referred to as the *Batchelor scale*, which admits a change in the scalar spectral behavior. The Batchelor theory⁴ predicted that the scalar power spectrum at high Schmidt numbers would display a k^{-1} dependence beyond the Kolmogorov wavenumber, *i.e.*, a spectral slope of -1 . Measurements in the laboratory (*e.g.*, Gibson and Schwarz⁹) and the ocean (*e.g.*, Grant *et al.*¹⁰) were subsequently reported to be in accord with this prediction.

On the other hand, more recent measurements by Gargett¹¹ in the ocean were found not to exhibit a k^{-1} spectral range (see, however, discussion by Gibson in Refs. 12 and 6). The same result was noted in passive scalar mixing measurements in shear layers¹³ and in scalar measurements in turbulent jets.^{14,15} Specifically, despite adequate resolution in those experiments, no k^{-1} range was found at high spatial wavenumbers, or, to be exact, temporal frequencies, adding to the questions about the universality, if not the validity,¹⁶ of the classical predictions at high Schmidt number.

The issue of spatial, *vs.* temporal, spectra should be recognized here. The classical theories cited deal with spatial spectra. One could argue, therefore, that comparisons of measurements of temporal spectra with predictions of spatial spectra cannot be made directly. Two points, however, should be noted in response. First, the overwhelming majority of experimentally obtained spectra reported in accord with the theoretical predictions have, in fact, been temporal. Second, at least in the case of developing flows that are not (statistically) spatially homogeneous over the range of spectral scales of interest, the notion of a spatial spectrum and the assumption of a statistically spatially homogeneous turbulent field is questionable. Temporal spectra, derived from point measurements, do not have to contend with this issue.

2. Experiment

The experiments investigated the scalar (concentration) field of round, axisymmetric, momentum-dominated, turbulent jets issuing from contoured nozzles into a large, quiescent discharge tank. The measurements were performed in the far field, on the centerline of the jet. Details of the experimental apparatus have appeared previously,¹⁴⁻¹⁷ so only a brief overview will be presented here.

The experimental facility consists of three major parts: the jet plenum, nozzle, and delivery system; a large reservoir that acts as the discharge tank; and the diagnostics, consisting of an argon-ion laser, focusing optics, collection optics, detector, signal-processing electronics, and the subsequent data-processing. The

working fluid is water, and the scalar is a laser dye (disodium fluorescein) which is homogeneously premixed with the jet plenum fluid. The resulting Schmidt number,

$$Sc \equiv \frac{\nu}{D} \quad (1)$$

with ν the kinematic viscosity of water and $D \simeq 5.2 \times 10^{-6} \text{ cm}^2/\text{s}$ the estimated aqueous species diffusivity of the fluorescein dye (Ref. 18, p. 280), is 1.9×10^3 .

The jet flow was established and maintained by pressurizing a downward oriented jet plenum with gas. Both sonically-metered and blow-down, nearly constant pressure, gas delivery configurations were used. The internal exit diameter of the jet nozzle is 2.5 mm (0.1 in.). The rectangular discharge tank is square in cross-section, approximately 2 m high and 1 m on edge. The tank bottom is over 600 nozzle diameters downstream. Large glass windows on all four sides provided optical access (see Ref. 15 for details).

The illumination source was an argon-ion laser (Coherent Innova 90). The particular unit was custom selected for its low AM noise figure ($\sim -95 \text{ dB}$) over the frequency range of interest in these experiments. It was operated at a power of 3.5 W in the light-regulation mode. The beam was spatially filtered, expanded, collimated, and subsequently focused to a small waist located on the centerline of the jet. A low dye concentration was used in the jet plenum ($\sim 10^{-6} \text{ M}$), with correspondingly substantially lower concentrations at the measuring stations. A more detailed discussion of this and related issues may be found in Refs. 14 and 15. The emitted fluorescence intensity was then proportional to the local scalar (dye) concentration $c(\mathbf{x}, t)$, that was, in turn, averaged over the extent of the measurement volume.

The fluorescence emitted from the measurement volume was collected through a narrow slit spatial filter. The beam profile and the slit width defined a small, spatially-averaging volume, roughly spherical in shape and of extent (diameter) $\ell_a \approx 50 \mu\text{m}$, as estimated by direct observation using a cathetometer. We will return to this quantity later.

A photomultiplier tube (RCA 8645) was used to detect the fluorescence emitted from this volume. Its output signal was amplified by a custom-designed low-noise transimpedance amplifier, low-pass filtered using a third-order Butterworth filter, digitized, sampled with some margin with respect to the Nyquist frequency, and stored for subsequent processing.

The measurements to be discussed here were made in the far field, on the axis of the jet, for jet Reynolds numbers in the range of

$$1.25 \times 10^4 \leq Re \equiv \frac{u_0 d}{\nu} \leq 7.2 \times 10^4 , \quad (2)$$

where u_0 is the nozzle exit velocity, d the nozzle exit diameter, and ν is the kinematic viscosity. Data were also recorded at both lower and higher Reynolds numbers. The lower Reynolds number jets, however, behaved substantially differently, by any of a number of criteria, and were not accepted as representing *bona fide* turbulence.¹⁴ In the other limit, the jet at the higher Reynolds number ($Re = 10.2 \times 10^4$) produced a distinct hissing sound. This was probably generated by the transient dilatation and subsequent oscillations of small air bubbles caused by the rapid reduction in pressure in such bubbles as they exited the nozzle, or by cavitation in the jet near-field region, or both (note that the plenum gauge pressure is quadratic with Reynolds number). See discussion and references in Ref. 19, pp. 452–453, and Ref. 20, pp. 205–207, for example. As a result, the $Re = 10.2 \times 10^4$ jet was exposed to different near-field conditions and will not be included in the discussion below. See Ref. 15 for a further documentation of the data.

Finally, constraints dictated by resolution and statistical convergence, *vis-à-vis* total number of large scale structures captured and length-of-run considerations, led to measurement stations in the range,

$$100 \leq \frac{x}{d} \leq 305 , \quad (3)$$

where x is the distance from the nozzle exit.

3. Scalar power spectrum estimation

The fluorescence signal $\phi(t)$, representing the photon flux incident on the photodetector, is a linear function of the spatial average of the convected local jet-fluid concentration $c(\mathbf{x}, t)$ over the measurement volume. It produces a signal that can be approximated by a convolution over $c(t) = c(\mathbf{x}_0, t)$, the jet fluid concentration at, say, the center of the measurement volume, \mathbf{x}_0 , *i.e.*,

$$\phi(t) \simeq \int_{-\infty}^{\infty} h_a(t-t') c(t') dt' \equiv h_a(t) \otimes c(t) . \quad (4)$$

In this expression, $h_a(t)$ models the impulse response of the spatio-temporal averaging process, *i.e.*, the temporal signal that would be measured if a spatial delta function of dye was convected through the measurement volume at the local flow velocity. See Fig. 1.

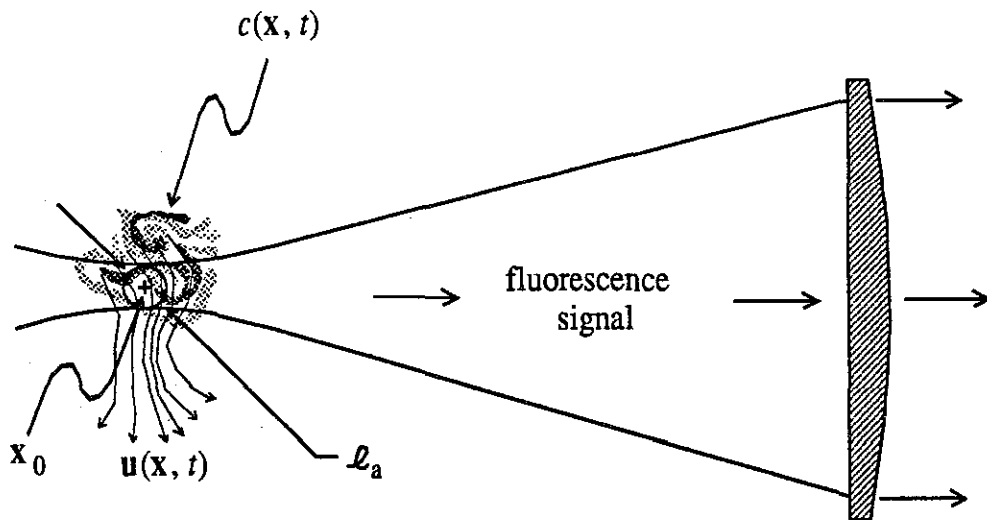


FIG. 1 Sketch of jet fluid concentration field $c(\mathbf{x}, t)$, convected through the measurement volume of extent l_a .

The fluorescence output $\phi(t)$, along with fluctuations contributed by the small laser intensity fluctuations, convected residual non-uniformities in the jet plenum dye concentration, photon shot noise, electronic noise generated by the signal-processing chain, *etc.*, was processed by the Butterworth low-pass filter to produce the total signal

$$s(t) = h_{LP}(t) \otimes \phi(t) + n(t) = h(t) \otimes c(t) + n(t) , \quad (5)$$

that was digitized and stored. In this expression, $h(t) \equiv h_{\text{LP}}(t) \otimes h_a(t)$ is the total system transfer function and $n(t)$ is the total, low-pass-filtered noise.

Assuming that the total system noise $n(t)$ can be modeled as uncorrelated with the local dye concentration time history $c(t)$, the spectrum $S_s(\omega)$ of $s(t)$ can be expressed in terms of the spectrum $S_\phi(\omega)$ of $\phi(t)$ and the spectrum $S_n(\omega)$ of the (low-pass filtered) noise $n(t)$, *i.e.*,

$$S_s(\omega) \simeq S_\phi(\omega) + S_n(\omega) , \quad (6)$$

where, from Eq. 4,

$$S_\phi(\omega) \simeq |H_a(\omega)|^2 S_c(\omega) , \quad (7)$$

with $H_a(\omega) \equiv \mathcal{FT}\{h_a(t)\}$, the Fourier transform of $h_a(t)$. This allows us to relate the total signal spectrum, $S_s(\omega)$, to the desired scalar fluctuation spectrum, $S_c(\omega)$, of $c(t)$, *i.e.*

$$S_s(\omega) \simeq |H(\omega)|^2 S_c(\omega) + S_n(\omega) \simeq |H_a(\omega)|^2 S_c(\omega) + S_n(\omega) , \quad (8)$$

where $H(\omega) \equiv \mathcal{FT}\{h(t)\} = H_{\text{LP}}(\omega) H_a(\omega)$.

For these experiments, the knee of the Butterworth low-pass filter was set substantially higher than the range of frequencies contained in $S_\phi(\omega)$. Its main purpose was to bandlimit the noise and de-alias the digitized measurements, allowing the noise-floor to be determined, as will be illustrated in the spectra presented below. This is the reason the modulus squared of $H_{\text{LP}}(\omega)$, the transfer function of the low-pass filter, can be ignored in Eqs. 7 and 8, and wherever it multiplies $S_\phi(\omega)$ and $S_c(\omega)$.

Figure 2 illustrates these relations by comparing the spectrum $S_s(\omega)$ of the total signal $s(t)$, *i.e.*, fluorescence $\phi(t)$ plus noise $n(t)$, with $S_\phi(\omega)$, the spectrum of the fluorescence signal alone. The latter was calculated by subtracting the estimated noise spectrum, $S_n(\omega)$, from the total spectrum $S_s(\omega)$. Recalling Eq. 6, we have

$$S_\phi(\omega) \simeq S_s(\omega) - S_n(\omega) . \quad (9)$$

The noise spectrum was assumed to be white, as was found to be the case in separate measurements of this quantity (see also Ref. 21 for examples). Nevertheless, the result is not sensitive to the assumed shape of the noise spectrum at low frequencies where $S_\phi(\omega)$ dominates. The data processed to produce the spectra in Fig. 2 were recorded at $x/d = 100$, for $Re = 1.25 \times 10^4$. Note the high dynamic range of the total signal spectrum, *i.e.*, the (logarithmic) difference of the low-frequency power to noise-floor power. Note also that the span to one-half the (scaled) sampling frequency is well beyond the noise-cross-over frequency. As can be seen, the frequency extent of the noise floor was substantial.

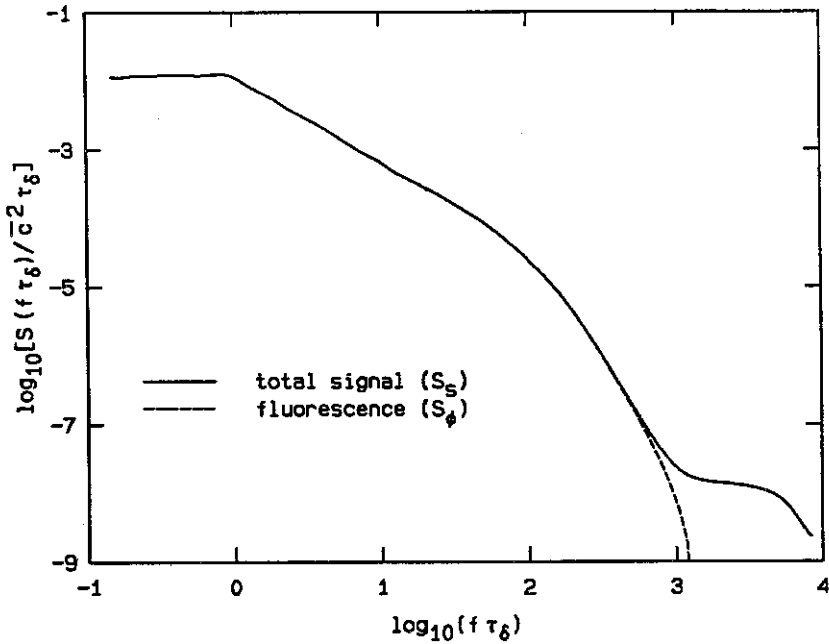


FIG. 2 Sample spectrum of the total signal (solid line: fluorescence + noise) and estimated fluorescence spectrum (dashed line: fluorescence), derived from measurements at $x/d = 100$, $Re = 1.25 \times 10^4$. Frequency scaled by $\tau_\delta(x)$, the local large-scale-passage time.

The spectra in Fig. 2, and throughout this paper, are normalized by \bar{c}^2 , the square of the local mean value of $c(t)$, multiplied by the local large-scale-passage time, $\tau_\delta(x)$, and plotted in terms of the circular frequency, f , scaled by $\tau_\delta(x)$. In these coordinates, their integral produces the normalized variance, *e.g.*,

$$\frac{c'^2}{\bar{c}^2} = \int_0^\infty \left[\frac{S_c(f\tau_\delta)}{\bar{c}^2 \tau_\delta} \right] df \tau_\delta . \quad (10)$$

The local large-scale-passage time, τ_δ , is given by,

$$\tau_\delta(x) \equiv \frac{\delta(x)}{u_{cl}(x)}, \quad (11a)$$

where

$$\delta(x) \simeq 0.41 x, \quad (11b)$$

is the local outer scale of the flow, here identified with the (measured) mean transverse extent (visual width) of the conical region enveloping the jet-fluid (Ref. 15, Appendix D), and $u_{cl}(x)$ is the mean centerline velocity. The latter was estimated from the relation

$$\frac{u_{cl}(x)}{u_j} = 6.2 \frac{d}{x - x_j}, \quad (11c)$$

where u_j is the jet velocity and x_j the jet (virtual) origin, recommended by Chen and Rodi.²² This spectrum and frequency scaling was found to produce similarity with respect to the downstream coordinate, x/d , in the analysis of scalar spectra measured in gas-phase jets.²³

The spectrum $S_c(\omega)$ of the scalar fluctuations $c(t)$ can, at least formally, be estimated by solving Eq. 7, *i.e.*,

$$S_c(\omega) \simeq \frac{S_\phi(\omega)}{|H_a(\omega)|^2}, \quad (12a)$$

or Eq. 8, yielding a result in terms of experimentally estimated quantities, *i.e.*,

$$S_c(\omega) \simeq \frac{S_s(\omega) - S_n(\omega)}{|H_a(\omega)|^2}. \quad (12b)$$

We should note, at this point, that Eq. 4, assuming a fixed $h_a(t)$, is not a proper equation for two reasons. First, the fluid velocity convecting the $c(\mathbf{x}, t)$ -field through the measurement volume is not a constant. Second, different scalar field lagrangian trajectories through the measurement volume sample chords of different sizes (and transit times) through it. These two effects could, in principle, be expressed as two additional convolutions over the local velocity field and scalar paths through the measurement volume. See Fig. 1.

For frequencies, however, corresponding to spatial scales of the order of, or less than, the extent of the measurement volume, ℓ_a , where the $H_a(\omega)$ transfer function will have an effect on the measurement of the scalar spectrum, fractional fluctuations in the convecting velocity are considerably smaller than fractional fluctuations in $c(\mathbf{x}, t)$, at least for this high-Schmidt-number fluid. They are also, largely, uncorrelated with them. Fluid paths through the measurement volume are also uncorrelated with the passively-convected scalar field. As a consequence, in estimating the spectrum in the frequency neighborhood of

$$f\tau_\delta(x) \approx \frac{\delta(x)}{2\pi\ell_a}, \quad (13)$$

and above, these two effects do not contribute.

Alternatively, the most general expression of the linear dependence of the fluorescence signal, $\phi(t)$, on the local jet-fluid concentration, $c(t)$, is given by Eq. 7. While Eq. 7 follows from Eq. 4, the converse is not true. Equation 4 is more restrictive, also requiring a definite phase relation between $c(t)$ and $\phi(t)$. Fortunately, these (unknown) phase relations do not enter in the relation between the corresponding spectra. We may conclude that Eqs. 7 and 12 represent valid relations for the corresponding spectra, even as Eq. 4 cannot be accepted as a correct description of the time-history of the fluorescence signal $\phi(t)$.

The estimation of the scalar spectrum $S_c(\omega)$ in the frequency range influenced by the spatio-temporal averaging of the measurement process also requires knowledge of the $H_a(\omega)$ transfer function. This can be estimated, in turn, by noting that it is dominated by a pole corresponding to the transit time of the flow through the measurement volume, *i. e.*,

$$H_a(\omega) \sim \frac{1}{1 + i\omega\tau_a}, \quad (14a)$$

with

$$\tau_a \approx \frac{\ell_a}{u_{cl}(x)}. \quad (14b)$$

Performing two different experiments, under as identical flow conditions as was feasible, at two different spatial resolutions, we were able to compare the spectra, for $p = 1, 2$,

$$S_{s_p}(\omega) \simeq |H_p(\omega)|^2 S_c(\omega) + S_{n_p}(\omega), \quad (15a)$$

corresponding to two different locations of the dominant pole, at, say, $\tau_a = \tau_1$ and $\tau_a = \tau_2 > \tau_1$, *i.e.*, for $p = 1, 2$,

$$H_p(\omega) \simeq \frac{1}{1 + i\omega\tau_p}. \quad (15b)$$

If the scalar spectrum, $S_c(\omega)$, could be assumed to be identical in the two experiments (the corresponding noise floors were determined separately in each case), we see that the ratio of the two fluorescence spectra,

$$\frac{S_{\phi_1}}{S_{\phi_2}} \simeq \frac{S_{s_1}(\omega) - S_{n_1}(\omega)}{S_{s_2}(\omega) - S_{n_2}(\omega)} \equiv G(\omega; \tau_1, \tau_2), \quad (16a)$$

would be given by

$$G(\omega; \tau_1, \tau_2) \simeq \frac{1 + (\omega\tau_2)^2}{1 + (\omega\tau_1)^2} = \begin{cases} 1, & \text{for } \omega \ll 1/\tau_2; \\ (\tau_2/\tau_1)^2, & \text{for } \omega \gg 1/\tau_1, \end{cases} \quad (16b)$$

independently of the, as yet unknown, scalar spectrum, $S_c(\omega)$.

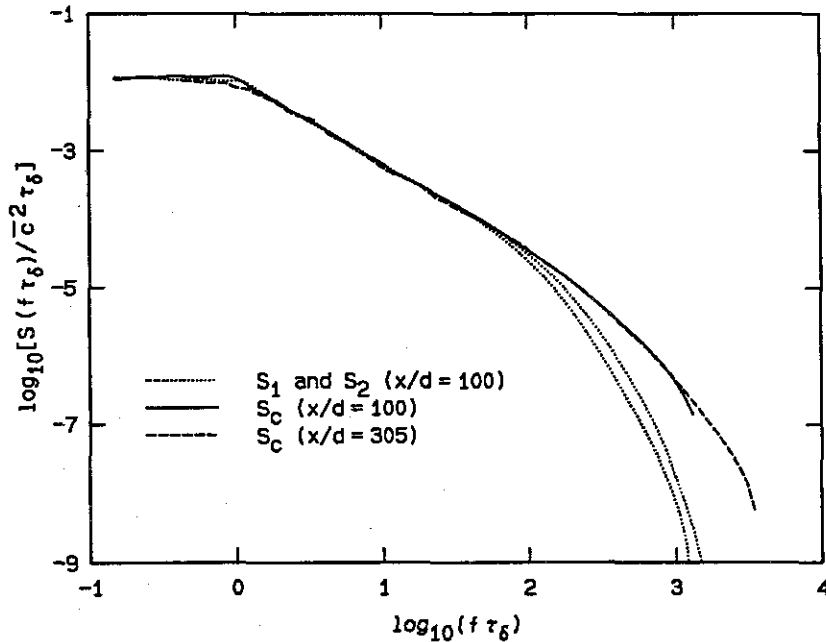


FIG. 3 Dotted lines: Fluorescence spectra estimated from measurements at $x/d = 100$ and $Re = 1.25 \times 10^4$ at two spatial resolutions. Solid line: Estimated concentration spectrum (Eq. 12) at $x/d = 100$ and $Re = 1.25 \times 10^4$. Dashed line: Estimated concentration spectrum at $x/d = 305$ and $Re = 1.2 \times 10^4$.

Two fluorescence spectra, $S_{\phi_1} = S_{s_1}(\omega) - S_{n_1}(\omega)$ and $S_{\phi_2} = S_{s_2}(\omega) - S_{n_2}(\omega)$, from one such pair of experiments, at $x/d = 100$ and $Re = 1.25 \times 10^4$, are plotted in Fig. 3 (dotted lines). The fluorescence spectrum with the larger high-frequency content is the one plotted in Fig. 2. Power spectra were computed numerically using a power spectral density estimation methodology that has evolved over the past ten years, or so. A documentation of some of its earlier features can be found in Ref. 24. In processing the data in the experiments reported here, the power spectral density estimation program computes spectra of data files by means of FFT methods, and incorporates Hanning windowing, contiguous record overlapping, and parabolic detrending, among other features. Records up to 2^{17} points can be accommodated. For spectra known to be smooth, the program can provide third-octave ($\approx 1/10$ decade) gaussian filtering, sampled at 20 points per decade, to produce the final spectra. This feature was used for all the spectra plotted in this paper, not so much for smoothing, but to reduce the number of points to a manageable level for plotting purposes (note that $2^{16} = 65,536$).

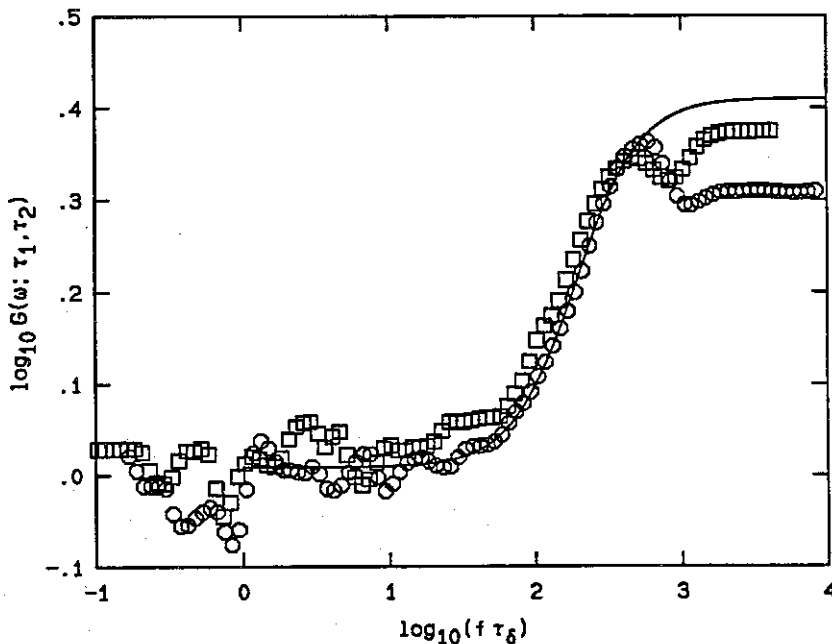


FIG. 4 Computed ratio, $G(\omega; \tau_1, \tau_2)$, of fluorescence spectra at $x/d = 100$ (Eq. 16). Circles: $Re = 1.25 \times 10^4$. Squares: $Re = 2.55 \times 10^4$. Solid line: Least squares fit for τ_1 and τ_2 .

The ratios $G(\omega; \tau_1, \tau_2)$ for a pair of spectra, measured at $x/d = 100$, at $Re = 1.25 \times 10^4$ (circles) and a pair at $Re = 2.55 \times 10^4$ (squares), respectively, are plotted in Fig. 4. As can be seen, the ratios of spectra measured at different Reynolds numbers are very nearly the same, in accord with the analysis outlined above, even though, as we will see below, the spectra themselves are Re -dependent.

The curve (solid line) in Fig. 4 is a least-squares fit for τ_1 and τ_2 to the lower Reynolds number data, that were characterized by the higher signal-to-noise ratio, in the frequency range $1.0 \leq f\tau_\delta \leq 2.8$. The lower limit of the fit range is chosen so as to exclude (the small) run-to-run variations at frequencies well below those affected by the spatial averaging. The upper frequency limit is dictated by the less than unity signal-to-noise ratio at higher frequencies yet (*cf.* Fig. 2). The values for τ_1 and τ_2 estimated by this procedure were

$$2\pi \tau_1/\tau_\delta \simeq 4.2 \times 10^{-3} \quad \text{and} \quad 2\pi \tau_2/\tau_\delta \simeq 6.6 \times 10^{-3} \quad , \quad (17)$$

respectively. This corresponds to an effective spatial extent of the measurement volume of $\ell_a \simeq 69 \mu\text{m}$ for the smaller of the two (Eq. 13), in reasonable accord with the visually estimated value of $\sim 50 \mu\text{m}$ using the cathetometer. This value was used to calculate the concentration spectrum, $S_c(\omega)$, at $x/d = 100$ and $Re = 1.25 \times 10^4$, plotted as the solid line in Fig. 3. It was computed from the fluorescence spectrum recorded at the higher resolution, using Eq. 12 with the estimated single-pole transfer function $H_a(\omega)$ of Eq. 14, at $\tau_a = \tau_1$.

The effective pole locations for data recorded at $x/d = 305$ were more difficult to estimate. At $x/d = 305$, the higher relative spatial resolution pushed the poles closer to the noise cross-over point. On the other hand, at $x/d = 305$, the (logarithmic) difference between the fluorescence and estimated concentration spectra was much smaller over the frequency range of interest. Figure 5 plots the fluorescence spectrum (dotted line) at $x/d = 305$ and $Re = 1.2 \times 10^4$ as well as the estimated concentration spectrum (dashed line). As can be seen, the effects of compensation, in this case, are much smaller (*cf.* difference at, say, $f\tau_\delta \simeq 2.7$ in Figs. 3 and 5). The estimated concentration spectrum at $x/d = 305$ in Fig. 5 is the one plotted as a dashed line in Fig. 3.

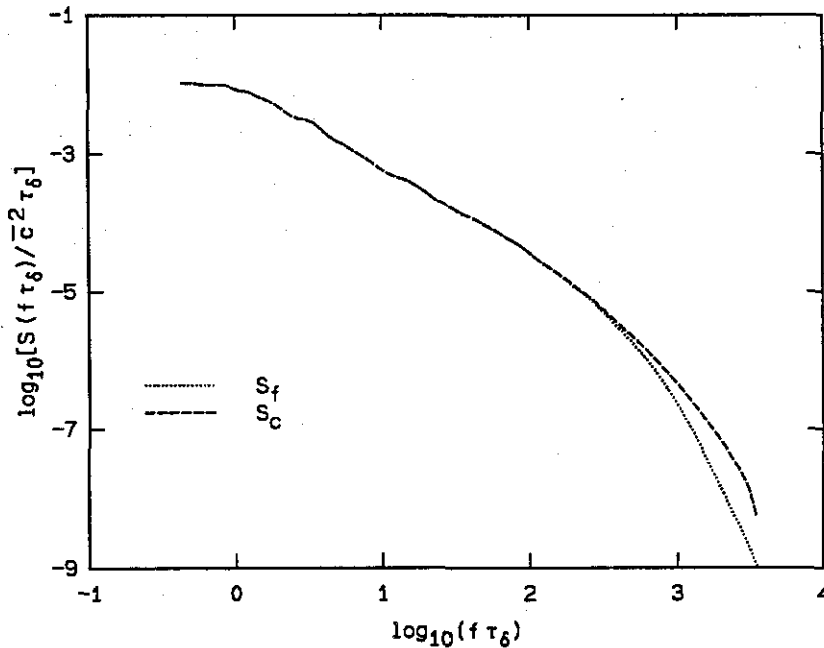


FIG. 5 Dotted line: Fluorescence spectrum. Dashed line: Estimated concentration spectrum. Data recorded at $x/d = 305$ and $Re = 1.2 \times 10^4$.

The jet fluid concentration spectra to be discussed below were all estimated in this fashion. The values of τ_a , the transfer function time constant used in the compensation calculations, were fixed for all the data measured at each x/d axial location (Eq. 17, for measurements at $x/d = 100$, depending on which slit width was used to record the fluorescence data). A fixed pair of values was also used for all the data measured at $x/d = 305$.

4. Results and discussion

The conspicuous agreement between the concentration spectra at $x/d = 100$ (solid line) and $x/d = 305$ (dashed line) in Fig. 3, up to frequencies limited by signal-to-noise ratio considerations, should be noted. A similar independence of the scaled spectra with downstream location was also found to hold in gas-phase jets,²³ where the relatively larger diffusion scales, at $Sc \approx 1$, and comparable Reynolds numbers made it possible to estimate the concentration spectra with enough spatial resolution directly, obviating the need for the compensation scheme employed here.

In the case of the present, liquid-phase data, we should entertain the possibility that the collapse of the spectra may be attributable to a fortuitous choice of the compensation pole. Some observations, however, are relevant here. First, the close agreement between the two spectra also holds in the $f\tau_\delta < 2$ frequency range, where the effects of compensation, even for the $x/d = 100$ data, are negligible. As we will see below, this will also be found to be the case at higher Reynolds numbers. Second, the value of the pole represents a single parameter. In contrast, the collapse of the spectra at the two axial locations, with substantially different degrees of compensation in each case, is over 5 orders of magnitude in the power spectra. Conversely, this collapse supports the validity of the single-pole model for the leading order behavior of the measurement transfer function.

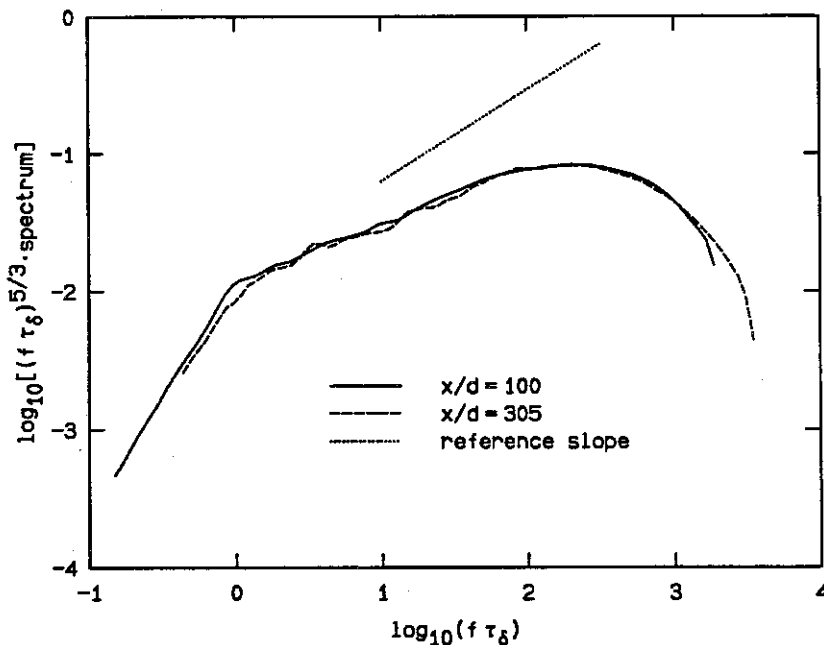


FIG. 6 Frequency-scaled concentration spectra. Solid line: $x/d = 100$ and $Re = 1.25 \times 10^4$. Dashed line: $x/d = 305$ and $Re = 1.2 \times 10^4$. Dotted line: reference line at a $2/3$ slope, corresponding to a k^{-1} spectrum.

It is useful to plot the product of the concentration spectra with $f^{5/3}$, as is commonly done. A spectrum described by a $-5/3$ power-law yields a horizontal line over the $-5/3$ frequency range when plotted in this fashion. The product of the concentration spectra with $(f\tau_\delta)^{5/3}$, derived from the data at $x/d = 100$ and

$x/d = 305$, at $Re = 1.25 \times 10^4$ and $Re = 1.2 \times 10^4$, are plotted in Fig. 6 as the solid and dashed line curves, respectively. Also plotted, for reference, is a straight line with a slope (logarithmic derivative) of $2/3$, corresponding to the high-Schmidt number Batchelor k^{-1} theoretical spectrum.⁴

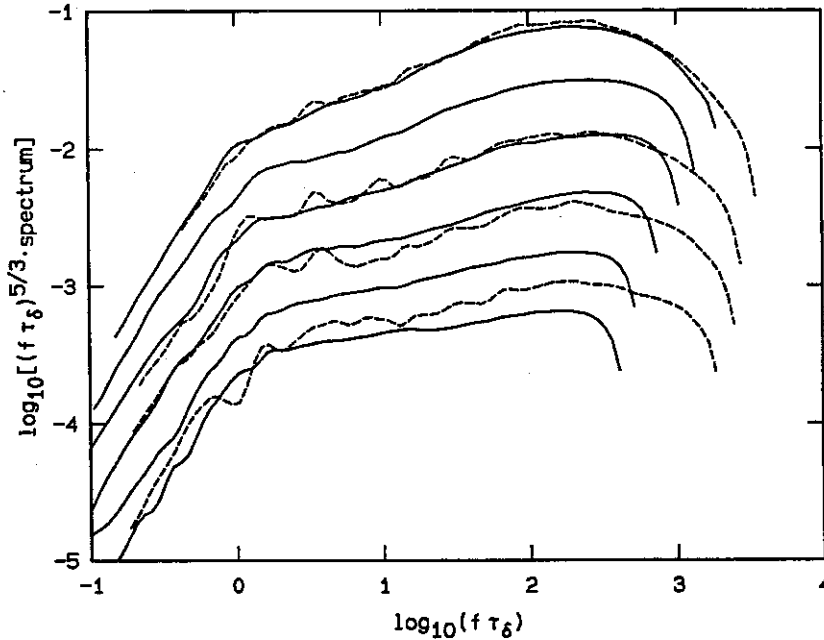


FIG. 7 Frequency-scaled concentration spectra. Solid lines: $x/d = 100$ data ($1.25 \leq Re \times 10^{-4} \leq 7.2$). Dashed lines: $x/d = 305$ data ($1.2 \leq Re \times 10^{-4} \leq 6.5$). Individual spectra are offset by $-2 \log_{10}(Re/Re_0)$, $Re_0 = 1.2 \times 10^4$, for clarity.

The solid lines in Fig. 7 plot spectra derived from measurements at $x/d = 100$, for $Re \times 10^{-4} = 1.25, 1.76, 2.55, 3.6, 5.1$, and 7.2 . The decrease in the scaled frequency resolved, in the $x/d = 100$ spectra, as the speed of the flow increased with increasing Reynolds number, is evident. The dashed lines plot spectra measured at $x/d = 305$, for $Re \times 10^{-4} = 1.2, 2.4, 4.0$, and 6.5 . As can be seen, the highest frequency resolved in the $x/d = 305$ spectra is a much weaker function of Reynolds number, signal-to-noise ratio limitations being more serious than spatial resolution at this station. Individual spectra for both x/d stations are plotted offset by $-2 \log_{10}(Re/Re_0)$, with $Re_0 = 1.2 \times 10^4$, to aid in visualizing the evolution of trends with Reynolds number.

The longer characteristic local time scale at $x/d = 305$ did not allow as many large scale structures to be included in the record. As a consequence, the statistical convergence of the $x/d = 305$ spectra is not as good as for the $x/d = 100$ data. On the other hand, the higher relative spatial resolution at $x/d = 305$ allowed the spectrum to be estimated to a higher (scaled) frequency. That trade-off aside, the agreement between the (scaled) spectra at $x/d = 100$ and $x/d = 305$ holds for all the cases for which data were recorded at the same, or nearly the same, Reynolds number at the two stations.

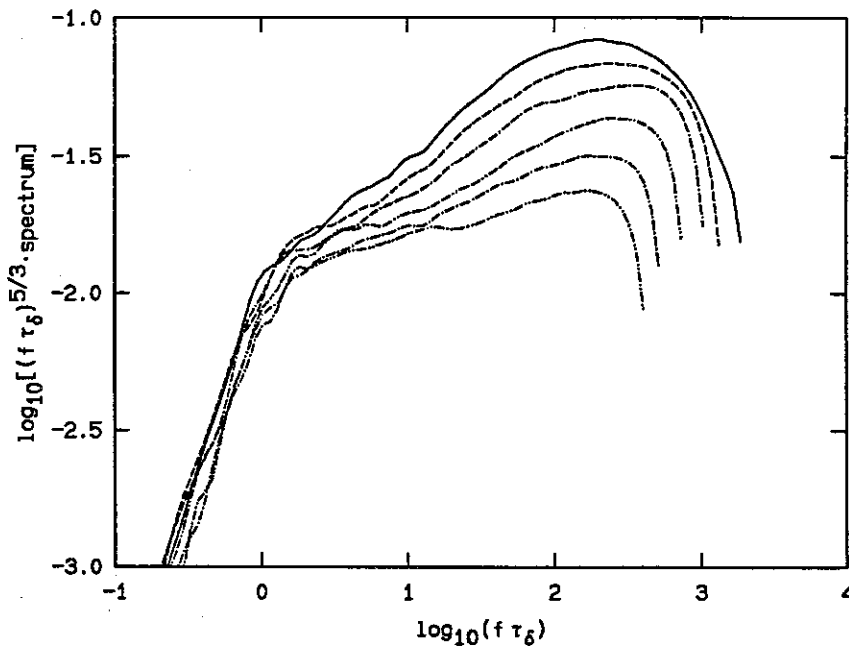


FIG. 8 Frequency-scaled concentration spectra derived from data at $x/d = 100$ and $1.25 \leq Re \times 10^{-4} \leq 7.2$ (no offsets).

Following the transition out of the large scale frequency regime ($f\tau_\delta \sim 1$), the spectra appear to be described by a power-law with an exponent that is increasing from, roughly, 1.2 to 1.5, in absolute value, with increasing Reynolds number (*cf.* Ref. 15, Fig. 5.2). This progression with Reynolds number is easier to discern in Fig. 8, which plots the concentration spectra at $x/d = 100$, for $Re \times 10^{-4} = 1.25$ (solid line), 1.76 (dashed line), 2.55 (dot-2-dash), 3.6 (2-dot-2-dash), 5.1 (dot-dash), and 7.2 (2-dot-dash), with no offsets. The extent of the power-law regime can be seen to increase slightly with increasing Reynolds number. A similarly

increasing spectral slope (in absolute value) with Reynolds number was also noted in measurements of gas-phase spectra,²³ for $Re \times 10^{-4} = 0.5, 1.6,$ and 4.0 .

As can be seen by sighting along the spectra in Fig. 8, the power-law region is followed by a different regime at higher frequencies yet. This regime does not support the Batchelor k^{-1} prediction⁴ that should apply for over a decade and a half in frequency in this case (recall that $Sc \approx 1.9 \times 10^3$ here). This can be seen in Fig. 6, which includes a dotted line with a reference slope of $2/3$, corresponding to a k^{-1} spectrum. The spectra at increasing Reynolds number move even further from this slope, as can be seen by comparing the $Re = 1.2 \times 10^4$ spectrum with those at higher Reynolds numbers in Fig. 8. It should be noted that this conclusion extends to frequencies below $f\tau_\delta \simeq 2$, which are unaffected by resolution and compensation considerations.

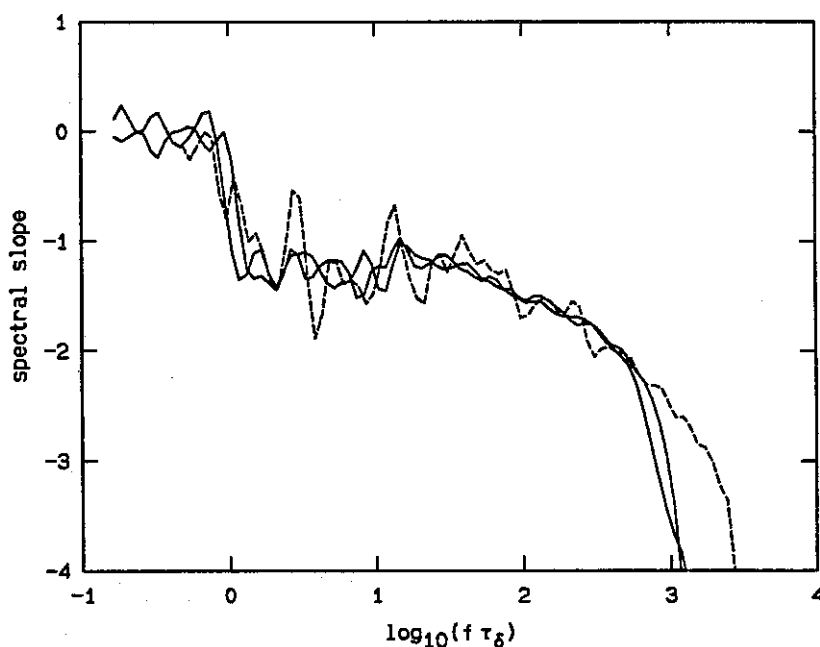


FIG. 9 Spectrum slope (logarithmic derivative). Solid lines: data at $x/d = 100$ and $Re = 1.25 \times 10^4$. Dashed line: $x/d = 305$, $Re = 1.2 \times 10^4$.

To facilitate the study of this higher frequency regime, we also computed the slope of the spectra (logarithmic derivative). A plot of spectrum slopes, for the lower Reynolds number data, appears in Fig. 9. These were derived from the two

$x/d = 100$, $Re = 1.25 \times 10^4$ spectra in Fig. 3 (solid lines) and the $x/d = 305$, $Re = 1.2 \times 10^4$ spectrum (dashed line). Their comparison helps assess issues of statistical convergence and confidence in this more delicate statistic, as well as the effects of spatial resolution and the applied compensation.

The plots in Fig. 9 suggest a frequency-dependence of the slope of the spectra that is close to a straight line, in these coordinates, for frequencies higher than $f\tau_\delta \simeq 1.2$, at this Reynolds number. This linear behavior extends for a decade and a half and into frequencies beyond which the data are limited by resolution and signal-to-noise considerations. The straight line appears to be a good representation for frequencies below $f\tau_\delta \approx 2$, for which the effects of compensation were negligible even for the $x/d = 100$ data (*cf.* Fig. 3). For frequencies above $f\tau_\delta \simeq 2$, the same straight line also describes the behavior for both the $x/d = 100$ and $x/d = 305$ data, which were affected by resolution (and compensation) to a different extent (*cf.* Figs. 3 and 5).

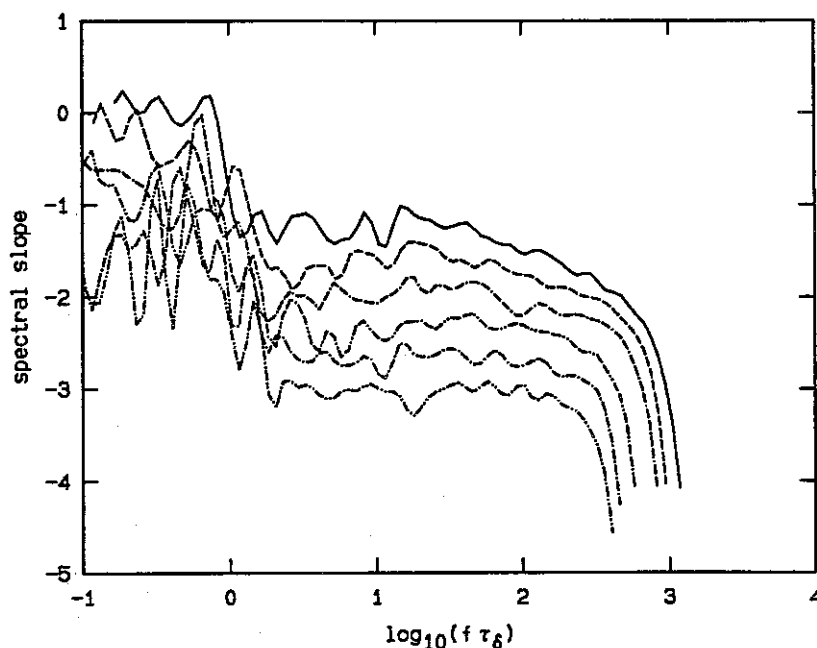


FIG. 10 Slope (logarithmic derivative) of spectra from data at $x/d = 100$ and $1.25 \leq Re \times 10^{-4} \leq 7.2$. Spectra offset as in Fig. 7. Line types as in Fig. 8.

A straight line for the logarithmic derivative of the spectrum corresponds to a spectrum that is parabolic in log-log coordinates, or log-normal in linear coordinates, *i.e.*,

$$S_c(f\tau_\delta) \propto \exp \left\{ -\frac{1}{2} [a \ln(f\tau_\delta) + b]^2 \right\} . \quad (18)$$

This expression, rather than a k^{-1} power law, seems to be the appropriate description of our jet fluid concentration spectra at high frequencies, over a range of frequencies at least as large as \sqrt{Sc} , *i.e.*, a decade and a half, in this case.

Figure 10 plots the local slope (logarithmic derivative) of the spectra in Fig. 8. The offset scheme employed in Fig. 7, and line-types employed in Fig. 8, were also used here. Straight lines can be seen to be a good representation for the spectrum slope at high frequencies with Reynolds number dependent values of the parameters a and b in Eq. 18. The end of the power-law regime and the beginning of the log-normal range can be seen to shift to higher frequencies with increasing Reynolds number. Our data admit a Kolmogorov scaling for the Reynolds number dependence of this transition frequency, *i.e.*, $Re^{3/4}$, but corresponding to the convection (passage frequency) of a physical scale roughly 80 times larger than the estimated Kolmogorov scale (computed using the estimated mean centerline energy dissipation²⁵ and the kinematic viscosity). This transition is not very well defined, however, and other Reynolds number scaling possibilities cannot be ruled out.

5. Conclusions

This work has investigated temporal scalar (jet fluid concentration) power spectra on the centerline of high Schmidt number turbulent jets, in the Reynolds number range $1.2 \leq Re \times 10^{-4} \leq 7.2$. Our spectra exhibit a power-law regime at frequencies above the local large scale passage frequency, with a Reynolds number dependent exponent increasing (in absolute value) from, roughly, -1.2 to -1.5 over the Reynolds number range investigated. This corroborates a similar finding for gas-phase jet fluid concentration spectra measured at comparable Reynolds numbers.²³ At higher frequencies, the spectra are well represented by a log-normal relation with Reynolds number dependent coefficients. While our data admit a Kolmogorov-like

scaling for the beginning of the log-normal region in the spectrum, *i.e.*, $\sim Re^{3/4}$, other possibilities cannot be ruled out.

We appreciate that our results are at odds with the classical picture of high Schmidt number scalar spectra. We do not find a $-5/3$ power-law regime, even though our measurements were conducted at Reynolds numbers where such behavior has previously been reported for high Schmidt number jet fluid scalar spectra.²⁶ Finally, despite adequate resolution and signal-to-noise ratio, our data do not support the Batchelor k^{-1} power-law prediction.⁴ Specifically, we found no constant k^{-1} slope at high frequencies and a spectral slope that does not even locally attain a value of -1 .

On the whole, our scalar spectra are rather similar to those derived by Gargett from ocean measurements.¹¹ In conjunction with her data and analysis, the current results raise further questions about the universal descriptions of scalar spectra, and their applicability to some of the canonical flows, such as turbulent jets.

Acknowledgments

We would like to acknowledge contributions by Dan Lang and David Dowling to the experiments. This work was supported by AFOSR Grants No. 83-0213 and 88-0155, and GRI Contract No. 5087-260-1467.

References

- ¹ Kolmogorov, A. N., "Local Structure of Turbulence in an Incompressible Viscous Fluid at Very High Reynolds Numbers," *Dokl. Akad. Nauk SSSR* **30**, 299 (1941).
- ² Corrsin, S., "On the spectrum of isotropic temperature fluctuations in isotropic turbulence," *J. Appl. Phys.* **22**, 469-473 (1951).
- ³ Oboukhov, A. M., "Some specific features of atmospheric turbulence," *J. Fluid Mech.* **13**, 77-81 (1962).

- ⁴ Batchelor, G. K., "Small-scale variation of convected quantities like temperature in turbulent fluid. Part 1. General discussion and the case of small conductivity," *J. Fluid Mech.* **5**, 113–133 (1959).
- ⁵ Monin, A. S., and Yaglom, A. M., *Statistical Fluid Mechanics: Mechanics of Turbulence II* (Ed. J. Lumley, MIT Press, Cambridge, MA, 1975).
- ⁶ Gibson, C. H., "Kolmogorov similarity hypotheses for scalar fields: sampling intermittent turbulent mixing in the ocean and galaxy," *Proc. Roy. Soc. A* **434**, 149–164 (1991).
- ⁷ Chapman, D. R., "Computational Aerodynamics Development and Outlook," *AIAA J.* **17**(12), 1293–1313 (1979).
- ⁸ Batchelor, G. K., Howells, I. D. , and Townsend, A. A., "Small-scale variation of convected quantities like temperature in turbulent fluid. Part 2. The case of large conductivity," *J. Fluid Mech.* **5**, 134–139 (1959).
- ⁹ Gibson, C. H., and Schwarz, W. H., "The universal equilibrium spectra of turbulent velocity and scalar fields," *J. Fluid Mech.* **16**, 365–384 (1963).
- ¹⁰ Grant, H. L., Hughes, B. A., Vogel, W. M., and Moilliet, A., "The spectrum of temperature fluctuations in turbulent flow," *J. Fluid Mech.* **34**, 423–442 (1968).
- ¹¹ Gargett, A. E., "Evolution of scalar spectra with the decay of turbulence in a stratified fluid," *J. Fluid Mech.* **159**, 379–407 (1985).
- ¹² Gibson, C. H., "Fossil turbulence and intermittency in sampling oceanic mixing processes," *J. Geophys. Res.* **92**, C5, 5383–5404 (1987).
- ¹³ Komori, S., Kanzaki, T., Murakami, Y., and Ueda, H., "Simultaneous measurements of instantaneous concentrations of two species being mixed in a turbulent flow by using a combined laser-induced fluorescence and laser-scattering technique," *Phys. Fluids A* **1**(2), 349–352 (1989).
- ¹⁴ Miller, P. L., and Dimotakis, P. E., "Reynolds number dependence of scalar fluctuations in a high Schmidt number turbulent jet," *Phys. Fluids A* **3**(5), 1156–1163 (1991).
- ¹⁵ Miller, P. L., *Mixing in High Schmidt Number Turbulent Jets*, Ph.D. thesis, California Institute of Technology (1991).

- ¹⁶ Dimotakis, P. E., and Miller, P. L., "Some consequences of the boundedness of scalar fluctuations," *Phys. Fluids A* 2(11), 1919–1920 (1990).
- ¹⁷ Miller, P. L., and Dimotakis, P. E., "Stochastic geometric properties of scalar interfaces in turbulent jets," *Phys. Fluids A* 3(1), 168–177 (1991).
- ¹⁸ Ware, B. R., Cyr, D., Gorti, S., and Lanni, F., "Electrophoretic and Frictional Properties of Particles in Complex Media Measured by Laser Light Scattering and Fluorescence Photobleaching Recovery," *Measurement of Suspended Particles by Quasi-Elastic Light Scattering* (Wiley, NY), 255–289 (1983).
- ¹⁹ Blake, W. K., *Mechanics of Flow-Induced Vibration. II* (Academic Press, Orlando, FL, 1986).
- ²⁰ Young, F. R., *Cavitation* (McGraw-Hill, London, 1989).
- ²¹ Dowling, D. R., Lang, D. B., and Dimotakis, P. E., "An Improved Laser-Rayleigh Scattering Photodetection System," *Exp. in Fluids* 7(7), 435–440 (1989).
- ²² Chen, C. J., and Rodi, W., *Vertical Turbulent Buoyant Jets. A Review of Experimental Data* (Pergammon Press, Oxford, 1980).
- ²³ Dowling, D. R., and Dimotakis, P. E., "Similarity of the concentration field of gas-phase turbulent jets," *J. Fluid Mech.* 218, 109–141 (1990).
- ²⁴ Dowling, D. R., *Mixing in Gas Phase Turbulent Jets*, Ph.D. thesis, California Institute of Technology (1988).
- ²⁵ Friehe, C. A., Van Atta, C. W., and Gibson, C. H., "Jet turbulence: Dissipation rate measurements and correlations," *AGARD Turbulent Shear Flows CP-93*, 18.1–7 (1971).
- ²⁶ Becker, H. A., Hottel, H. C., and Williams, G. C., "The Nozzle-Fluid Concentration Field of the Round Turbulent, Free Jet," *J. Fluid Mech.* 30(2), 285–303 (1967).

APPENDIX B

DIMOTAKIS, P. E. 1993 "Some issues on turbulent mixing and turbulence," W. C. Reynolds' 60th birthday Turbulence Symposium (22-23 March 1993, Monterey, CA), GALCIT Report FM93-1a.

Some issues on turbulent mixing and turbulence

Paul E. Dimotakis

*Graduate Aeronautical Laboratories
California Institute of Technology
Pasadena, California 91125*

Abstract

Recent data on turbulent mixing suggest that the mixing transition, previously documented to occur in shear layers, also occurs in jets, as well as many other flows, and can be regarded as a universal phenomenon. The resulting, fully-developed turbulent flow requires a minimum Reynolds number of $Re \approx 10^4$, or a Taylor Reynolds number of $Re_T \approx 10^2$, to be sustained. Turbulent mixing in this fully-developed state does not appear to be universal, however, with a qualitatively different behavior between shear layers and jets.

Presented at the Turbulence Symposium in honor of W. C. Reynolds' 60th birthday
22–23 March 1993, Monterey, California

GALCIT Report FM93-1a

17 March 1993

Revised: 6 July 1993

1. Introduction

A correct description of turbulent mixing is particularly taxing on our understanding of turbulence; such a description relies on an account of the full spectrum of scales. Specifically, to describe the *entrainment* stage that is responsible for the engulfment of large pockets of irrotational fluid species into the turbulent flow region,¹ the large scale flow structures need to be correctly described. Secondly, to describe the subsequent kinematic *stirring* process that is responsible for the large interfacial surface generation between the mixing species, the intermediate range of scales must be correctly accounted for. These are below the largest in the flow in size, but above the smallest affected by viscosity and molecular diffusivity. Finally, the dynamics at the smallest scales must be captured to describe the *molecular mixing* process itself. These three phases of turbulent mixing were clearly identified as “more or less distinct stages” in the 1948 description of mixing by Eckart,² who dubbed them as the *initial*, *intermediate*, and *final* stages, respectively. In the case of mixing of high Schmidt number fluids, *i.e.*, fluids characterized by a molecular diffusivity, \mathcal{D} , that is much smaller than the kinematic viscosity, ν , it is also useful to distinguish between the vorticity-diffusion stage, whereby velocity gradients are removed, and the species-diffusion stage, which removes scalar gradients.³

On the other side, successful descriptions and models of mixing provide us with tests of aspects of turbulent flow that are difficult to probe by other means — experimentally, numerically, or theoretically — at the high Reynolds numbers of interest here.

An exciting discussion in the context of mixing by chaotic advection has been taking place during the last decade. See, for example, Refs. 4–7, as well as several papers from the 1990 *IUTAM Symposium on Fluid Mechanics of Stirring and Mixing* (Published in *Phys. Fluids A* 5, Part 2, May 1991). There is little doubt that this progress will contribute to our understanding in the context of the broader issues of turbulent mixing. The present discussion, however, will be limited to flows at Reynolds numbers that are high enough for the turbulence to be regarded as fully-developed. In that regime, the impact of the recent progress in the behavior of deterministic, chaotic systems has yet to be felt, in my opinion.

As a practical matter, fully-developed turbulent flow typically requires that the local flow Reynolds number, *i.e.*,

$$Re(x) = \frac{U(x)\delta(x)}{\nu} \quad (1)$$

must be high enough. Generally speaking, turbulence cannot be sustained if the (local) Reynolds number falls below some minimum value, Re_{\min} . In the expression in Eq. 1, the characteristic velocity, $U(x)$, and transverse extent of the flow, $\delta(x)$, are to be taken as local values.

The main part of the discussion will be drawn from turbulent mixing in the far field of nonaccelerating (negligible streamwise pressure gradient) shear layers and jets. While these two flows are similar, in many ways, they are sufficiently different in others to be useful as test beds of ideas and prospects for universal descriptions of turbulent mixing behavior. The phenomena are found to have a broader manifestation, however, with conclusions relevant to turbulent flow in general.

In the case of shear layers, the characteristic velocity will be taken as the (constant) freestream velocity difference, *i.e.*, $U_{sl}(x) = \Delta U \neq \text{fn}(x)$, whereas the characteristic length will be taken as the local shear layer width, *i.e.*, $\delta_{sl}(x) \propto x$. Assuming constant fluid properties, *i.e.*, $\nu = \text{const.}$, this yields a local Reynolds number for shear layers that increases linearly with the streamwise coordinate, *i.e.*,

$$Re_{sl}(x) \propto x . \quad (2a)$$

In the case of jets, the characteristic velocity will be taken as the local centerline velocity of the jet, *i.e.*, $U_j(x) = u_c(x) \propto x^{-1}$, while the local length scale will be taken as the local jet diameter, *i.e.*, $\delta(x) = \delta_j(x) \propto x$, yielding a local jet Reynolds number that is a constant of the flow, *i.e.*,

$$Re_j(x) \neq \text{fn}(x) . \quad (2b)$$

This difference between shear layers and jets in the dependence of the local Reynolds number is interesting in the context of spatially developing flows and the evolution of the distribution of scales and turbulence spectra.

As we increase the flow Reynolds number, from small values to values approaching some minimum Reynolds number for fully-developed turbulence, the flow is able to generate ever-increasing interfacial area between the mixing species, increasing mixing and, in the case of chemically-reacting flow, chemical product formation and heat release. Beyond this transition region, *i. e.*, for $Re \gg Re_{\min}$, the Reynolds number dependence of the amount of mixed fluid can be expected to be weaker. In fact, a tenet of fully-developed turbulent flow theory is that, at high enough Reynolds numbers, the dependence of the various mean flow quantities on Reynolds number should become negligible, or vanish.

On the other hand, mixing depends on the behavior of *gradients* in the flow as well as concentration of diffusing species and the “principle of self-similarity with respect to Reynolds number cannot be expected to be applicable . . . , since these gradients are determined by small-scale fluctuations.” (Ref. 8, p. xvi) We will examine these propositions by comparing the outcome of experimental investigations on turbulent mixing conducted in both gas- and liquid-phase shear layers and jets.

2. Transition Reynolds numbers in shear layers and jets

A qualitative difference in the appearance of the scalar field is observed across the transition in a shear layer to a more well-mixed state, as the Reynolds number is increased, as illustrated in Fig. 1. The transition to a more well-mixed state in a gas-phase turbulent shear layer was documented by Konrad,⁹ who used an aspirating probe¹⁰ to estimate the local value of the high-speed stream fluid fraction, averaged over the resolution volume and time-response of the aspirating probe. Subsequent estimates of mixing and chemical product volume fraction in liquid-phase shear layers,¹¹ using a pH indicator, as well as estimates derived from probability-density functions (pdf's) measured using laser-induced fluorescence techniques,¹² documented the same behavior.

The results from the two liquid-phase shear layer measurements are plotted in Fig. 2, which depicts the estimated chemical product thickness as a function of the local Reynolds number at the measuring station. A marked increase in



FIG. 1 Laser-induced fluorescence streak images of the scalar field in a liquid-phase shear layer, for $Re \simeq 1.75 \times 10^3$ (left) and $Re \simeq 2.3 \times 10^4$ (right). Data from Ref. 12, Figs. 7 and 9, respectively.

the estimated chemical product can be seen to occur at $Re \approx 10^4$. This is also associated with a change in the pdf of the scalar fluctuations. In the pretransition region, the pdf of the conserved scalar in the flow is dominated by the near-delta-function contributions of the unmixed (pure) fluid from each of the freestreams.¹² In the posttransition regime, the composition of the mixed fluid across the layer develops a preferred value that is well-correlated with the one inferred from the estimated overall entrainment ratio for the layer.^{3,12} The pdf evolves from one limit to the other in the course of this transition (*cf.* Ref. 12, Sec. 5.4, and Ref. 13), with a relatively long memory of the (typically, much larger) initial asymmetry in the relative amounts of each of the freestream fluids.

As noted in the discussions of these experiments,^{11,12} finite resolution limitations in these liquid-phase experiments overestimated the absolute amount of chemical product by, roughly, a factor of two, as confirmed in chemically-reacting experiments which measured the chemical product volume fraction directly.¹² Nevertheless, the documented increase in the amount of mixing at the transition Reynolds number is qualitatively correct and was found to occur at the same Reynolds number in both gas- and liquid-phase shear layers.¹⁴

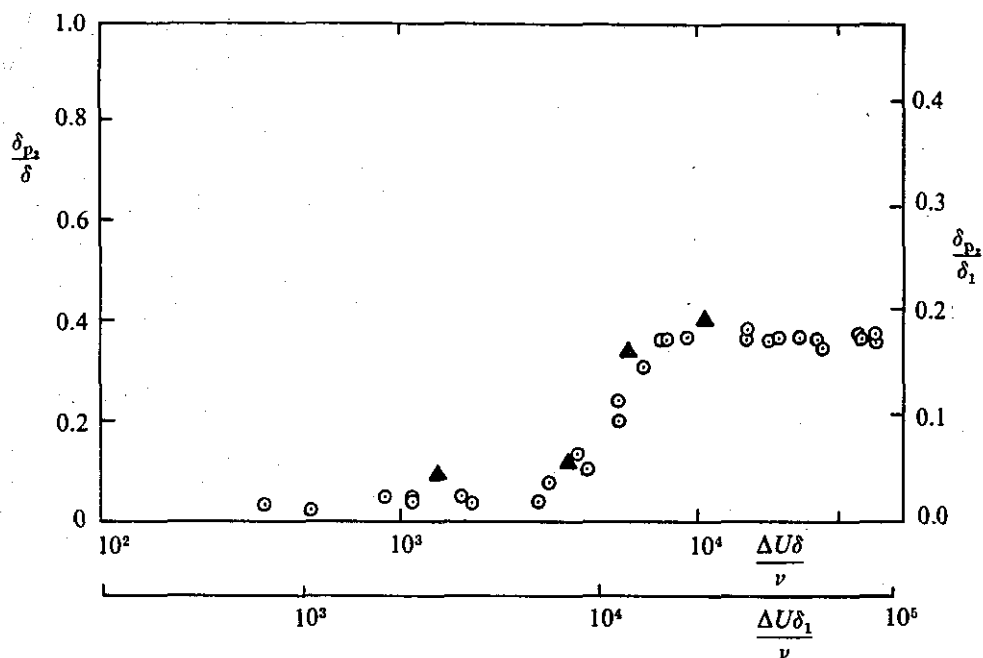


FIG. 2 Reynolds number dependence of chemical product volume fraction, in a liquid-phase shear layer, in the vicinity of the mixing transition.¹² Note that absolute values are overestimated in both experiments (see text).

The transition to a more well-mixed state, in these experiments, was correlated with the appearance of streamwise vortices and the ensuing transition to three-dimensionality of flow that is nominally two-dimensional in the initial region.¹¹⁻¹⁵ See discussion in the review paper by Roshko.¹⁶ Corroborating evidence was also found in the numerical simulations of time-developing shear layers by Moser & Rogers that followed the developing flow to sufficiently high Reynolds numbers to document the beginning of this behavior.¹⁷

The transition to a more well-mixed state in turbulent jets is less conspicuous than in shear layers. Turbulent jets being three-dimensional, even at low Reynolds numbers, such a transition is not correlated with a transition to three-dimensionality in the flow field. Nevertheless, there is, again, a qualitative difference in the appearance of the scalar field for values of the Reynolds number that are lower than $Re_{\min} \approx 10^4$ and values that are comparable to that, or higher. This is illustrated in the laser-induced fluorescence images in Fig. 3, of the jet-fluid concentration in the plane of symmetry of liquid-phase jets.¹⁸ Unmixed reservoir fluid (black) can be seen throughout the turbulent region and, in particular, all the way to the jet axis

in the lower Reynolds number (left) image at $Re_j \simeq 2.5 \times 10^3$ (imaged field spans $0 < x/d < 35$, where d is the jet nozzle diameter). This is not the case in the higher Reynolds number (right) image at $Re_j \simeq 10^4$ (imaged field spans $0 < x/d < 200$), in which jet fluid of varying concentrations can be seen to be more volume-filling within the turbulent region.

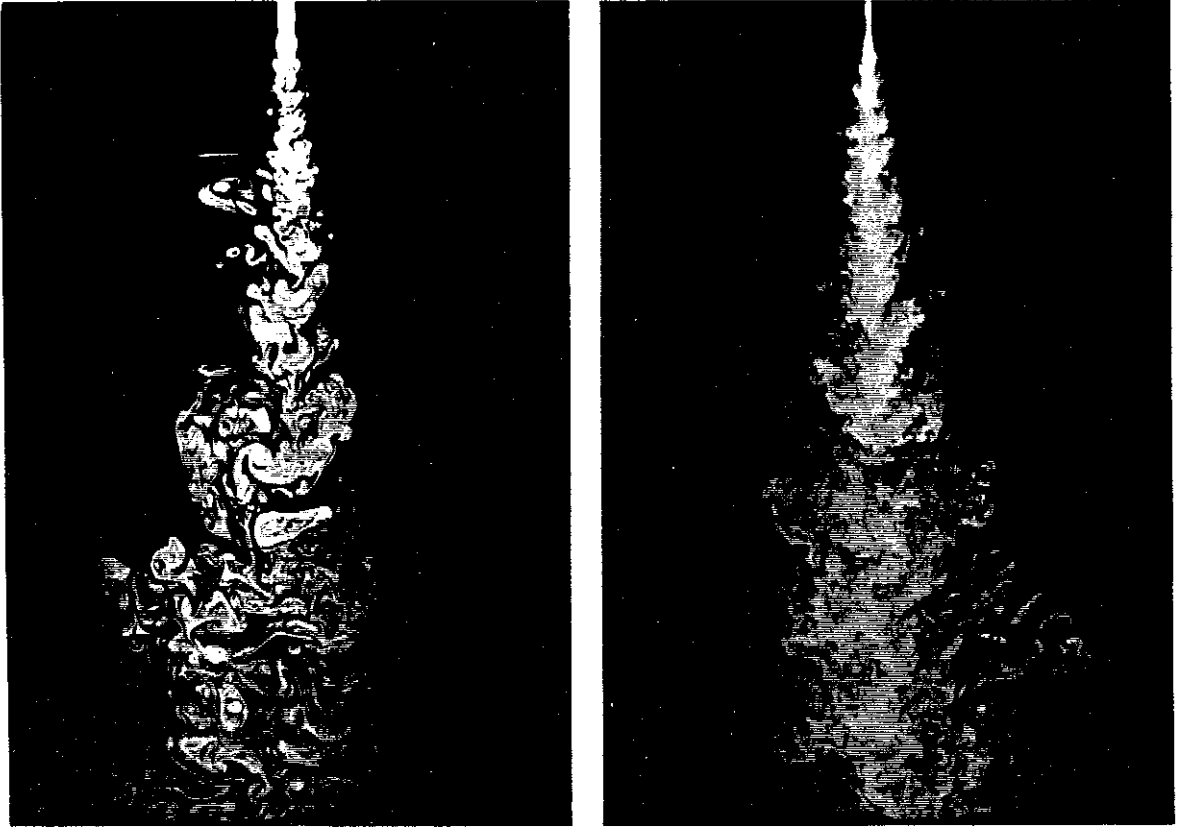


FIG. 3 Jet-fluid concentration in the plane of symmetry of a round turbulent jet. Left image: $Re_j \simeq 2.5 \times 10^3$ ($0 < x/d < 35$). Right image: $Re_j \simeq 10^4$ ($0 < x/d < 200$). Data from Ref. 18, Figs. 5 and 9.

Seitzman *et al.*¹⁹ investigated the outer entrainment and mixing region, using laser-induced fluorescence images of OH radicals in a H_2 -air turbulent diffusion flame. A qualitative evolution in the complexity of the thin burning regions can be seen, as the Reynolds number was increased from 2.3×10^3 to 4.95×10^4 (*cf.* their Fig. 3). In these experiments, this evolution is also influenced by decreasing

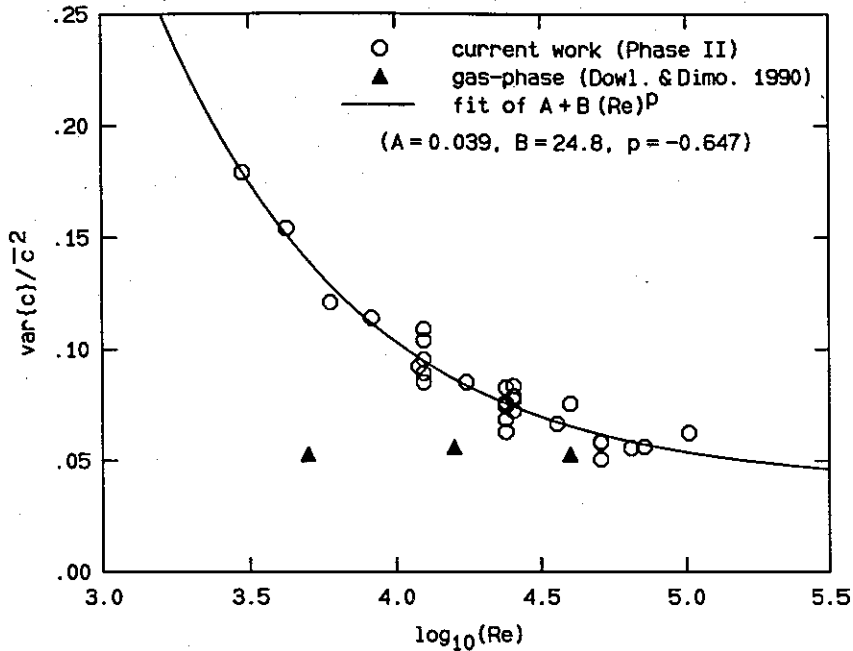


FIG. 4 Normalized variance of jet-fluid concentration on the axis of a turbulent jet, as a function of the jet Reynolds number (Ref. 22, Fig. 7.2). Circles: Liquid-phase jets.²² Triangles: Gas-phase jets.²⁰

buoyancy and the decreasing relative importance of baroclinic vorticity generation, as the Reynolds number was increased, and is, therefore, not entirely attributable to Reynolds number effects.

Similar behavior is reflected in the measurements of the rms of the scalar (jet fluid concentration) fluctuations on the axis, in the far field of gas- and liquid-phase jets, as a function of jet Reynolds number.²⁰⁻²² The data, in the form of the normalized scalar fluctuation variance, are plotted in Fig. 4 (Ref. 22, Fig. 7.2). The liquid-phase data exhibit a decrease in the fluctuation level with Reynolds number, with a rather less sensitive dependence for Reynolds numbers higher than $Re \approx 2 \times 10^4$, or so. Noting that lower fluctuation levels correspond to more homogeneous mixing, *i.e.*, a pdf of concentration values that are more tightly clustered around the local mean, we see that, at least for the case of a liquid-phase jet, the flow transitions to a more well-mixed state as the Reynolds number is increased, as in the shear layer, even though in a more gradual manner (*cf.* Fig. 2). A much weaker Reynolds number dependence of the normalized scalar variance can be seen for the gas-phase-jet data.

The Reynolds number dependence of turbulent mixing and chemical product formation in turbulent jets was recently investigated in gas-phase jets.^{23,24} In this context, the turbulent diffusion flame length, L_f , is important and marks the distance from the nozzle required to mix and burn the reactant carried by the jet fluid. If the stoichiometry of the jet/reservoir reactants and jet entrainment are held constant, and for fast chemical kinetics (high Damköhler number limit), the flame length dependence on the various flow parameters provides us with a measure of the dependence of mixing on those parameters. Decreasing flame lengths, for example, imply faster (better) mixing.

The dependence of the flame length on the stoichiometry of the jet-/reservoir-fluid chemical system must first be factored in the analysis. In particular, for a momentum-dominated, turbulent jet diffusion flame, the flame length is linearly dependent on the (mass) stoichiometric mixture ratio (*e.g.*, Refs. 25–27), *i.e.*,

$$\frac{L_f}{d^*} \simeq A \phi_m + B, \quad (3)$$

where ϕ_m is the mass of reservoir fluid required to completely consume a unit mass of jet fluid. The measurements must then be regarded as investigations of the behavior of the stoichiometric coefficient, A , and normalized virtual origin (intercept), B , and their dependence, in turn, on the flow parameters.

In these experiments, long platinum wires were stretched across the turbulent diffusion flame and spaced in equal logarithmic increments along the jet axis. These permitted the line-integral of the temperature rise, $\Delta T(x, y)$, due to heat released in the chemical reaction, to be measured along the y -coordinate (transverse to the jet axis), as a function of the downstream coordinate. See Fig. 5.

The experiments utilized the $F_2 + NO$ chemical reaction, with F_2 diluted in N_2 forming the jet fluid, and NO diluted in N_2 forming the quiescent reservoir fluid. With this chemical system, an adiabatic flame temperature rise, ΔT_f , as low as 7 K was realized (with the reaction still in the fast-kinetic regime). Such low values were dictated by the results of a separate investigation that assessed the effects of buoyancy and ascertained that the measurements were realized in the momentum-dominated regime for this heat-releasing flow. The Reynolds number was varied by varying the pressure in the combustion vessel.

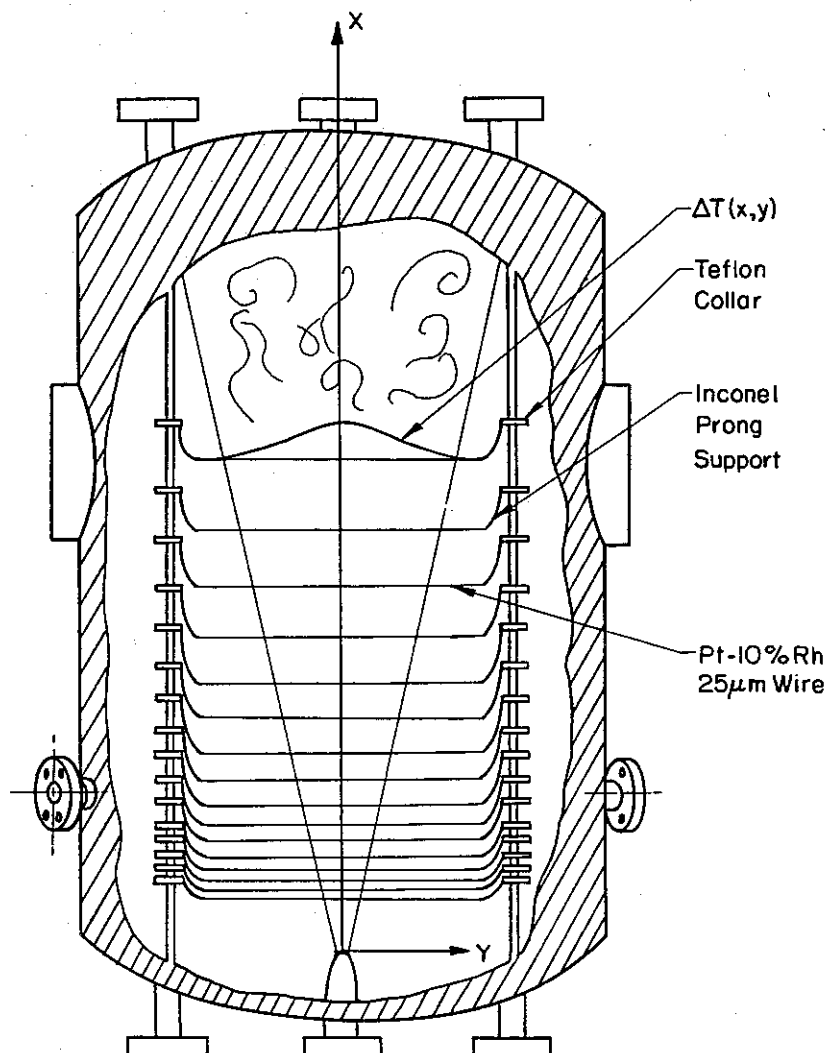


FIG. 5 Turbulent jet diffusion flame combustion vessel schematic, indicating the jet and the logarithmically-spaced temperature-sensing wire array.

If the temperature rise, $\Delta T(x, y)$, in the chemically-reacting jet is normalized by ΔT_f , the adiabatic flame temperature rise for the reaction, the line integral across the jet axis can be used to form a product thickness, $\delta_P(x)$, analogous to the one defined for shear layers, *i.e.*,

$$\delta_P(x) \equiv \int_{-\infty}^{\infty} \frac{\Delta T(x, y)}{\Delta T_f} dy \quad (4)$$

(*cf.* Ref. 28, Sec. 3.1.3; Ref. 29, Sec. 1.9; and Ref. 30, Eqs. 41 and discussion following). Sample data are depicted in Fig. 6, for a range of values of the (mass)

stoichiometric mixture ratio, ϕ_m . The data plot the product thickness δ_P , normalized with the length, L_w , of the platinum resistance wire used to measure the line integral, versus the logarithm of x/d^* , where d^* is the jet source diameter.²⁷

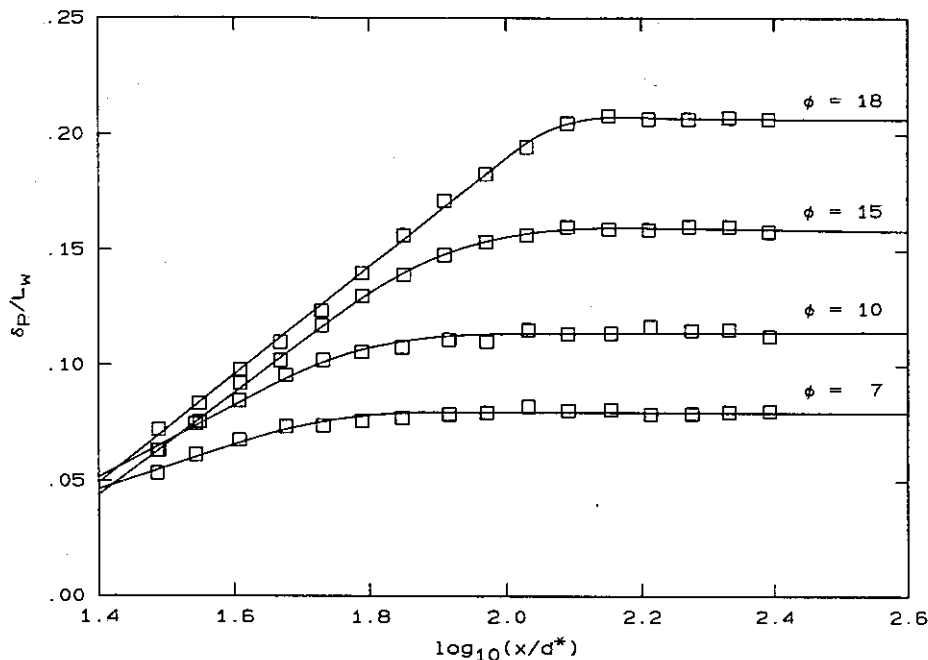


FIG. 6 Product thickness *vs.* $\log_{10}(x/d^*)$, for several stoichiometric mixture ratios (Ref. 24, Fig. 5).

To analyze these data, we note that for regions of the flow well upstream of the flame length, *i.e.*, for $x \ll L_f$, the entrained reactant is consumed on, or just outside, the boundary of the turbulent region. There, the turbulent fluid is jet-fluid-reactant rich and it need comprise only a small fraction of the mixed fluid to consume the entrained reservoir-fluid-reactant. The diffusion/reaction process then takes place in a relatively thin peripheral reaction zone at $y = \pm R_r(x)$,^a whose ensemble-averaged radius, $R_r(x)$, is proportional to x . As a consequence, the line integral of the time-averaged temperature rise across the turbulent region increases as the chemical reaction releases heat in the thin reaction zones at the edges of the turbulent region.

^a This picture is corroborated by the OH-images obtained by a number of investigators in H₂-air jet flames (*cf.* Refs. 19 and 31, for example).

It was conjectured that the radial integral of the temperature rise, at a given station x , increases in proportion to the entrainment velocity at that station, $u_e[R_r(x)]$, *i.e.*,

$$\frac{d}{dx} \int_0^\infty \Delta T(x, r) dr \propto u_e[R_r(x)] \Delta T_f, \quad (5)$$

or, for a momentum-driven, turbulent jet,

$$d \int_{-\infty}^\infty \frac{\Delta T(x, y)}{\Delta T_f} dy \propto \frac{dx}{2\pi R_r(x)} \propto \frac{dx}{x}. \quad (6)$$

Integrating this relation and scaling with the flame length L_f , we have

$$\frac{\delta_P(x \ll L_f)}{L_f} \simeq a \log\left(\frac{x}{L_f}\right) + b. \quad (7)$$

This dependence of the line integral on x suggested the logarithmic wire spacing used in the experiment and was used in the analytical form of the fit for the line-integrated, time-averaged, temperature-rise data (*cf.* Fig. 6).

Beyond the end of the flame region, *i.e.*, for $x > L_f$, no further heat is released and, in the absence of buoyancy effects, the temperature excess becomes a passively-convected scalar with a self-similar profile. In that case,

$$\Delta T(x, y) \simeq \Delta T(x, 0) f\left(\frac{y}{x}\right) \propto \frac{1}{x} f\left(\frac{y}{x}\right)$$

and the product thickness line integral becomes independent of the downstream coordinate, x , *i.e.*,

$$\delta_P(x > L_f) \propto \int_{-\infty}^\infty \frac{1}{x} f\left(\frac{y}{x}\right) dy \neq \text{fn}(x). \quad (8)$$

As can be seen in Fig. 6, the experimental results confirmed the conjecture for $x \ll L_f$. They were also consistent with the anticipated conserved-scalar behavior of the temperature rise for $x > L_f$, *i.e.*, a product thickness that asymptotes to a constant value. Such data allow us to estimate the flame length, L_f . In particular, one can accept an operational definition of L_f as the location where the product thickness line integral (Eq. 4) has attained 99% of its asymptotic value, as one does on the basis of a boundary layer velocity profile, for example.

Figure 7 (Ref. 23, Fig. 4.8) plots the stoichiometric coefficient, A , in the expression for the flame length (cf. Eq. 3), *i.e.*, the slope of the flame length *vs.* the stoichiometric mixture ratio ϕ_m . This can be regarded as the additional length, in units of the jet source diameter d^* , required to entrain, mix, and react with a unit increase in the stoichiometric ratio of the jet-/reservoir-fluid chemical system, *i.e.*,

$$A \equiv \frac{d}{d\phi_m} \left(\frac{L_f}{d^*} \right) . \quad (9)$$

In the fast kinetic regime, as was the case in these experiments, this quantity is a useful measure of mixing. It separates the self-similar, far-field behavior from that of the virtual origin in the overall mixing process.

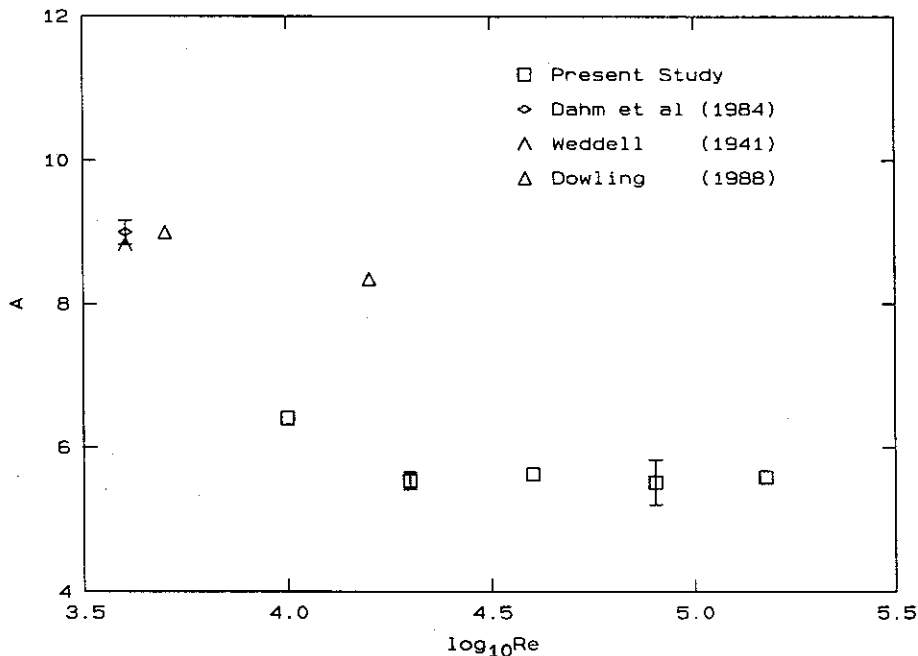


FIG. 7 Flame length stoichiometric coefficient A (Eq. 3). Squares: Gas-phase chemically-reacting jet data.²³ Diamond: Laser-induced fluorescence, liquid-phase data.³² Lambda: pH-indicator, liquid-phase data.^{25,33} Triangles: Flame length data inferred from gas-phase, nonreacting data (see text).³⁴

The data in Fig. 7 indicate that mixing in the far field of a turbulent jet improves relatively rapidly with increasing Reynolds number. Specifically, A decreases until a Reynolds number of, roughly, 2×10^4 , with a much weaker dependence on Reynolds

number, if any, beyond that. These data are in accord with the nonreacting, liquid-phase data in Fig. 4, which also indicate improved mixing up to Reynolds numbers of 2×10^4 , or so, with a weaker dependence beyond that. The latter data, however, do not permit the separation of the far-field and virtual-origin contributions to the overall mixing process, as do the chemically reacting jet data. We should also note that the near- and intermediate-field behavior, which contributes to the virtual origin of the mixing process and the resulting flame length, does not exhibit the same Reynolds number dependence.²³

A potential difficulty should be recognized between the inferred behavior based on the nonreacting, gas-phase jet data (triangles),³⁴ and the chemically-reacting, gas-phase data (squares).²³ Two observations are relevant here. The values estimated from the nonreacting gas-phase data (triangles) were derived assuming certain similarity properties of the concentration pdf and the virtual origin of the whole process (see discussion in Ref. 34, Sec. 5.4, and Ref. 21, Appendix B).

Partly as a consequence, as was also noted in the comparison between the data in Figs. 4 and 7, it is not possible to separate the contribution to the flame length of the (rather large) virtual origin of the mixing process, and its dependence on Reynolds number,²³ from the Reynolds number dependence of the far-field mixing process, *i.e.*, the dependence of the flame length stoichiometric coefficient, A .

While this may be a minor point, we may wish to note that transition Reynolds numbers for jets seem to be twice as large as for shear layers. On the one hand, the two flows are sufficiently different to admit differences in their behavior of a factor of 2, or so, in Reynolds number. On the other, however, if the characteristic large scale $\delta(x)$ chosen for the local Reynolds number definition of a jet is the local *radius*, as would be appropriate if the length scale in the general case is defined as the transverse spatial extent across which the shear is sustained, then the transition Reynolds number for jets becomes very close to that for shear layers.

3. Mixing in fully-developed turbulence

In fully-developed turbulent shear layers, beyond the mixing transition, mixing also exhibits a weaker dependence on Reynolds number. Figures 8a and 8b plot experimentally obtained data of the normalized chemical product thickness, *i.e.*,

$$\frac{\delta_P(x; \phi)}{\delta(x)} = \frac{1}{\delta(x)} \int_{-\infty}^{\infty} \frac{\Delta T(x, y; \phi)}{\Delta T_f(\phi)} dy \quad (10)$$

(*cf.* Eq. 4), for both low (Fig. 8a) and high (Fig. 8b) values of the stoichiometric mixture ratio ϕ . The stoichiometric mixture ratio, in this case, denotes the parts (moles) of high-speed fluid required to consume a part (mole) of low-speed fluid in the shear layer mixing zone (*e.g.*, Ref. 30). The product thickness data in Figs. 8a and 8b were normalized by the 1% temperature rise product thickness, δ_T , which has been found to be close to the visual thickness, δ_{vis} , of the shear layer.^{1,12,30,35}

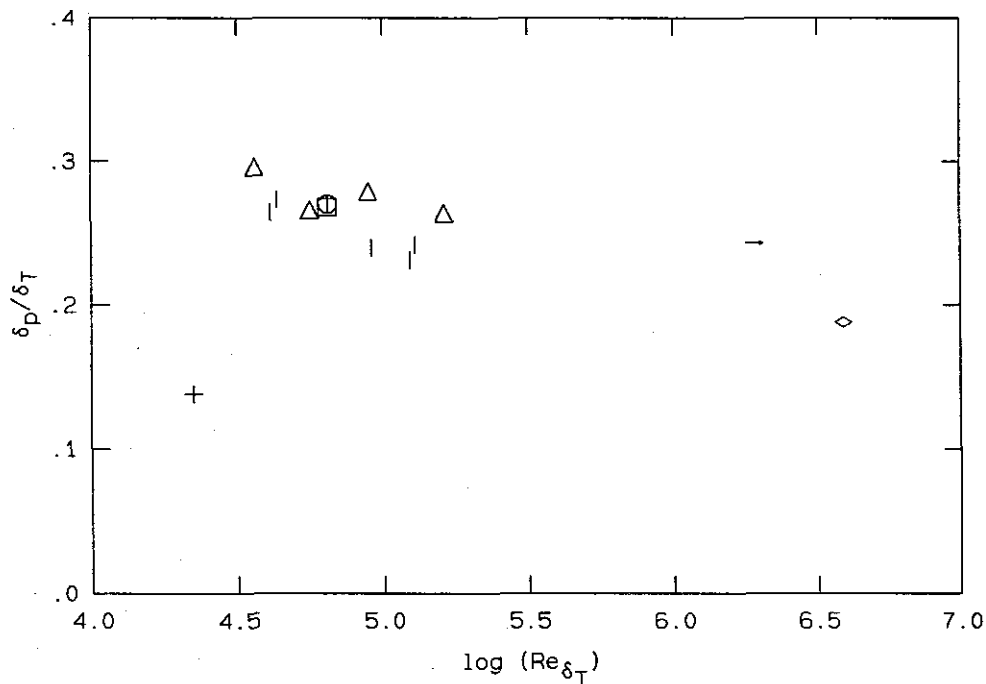


FIG. 8a Low- ϕ normalized product thickness *vs.* Reynolds number for a turbulent shear layer. Matched free-stream density, incompressible, gas-phase shear layers: $\phi = 1/8$ (square), $\phi = 1/4$ (circle).³⁵ Vertical lines: $\phi = 1/8$.³⁶ Triangles: $\phi = 1/8$.³⁷ Supersonic shear layers: $\phi = 1/4$, $\rho_2/\rho_1 = 0.71$, $M_c = 0.51$ (arrow); $\phi = 1/3$, $\rho_2/\rho_1 = 5.95$, $M_c = 0.96$ (diamond).³⁸ Liquid-phase shear layer: $\phi = 1/10$ (cross).¹²

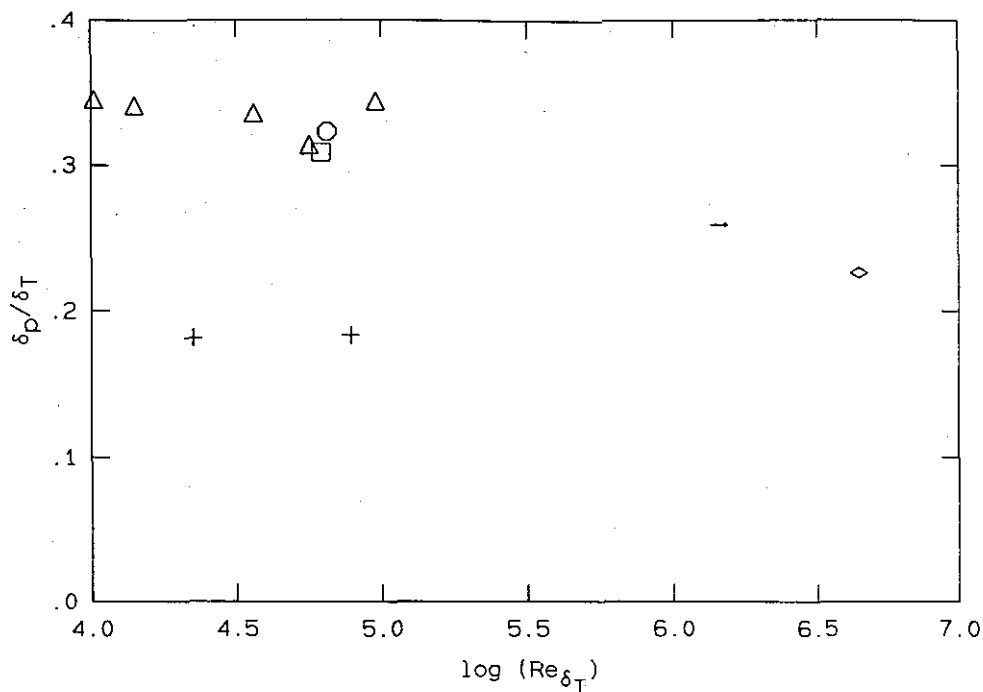


FIG. 8b High- ϕ shear layer normalized product thickness *vs.* Reynolds number. Matched free-stream density, incompressible, gas-phase shear layers: $\phi = 8$ (square), $\phi = 4$ (circle).³⁵ Triangles: $\phi = 8$.³⁷ Supersonic shear layers: $\phi = 4$, $\rho_2/\rho_1 = 0.71$, $M_c = 0.51$ (arrow); $\phi = 3$, $\rho_2/\rho_1 = 5.95$, $M_c = 0.96$ (diamond).³⁸ Liquid-phase shear layer: $\phi = 10$ (crosses).¹²

These data were all derived from chemically-reacting shear layer experiments, conducted in the fast chemical-kinetic regime, *i.e.*, high Damköhler number limit. In this limit, all molecularly mixed fluid produces chemical product, as dictated by the stoichiometry of the mixed fluid composition (*cf.* discussion in Ref. 30, Sec. IV).

The chemically reacting experiments were conducted for low and high values of the (molar) stoichiometric mixture ratio, ϕ , that can be expected to yield near-stationary values of the product thickness $\delta_p(\phi)$, with respect to ϕ . The chemical product thickness has a rather sensitive dependence on ϕ , as the stoichiometric mixture fraction, $\xi_\phi = \phi/(\phi + 1)$, approaches zero or unity, as a result of the regions near the delta functions corresponding to the pure fluid in the composition pdf.^{39,40} Data points indicated by crosses were derived from experiments in liquid-phase flows.¹² All other data were based on results from gas-phase flows. The plotted points based on the experiments by Frieler³⁷ and Hall *et al.*³⁸ were calculated by

Chris Bond from the original temperature-rise data.^b Data at the highest values of the Reynolds number were derived from chemically-reacting, supersonic shear layers ($M_1 > 1$, $M_2 < 1$)³⁸ and, as a consequence, can be assumed to be susceptible to the combined effects of compressibility as well as Reynolds number. We note here that even though the velocity ratio, $r \equiv U_2/U_1$, for the supersonic shear layer experiments was very low, and should perhaps not be included in the same plot as the subsonic shear layer experiments for which $r \simeq 0.4$, the *molar* entrainment ratio, E_n , *i.e.*, the ratio of the number of high-speed freestream fluid moles per mole of low-speed freestream fluid entrained, was estimated to be close to its value for the incompressible flow experiments. Specifically, for the incompressible flow experiments,^{3,12,35} $E_n \simeq 1.3$. The estimated values for the compressible shear layers were $E_n \simeq 1.07$, for the $M_c \simeq 0.51$ shear layer ($r \simeq 0.24$), and $E_n \simeq 1.2$, for the $M_c \simeq 0.96$ shear layer ($r \simeq 0.10$).^{38,41,42}

Several observations can be made on the basis of these data:

- a. In the limit of fast kinetics, the chemical product formed decreases as the Reynolds number increases. This implies less efficient mixing in fully-developed shear layers as the Reynolds number increases. Presently available data suggest that this is opposite the behavior exhibited by turbulent jets (recall data in Figs. 4 and 7, and related discussion).
- b. The data admit a Reynolds number dependence of the chemical product thickness for the low- ϕ case (Fig. 8a) that is stronger than the high- ϕ case (Fig. 8a).^c If this is proven to be the case, it would imply a complicated dependence of the pdf of compositions on Reynolds number.
- c. Liquid-phase shear layer mixing exhibits a weaker Reynolds number dependence than gas-phase shear layer mixing (*cf.* Fig. 8b). Unless the data for turbulent jets should all be regarded as not in fully-developed flow (*cf.* Fig. 4), this is also opposite the behavior found in turbulent jets.

^b Private communication.

^c Recall that, for these flows, the high-speed stream fluid is preferentially entrained.³

Based on the presently available scant experimental data and unless the region $2 \times 10^5 < Re < 10^6$ conceals a second transition to a Reynolds-number-independent turbulent mixing state,

- d. the trend in Figs. 8a and 8b suggests that, at least at low compressibility, *e.g.*, up to the lower of the two convective Mach numbers investigated, Reynolds number effects dominate compressibility effects.

The latter observation must be regarded as the most tentative and must await the results of further experimental investigations to be confirmed.

It is interesting that in the case of mixing in turbulent jets, gas-phase data for the flame length indicate only a weak Reynolds number dependence beyond the mixing transition, if any (Fig. 7). Measurements in liquid-phase jets, however, at Reynolds numbers as high as 7.2×10^4 , yield scalar spectra that have not converged to a Reynolds-number-independent state,⁴³ in accord with the data in Fig. 4.

Finally, it is noted that some of these observations are at variance with the inferences drawn in a review by Broadwell & Mungal,⁴⁴ of earlier data. The interested reader is directed to that discussion for further details.

4. Transition Reynolds numbers in other flows

The observations of mixing transitions in shear layers and jets suggest that a minimum Reynolds number may be required for turbulence to develop into a more well-mixed state in these flows. Specifically, we must have $Re > Re_{\min}$, with Re_{\min} in the neighborhood of 0.5×10^4 to 2×10^4 , for fully-developed turbulent flow. It is interesting that this value does not appear to be peculiar to the far-field behavior in turbulent jets and free-shear layers. Other flows also exhibit similar transitions at comparable values of the Reynolds number, as we'll discuss below.

Pipe flow, for example, transitions out of its slug/puff regime to a less intermittent, fully-turbulent state over a range of Reynolds numbers that depend on the entrance conditions. This sensitivity to initial conditions diminishes, however, at a Reynolds number in the vicinity of 10^4 .⁴⁵

The Coles' turbulent boundary layer wake parameter, Π , that scales the outer flow region of a turbulent boundary layer,⁴⁶ is found to increase with Reynolds number, for a zero-pressure-gradient boundary layer, attaining an asymptotic value of $\Pi = 0.620$ at a Reynolds number, based on displacement thickness,⁴⁷ of $Re \equiv U_\infty \delta^*/\nu \simeq 0.8 \times 10^4$. See Refs. 48 and 49, for a discussion, and Ref. 49, Table 4 and Fig. 6, for a compilation of low-speed, turbulent boundary-layer flow data.

In experiments by Liepmann & Gharib, in the near field of turbulent jets, the number of azimuthal nodes in vortex structures becomes difficult to identify beyond a certain Reynolds number, where the flow transitions to a much more chaotic state.⁵⁰ The authors correlate this transition with a laminar-turbulent transition in the jet nozzle boundary layers. It is also interesting, however, that it occurs at a Reynolds number very close to 10^4 .

In recent experiments on lifted-flame behavior, Hammer notes a change in the scaled lift-off height of turbulent jet flames at a jet Reynolds number, in the neighborhood of $Re \approx 1.8 \times 10^4$, beyond which the Reynolds number dependence is weaker. See data in Ref. 51, Fig. 3.8, and discussion following.

In his review of bluff-body flows, Roshko documents several regimes, as indicated by the behavior of the base pressure of a circular cylinder, as a function of Reynolds number.⁵² In particular, the (negative) base pressure is found to increase in the range of Reynolds numbers of $0.3 \times 10^4 < Re \equiv U_\infty d_{cyl}/\nu < 2 \times 10^4$ (Ref. 52, Fig. 1). Roshko attributes this behavior to a transition in the separating shear layers.

Measurements of the scaled turbulent kinetic energy dissipation rate,

$$\alpha = \frac{\varepsilon \ell}{u'^3}, \quad (11)$$

in flow behind square grids, where ε is the kinetic energy dissipation per unit mass, ℓ is the longitudinal length scale, and u' is the rms streamwise velocity fluctuation level, suggest that it decreases relatively rapidly with increasing Taylor Reynolds number,

$$Re_T \equiv \frac{u' \lambda_T}{\nu}, \quad (12a)$$

where λ_T is the Taylor microscale, until a value of $Re_T \approx 70$, and then becomes much less sensitive to Reynolds number, attaining a value of $\alpha \approx 1$ at higher Reynolds numbers. This value may not be universal, however, with measured values in the range $1 < \alpha < 2.7$ behind non-square grids.⁵³

A similar conclusion was arrived at by Jimenez *et al.*,⁵⁴ in their numerical simulations of turbulence in a spatially-periodic cube, in the range $36 < Re_T \leq 170$. They report a value of $\alpha \simeq 0.65$ attained for $Re_T \geq 95$. Since

$$Re_T \approx Re^{1/2}, \quad (12b)$$

it, again, appears that $Re > Re_{\min} \approx 10^4$ is a necessary condition for fully-developed turbulent flow.⁵⁵

In thermal convection, a transition from “soft turbulence” to “hard turbulence” has been noted for Rayleigh numbers given by $Ra \approx 10^8$, that is marked by a qualitative change in the pdf of the measured temperature fluctuations.⁵⁶ Since $Re \approx Ra^{1/2}$ for this flow,⁵⁷ we again recover a minimum Reynolds number boundary of the fully-developed turbulent state at $Re \approx 10^4$.

Careful experiments were recently performed that measured the torque in Couette-Taylor flow, in the range of Reynolds numbers of $800 < Re < 1.23 \times 10^6$.^{58,59} These experiments revealed a “well-defined, non-hysteretic transition” in a narrow range of Reynolds numbers, $10^4 < Re_{tr} < 1.3 \times 10^4$. The flow was found to be qualitatively different, below and above this transition, as illustrated in the flow-visualization data reproduced in Fig. 9, with pre- and post-transition differences reminiscent of the corresponding ones in jets (*cf.* Fig. 3). See also additional flow-visualization data in Ref. 58, Figs. 1a,b. Beyond this transition, the dependence of the torque on Reynolds number becomes progressively weaker. Significantly, however, the torque does not attain viscosity-independent behavior to the highest Reynolds numbers investigated.

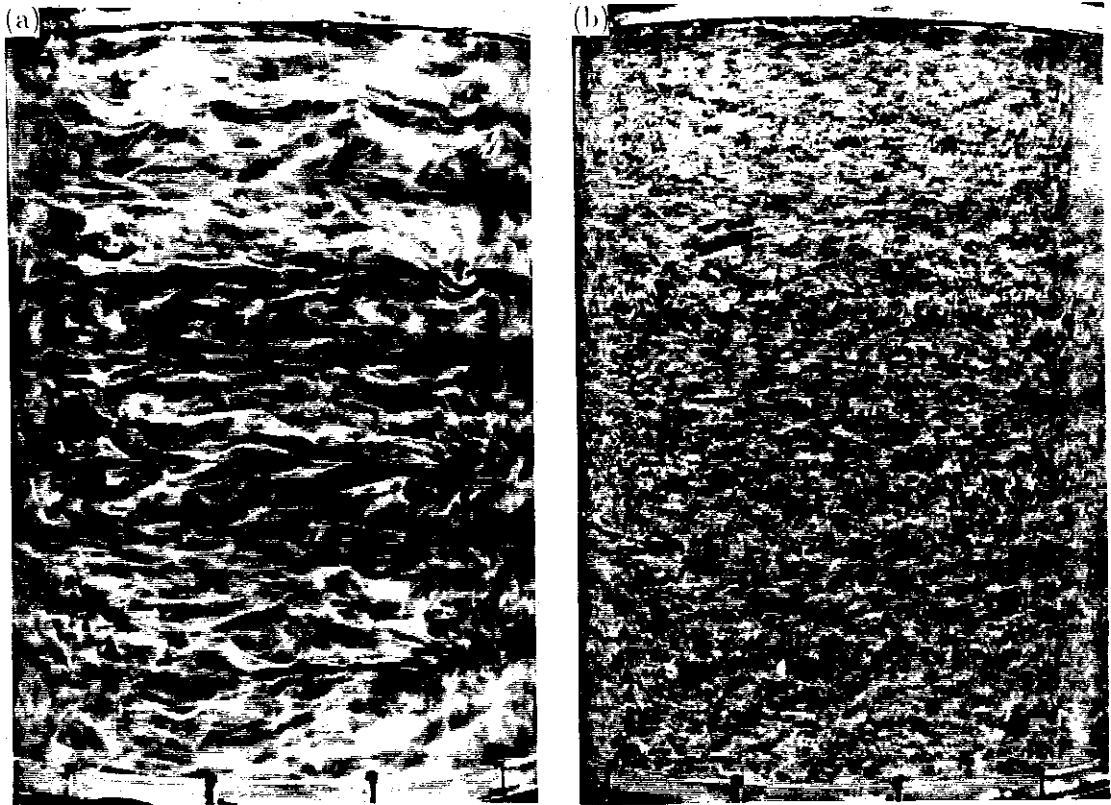


FIG. 9 Couette-Taylor flow-visualization data at (a) $Re = 0.6 \times 10^4$, and (b) $Re = 2.4 \times 10^4$. From Ref. 59, Figs. 5a,b, reproduced by kind permission of Prof. H. Swinney.

5. A criterion for fully-developed turbulence?

The preceding observations suggest there may exist a property of turbulence that induces it to transition to a more well-mixed state, is associated with Reynolds numbers in excess of $Re_{\min} \approx 10^4$, and appears to be rather independent of the details of the flow geometry. The following is a proposed ansatz to account for this behavior.

That this transition appears to be independent of the flow geometry indicates that the explanation should not be sought in the large-scale dynamics, or the development of distinct features and organized patterns in these flows. These are, typically, flow-geometry dependent. One is rather led to consider the physical significance of the various scales of turbulence and their Reynolds number scaling.

The 1941 Kolmogorov proposals hypothesize that the dynamics in the (inertial) range of scales λ that are unaffected by the outer scale δ , but are large compared to the inner, dissipation (Kolmogorov) scale,

$$\lambda_K \equiv \left(\frac{\nu^3}{\varepsilon} \right)^{1/4}, \quad (13)$$

i.e., for

$$\lambda_K \ll \lambda \ll \delta, \quad (14)$$

can be treated in a universal, self-similar fashion. In this range of scales, for example, the energy spectrum is predicted (and found) to exhibit a power-law behavior with a $-5/3$ exponent.⁶⁰

To refine the bounds in Eq. 14, we appreciate that independence from the dynamics of the outer scale, δ , requires that the scale λ be smaller than a scale that can be generated directly from the outer scale δ . Such a scale would be an outer laminar layer thickness, λ_L , that can be generated by a single δ -size sweep across the whole transverse extent of the turbulent region, for example. The size of this scale can be estimated in terms of the 99% thickness of a Blasius boundary layer, for example, that is growing over a spatial extent δ , *i.e.*,

$$\frac{\lambda_L}{\delta} \simeq 5.0 Re^{-1/2}. \quad (15)$$

It is a scale connected by viscosity to the outer scale, δ , of the flow. By virtue of its dependence on Reynolds number (*cf.* Eqs. 12 and 15), this scale, as noted by H. W. Liepmann in private conversation many years ago, is closely related to the Taylor microscale, λ_T .

At the other end of the spectrum, the requirement that the motions must be inviscid with respect to the inner dissipation scales dictates that the local scale λ must be large with respect to an inner viscous scale, λ_ν (*cf.* Fig. 10) that can be taken as proportional to the (defined) Kolmogorov dissipation scale, λ_K . This allows us to refine the inequality that bounds the inertial range of scales (Eq. 14) to the one below, *i.e.*,

$$\frac{\lambda_K}{\delta} < \frac{\lambda_\nu}{\delta} \ll \frac{\lambda}{\delta} \ll \frac{\lambda_L}{\delta} < 1, \quad (16)$$

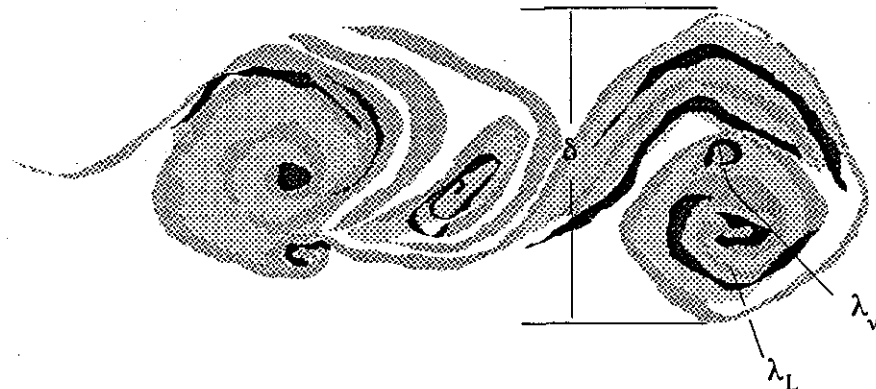


FIG. 10 Schematic of the outer scale, δ ; the Taylor scale, λ_T ; and the viscous scale, λ_ν , in a sheared turbulent region.

as a necessary condition for fully-developed flow.

To translate this inequality to a relation for the Reynolds number, we need the Reynolds number dependence of the ratio of the various scales to the outer scale δ . We can rely on Eq. 15 for the estimate of the outer laminar-layer thickness, λ_L , suggested by Liepmann. Following on his suggestion, it is interesting to compare that to the Taylor scale for a turbulent jet, for example. For turbulence in the far field of a jet, the Taylor scale, λ_T , can be estimated from the Taylor Reynolds number on the jet axis (Eq. 12). This is approximately given by

$$Re_T \simeq 1.4 Re^{1/2}, \quad (17)$$

on the jet axis.^{20,21} Using the value of $u' \simeq 0.25 u_c$, on the axis of the turbulent jet, and $\delta(x) \simeq 0.4(x - x_0)$ for the local jet diameter, we obtain

$$\frac{\lambda_T}{\delta} \simeq 2.3 Re^{-1/2}, \quad (18)$$

which is a little smaller but close to the Liepmann laminar-layer thickness, λ_L (a prefactor of 2.3 for λ_T , vs. 5.0, for λ_L), especially considering that it is estimated from flow properties on the jet axis.

An appropriate inner viscous scale, λ_ν , can be estimated in terms of the wave-number k_ν , where the energy spectrum deviates from the $-5/3$ power-law behavior, or, $k_\nu \lambda_K \simeq 1/8$.^{61,62} This yields,⁶³

$$\lambda_\nu \approx \frac{2\pi}{k_\nu} \simeq 50 \lambda_K. \quad (19)$$

To estimate the Reynolds number and outer scale dependence of λ_ν , we can use the expression from Friehe *et al.*,^{20,64} for the energy-dissipation rate on the jet axis, in the far field, *i.e.*,

$$\varepsilon \simeq 48 \frac{u_0^3}{d_0} \left(\frac{d_0}{x - x_0} \right)^4, \quad (20)$$

where u_0 is the jet nozzle velocity, d_0 is the jet nozzle diameter, and x_0 is the virtual origin of the far field turbulent flow. Substituting in Eq. 13 we then have

$$\frac{\lambda_K}{\delta} \simeq 0.95 Re^{-3/4}, \quad (21)$$

and, therefore, for a turbulent jet,

$$\frac{\lambda_\nu}{\delta} \simeq 50 Re^{-3/4}. \quad (22)$$

Substituting for λ_L , λ_ν , and λ_K in Eq. 16, we obtain

$$Re^{-3/4} < \frac{\lambda_{\min}}{\delta} \approx 50 Re^{-3/4} \ll \frac{\lambda}{\delta} \ll \frac{\lambda_{\max}}{\delta} \approx 5.0 Re^{-1/2} < 1. \quad (23)$$

The range of intermediate inviscid scales, *i.e.*, scales smaller than λ_L but larger than λ_ν , can be seen to grow rather slowly with Reynolds number. Specifically, the ratio

$$\mathcal{N} = \frac{\lambda_{\max}}{\lambda_{\min}}, \quad (24a)$$

which measures the extent of the uncoupled range of spatial scales, *i.e.*, the number of viscous scales within a Taylor scale, is given by

$$\mathcal{N} \approx 0.1 Re^{1/4}, \quad (24b)$$

where the (approximate) factor of 0.1 was estimated for a turbulent jet. This is indicated schematically in Fig. 11. In other flows, we can expect the uncoupled range of scales to exhibit the same Reynolds number dependence (Eqs. 24a,b), with, possibly, a different prefactor, however.

On the basis of these observations, it can be argued that a necessary condition for fully-developed turbulence and the 1941 Kolmogorov similarity ideas to apply is the existence of a range of scales that are uncoupled from the large scales, on the one hand, and are free from the effects of viscosity, on the other. Considering that we must have

$$\frac{\lambda_L}{\lambda_\nu} \simeq \frac{\lambda_{\max}}{\lambda_{\min}} = \mathcal{N} > 1, \quad (24c)$$

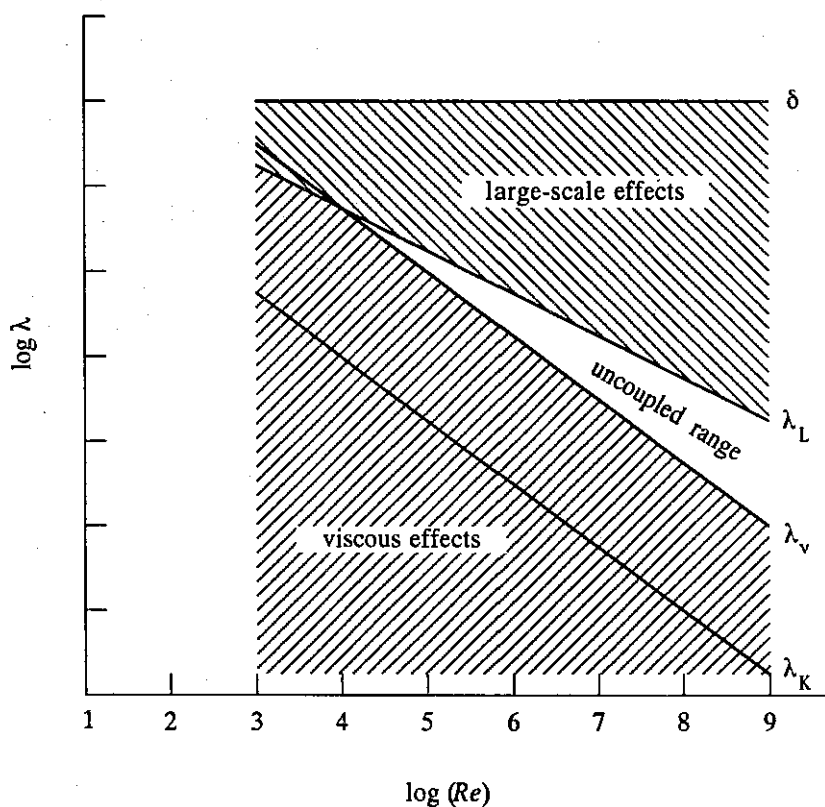


FIG. 11 Reynolds number dependence of spatial scales for a turbulent jet.

with some margin, we see that the existence of such a range of scales requires a minimum Reynolds number of the order of 10^4 (Eq. 24b); a value in accord with the minimum Reynolds number identified for transition to fully-developed, well-mixed turbulent flows.

Jimenez *et al.* performed measurements of velocity fluctuations in a two-dimensional shear layer and found a power-law regime in the energy spectrum, with an exponent close to $-5/3$, developing in the neighborhood of the mixing transition.⁶⁵ Subsequent investigations of the mixing transition by Huang and Ho also associated the development of a $-5/3$ spectral regime with the mixing transition, correlating it, however, with the number of pairings rather than with local values of the Reynolds number.⁶⁶ Nevertheless, in both these investigations, the Reynolds number in the vicinity of the mixing transition and the development of the $-5/3$ spectrum regime was found to be in the range of $3 \times 10^3 < Re(x) < 10^4$, in accord with the range documented in Fig. 2. To the extent that the appearance of a $-5/3$ spectral regime marks the development of an inertial range of scales and the applicability of the

1941 Kolmogorov ideas, these experiments lend further credence to the ansatz.

6. Conclusions

The preceding discussion of the experimental evidence and the theoretical ansatz supports the notion that fully-developed turbulence requires a minimum Reynolds number of the order of 10^4 to be sustained. This value must be viewed as a necessary, but not sufficient, condition for the flow to be fully-developed. Presently available evidence suggests that both the fact that the phenomenon occurs and the range of values of the Reynolds number where it occurs are universal, *i.e.*, independent of the flow geometry.

On the other hand, how sharp this transition is *does* appear to depend on the details of the flow. In particular, it is remarkably sharp, as a function of Reynolds number, in the (Couette-Taylor) flow between concentric rotating cylinders. It is less well-defined for a shear layer and, among the flows considered, the least well-defined for turbulent jets. Perhaps an explanation for this variation lies in the definition of the Reynolds number itself (Eq. 1) and the manner in which the various factors that enter are specified for each flow. In the case of the Couette-Taylor flow, for example, both the velocity $U_{CT} = \Omega a$ and the spatial scale $\delta_{CT} = b - a$, where Ω is the differential rotation rate, with a and b the inner and outer cylinder radii, are well-defined by the flow-boundary conditions.⁵⁹

In the case of a zero streamwise pressure-gradient shear layer, the velocity $U_{sl} = \Delta U = U_1 - U_2$ is a constant, reasonably well specified by the flow boundary conditions at a particular station. The length scale $\delta_{sl} = \delta_{sl}(x) = \langle \delta(x, t) \rangle_t$, however, must be regarded as a stochastic variable in a given flow with a relatively large variance. The Reynolds number for the shear layer is then the product of a well-defined variable and a less well-defined, stochastic variable.

In the case of a turbulent jet, both the local velocity $U_j = U_j(x) = \langle u_c(x, t) \rangle_t$ and the length scale $\delta_j = \delta_j(x) = \langle \delta_j(x, t) \rangle_t$, or $\delta_j(x) = \langle R(x, t) \rangle_t$, the local jet radius, must be regarded as stochastic flow variables, each with its own large variance. The Reynolds number for the jet is then the product of two stochastic

variables and, as a consequence, its local, instantaneous value is the least well-defined of the three.

Viewing the Reynolds number itself as a stochastic variable, it would appear that the hierarchy of the sharpness of the transition to the fully-developed turbulent state is correlated with the sharpness with which the flow and the boundary conditions allow the values of the local Reynolds number to be specified to the dynamics.

A related issue also arises as a consequence of the definition of the local Reynolds number. As noted in the discussion of Eqs. 1 and 2, the Reynolds number for a shear layer increases with the downstream coordinate, whereas the Reynolds number for a jet is a constant of the flow. As a consequence, a shear layer may possess regions with local Reynolds numbers below the minimum and transition to fully-developed turbulence, *within the spatial extent of the same flow*, if its stream-wise extent is large enough. A turbulent jet, on the other hand, is either fully developed over its whole extent, or is not. This is also relevant to the description and dynamics in other flows.

As regards fully-developed turbulent flow, the presently available evidence does not support the notion of Reynolds-number-independent mixing dynamics, at least in the case of gas-phase shear layers for which the investigations span a large enough range. In the case of gas-phase turbulent jets, presently available evidence admits a flame length stoichiometric coefficient A (*cf.* Eq. 3) tending to a Reynolds-number-independent behavior (*cf.* Fig. 7). We appreciate, however, that the range of Reynolds numbers spanned by experiments to date may not be large enough to provide us with a definitive statement, at least as evidenced by the range required in the case of shear layers (*cf.* Figs. 8). Secondly, the flame-length virtual origin, B (Eq. 3), possesses a maximum in the neighborhood of the transition Reynolds number of $Re \approx 2 \times 10^4$ and does not appear to attain a Reynolds-number-independent behavior in the same range of Reynolds numbers.²³ We should also recall that the torque in Couette-Taylor flow does not attain a Reynolds-number-independent behavior to the highest values of the Reynolds number investigated.⁵⁹ Neither, of course, does the skin-friction coefficient in a turbulent boundary layer over a smooth

flat plate.

In comparing shear-layer with turbulent-jet mixing behavior, the more important conclusion may be that they appear to respond in the opposite way to Schmidt number effects, *i.e.*, gas- *vs.* liquid-phase behavior. Specifically, it is high-Schmidt number (liquid-phase) shear layers that exhibit a low Reynolds-number dependence in chemical product formation, if any (*cf.* Fig. 8b). In contrast, it is gas-phase turbulent jets that exhibit an almost Reynolds-number-independent normalized variance of the jet-fluid concentration on the jet axis, with a strong Reynolds-number dependence found in liquid-phase jets, in the same Reynolds-number range (*cf.* Fig. 4).

To summarize, recent data on turbulent mixing, as well as evidence garnered in other contexts, support the notion that fully-developed turbulent flow requires a minimum Reynolds number of 10^4 , or a Taylor Reynolds number of $Re_T \approx 10^2$, to be sustained. Conversely, turbulent flow below this Reynolds number cannot be regarded as fully-developed and can be expected to be qualitatively different.

The manifestation of the transition to this state may depend on the particular flow geometry, *e.g.*, the appearance of streamwise vortices and three-dimensionality in shear layers. Nevertheless, the fact that such a transition occurs, as well as the approximate Reynolds number where it is expected, appears to be a universal property of turbulence. It is observed in a wide variety of flows and turbulent flow phenomena.

In contrast, studies of mixing in fully-developed turbulent jets and shear layers suggest that we cannot hope for a universal description of turbulent mixing. The dimensionless parameters that scale the relative importance of the molecular diffusivity coefficients, such as viscosity and species diffusivity, must not only enter in this description, but are likely to do so in a non-universal way.

It is interesting that transition to turbulence, at intermediate values of the Reynolds number, appears to be universal, whereas mixing in fully-developed turbulence, at high Reynolds numbers, does not.

7. Acknowledgements

The work described here is part of a larger program at Caltech to study mixing and chemically reacting turbulent flows and the result of the efforts, collaboration, and discussions of many people over the years. In the context of the material presented in this paper, I would specifically like to acknowledge the work and discussions with Paul L. Miller, on turbulent jet mixing, and Chris L. Bond, who recalculated many of the data points in Figs. 8 from the original measurements. This work was supported by the Air Force Office of Scientific Research, Grant Nos. 88-0155, 90-0304, and F49620-92-J-0290, and the Gas Research Institute Contract No. 5087-260-1467.

References

- ¹ Brown, G. L., and Roshko, A., "On Density Effects and Large Structure in Turbulent Mixing Layers," *J. Fluid Mech.* **64**, 775-816 (1974).
- ² Eckart, C., "An Analysis of the Stirring and Mixing Processes in Incompressible Fluids," *JMR VII*, 265-275 (1948).
- ³ Dimotakis, P. E., "Two-Dimensional Shear-Layer Entrainment," *AIAA J.* **24**, 1791-1796 (1986).
- ⁴ Aref, H., "Stirring by chaotic advection," *J. Fluid Mech.* **143**, 1-21 (1984).
- ⁵ Ottino, J. M., *The kinematics of mixing: stretching, chaos, and transport* (Cambridge University Press, 1989).
- ⁶ Rom-Kedar, V., Leonard, A., and Wiggins, S., "An analytical study of transport, mixing and chaos in an unsteady vortical flow," *J. Fluid Mech.* **214**, 347-394 (1990).
- ⁷ Ottino, J. M., "Mixing, Chaotic Advection and Turbulence," *Ann. Rev. Fluid Mech.* **22**, 207-253 (1990).
- ⁸ Kuznetsov, V. R., and Sabel'nikov, V. A., *Turbulence and Combustion* (Hemisphere Publishing, New York, 1990).

- ⁹ Konrad, J. H., *An Experimental Investigation of Mixing in Two-Dimensional Turbulent Shear Flows with Applications to Diffusion-Limited Chemical Reactions*, Ph.D. thesis, California Institute of Technology (1976).
- ¹⁰ Brown, G. L., and Rebollo, M. R., "A Small, Fast-Response Probe to Measure Composition of a Binary Gas Mixture," *AIAA J.* **10**, 649-652 (1972).
- ¹¹ Breidenthal, R. E., "Structure in Turbulent Mixing Layers and Wakes Using a Chemical Reaction," *J. Fluid Mech.* **109**, 1-24 (1981).
- ¹² Koochesfahani, M. M., and Dimotakis, P. E., "Mixing and chemical reactions in a turbulent liquid mixing layer," *J. Fluid Mech.* **170**, 83-112 (1986).
- ¹³ Masutani, S. M., and Bowman, C. T., "The structure of a chemically reacting plane mixing layer," *J. Fluid Mech.* **172**, 93-126 (1986).
- ¹⁴ Bernal, L. P., Breidenthal, R. E., Brown, G. L., Konrad, J. H., and Roshko, A., "On the Development of Three-Dimensional Small Scales in Turbulent Mixing Layers," *2nd Int. Symposium on Turb. Shear Flows* (Springer-Verlag, New York, 1980), 305-313 (1979).
- ¹⁵ Bernal, L. P., and Roshko, A., "Streamwise vortex structure in plane mixing layers," *J. Fluid Mech.* **170**, 499-525 (1986).
- ¹⁶ Roshko, A., "The mixing transition in free shear flows," *The Global Geometry of Turbulence* (Impact of nonlinear dynamics), NATO Advance Research Workshop, 8-14 July 1990, Rota (Cádiz), Spain (1990).
- ¹⁷ Moser, R. D., and Rogers, M. M., "Mixing transition and the cascade to small scales in a plane mixing layer," *Phys. Fluids A* **3**, 1128-1134 (1991).
- ¹⁸ Dimotakis, P. E., Miake-Lye, R. C., and Papantoniou, D. A., "Structure and Dynamics of Round Turbulent Jets," *Phys. Fluids* **26**, 3185-3192 (1983).
- ¹⁹ Seitzman, J., Üngüt, A., Paul, P., and Hanson, R., "Imaging and Characterization of OH Structures in a Turbulent Nonpremixed Flame," *23rd Symposium (International) on Combustion/The Combustion Institute*, 637-644 (1990).
- ²⁰ Dowling, D. R., and Dimotakis, P. E., "Similarity of the concentration field of gas-phase turbulent jets," *J. Fluid Mech.* **218**, 109-141 (1990).

- 21 Miller, P. L., and Dimotakis, P. E., "Reynolds number dependence of scalar fluctuations in a high Schmidt number turbulent jet," *Phys. Fluids A* **3**, 1156–1163 (1991).
- 22 Miller, P. L., *Mixing in High Schmidt Number Turbulent Jets*, Ph.D. thesis, California Institute of Technology (1991).
- 23 Gilbrech, R. J., *An Experimental Investigation of Chemically-Reacting, Gas-Phase Turbulent Jets*, Ph.D. thesis, California Institute of Technology (1991).
- 24 Gilbrech, R. J., and Dimotakis, P. E., "Product Formation in Chemically-Reacting Turbulent Jets," *AIAA 30th Aerospace Sciences Meeting*, Paper 92-0581 (1992).
- 25 Hottel, H. C., "Burning in Laminar and Turbulent Fuel Jets," 4th Symposium (International) on Combustion (Williams and Wilkins, Baltimore, 1953), 97–113 (1952).
- 26 Broadwell, J. E., "A Model of Turbulent Diffusion Flames and Nitric Oxide Generation. Part I," TRW Document No. 38515-6001-UT-00, EERC Final Report, PO No. 18889 (1982).
- 27 Dahm, W. J. A., and Dimotakis, P. E., "Measurements of Entrainment and Mixing in Turbulent Jets," *AIAA J.* **25**, 1216–1223 (1987).
- 28 Bilger, R. W., "Turbulent Flows with Nonpremixed Reactants," *Turbulent Reacting Flows* (Eds. P. A. Libby, F. A. Williams, *Topics in Applied Physics* **44**, Springer-Verlag, New York), 65–113 (1980).
- 29 Kuo, K. K., *Principles of Combustion* (John Wiley, New York, 1986).
- 30 Dimotakis, P. E., "Turbulent Free Shear Layer Mixing and Combustion," *High Speed Flight Propulsion Systems*, in *Progress in Astronautics and Aeronautics* **137**, Ch. 5, 265–340 (1991).
- 31 Namazian, M., and Kelly, J. T., "Near-Field Instantaneous Flame and Fuel Concentration Structures," Twenty-Second Symposium (International) on Combustion/The Combustion Institute, 627–634 (1988).
- 32 Dahm, W. J. A., Dimotakis, P. E., and Broadwell, J. E., "Non-premixed turbulent jet flames," *AIAA 22nd Aerospace Sciences Meeting*, Paper 84-0369 (1984).

- ³³ Weddell, D., *Turbulent Mixing in Gas Flames*, Ph.D. thesis, Massachusetts Institute of Technology (1941).
- ³⁴ Dowling, D. R., *Mixing in Gas Phase Turbulent Jets*, Ph.D. thesis, California Institute of Technology (1988).
- ³⁵ Mungal, M. G., and Dimotakis, P. E., "Mixing and combustion with low heat release in a turbulent mixing layer," *J. Fluid Mech.* **148**, 349-382 (1984).
- ³⁶ Mungal, M. G., Hermanson, J. C., and Dimotakis, P. E., "Reynolds Number Effects on Mixing and Combustion in a Reacting Shear Layer," *AIAA J.* **23**, 1418-1423 (1985).
- ³⁷ Frieler, C. E., *Mixing and Reaction in the Subsonic 2-D Turbulent Free Shear Layer*, Ph.D. thesis, California Institute of Technology (1992).
- ³⁸ Hall, J. L., Dimotakis, P. E., and Rosemann, H., "Some measurements of molecular mixing in compressible turbulent mixing layers," *AIAA 22nd Fluid Dynamics, Plasma Dynamics and Lasers Conference*, Paper 91-1719 (1991).
- ³⁹ Broadwell, J. E., and Breidenthal, R. E., "A simple model of mixing and chemical reaction in a turbulent shear layer," *J. Fluid Mech.* **125**, 397-410 (1982).
- ⁴⁰ Dimotakis, P. E., "Turbulent shear layer mixing with fast chemical reactions," *US-France Workshop on Turbulent Reactive Flows* (Springer-Verlag, New York, 1989), 417-485 (1987).
- ⁴¹ Hall, J. L., *An Experimental Investigation of Structure, Mixing and Combustion in Compressible Turbulent Shear Layers*, Ph.D. thesis, California Institute of Technology (1991).
- ⁴² Dimotakis, P. E., "On the convection velocity of turbulent structures in supersonic shear layers," *AIAA 22nd Fluid Dynamics, Plasma Dynamics and Lasers Conference*, Paper 91-1724 (1991).
- ⁴³ Miller, P. L., and Dimotakis, P. E., "Measurements of scalar power spectra in high Schmidt number turbulent jets," *GALCIT Report FM92-3* (1992).
- ⁴⁴ Broadwell, J. E., and Mungal, M. G., "Large-scale structures and molecular mixing," *Phys. Fluids A* **3**(5), Pt. 2, 1193-1206 (1991).

- ⁴⁵ Wygnanski, I., and Champagne, F. H., "On transition in a pipe. Part I: The Origin of Puffs and Slugs and the Flow in a Turbulent Slug," *J. Fluid Mech.* **59**, 281-335 (1973).
- ⁴⁶ Coles, D., "The law of the wake in the turbulent boundary layer," *J. Fluid Mech.* **1**, 191-226 (1956).
- ⁴⁷ A turbulent boundary layer is characterized by three transverse scales, whose separation increases with increasing Reynolds number: the inner, viscous sub-layer; the intermediate, log-law layer; and the outer, wake region layer. The integral displacement thickness was used here as the single scale in the definition of Reynolds number.
- ⁴⁸ Coles, D., "The Young Person's Guide to the Data," Proc. AFOSR-IFP-Stanford Conference *Computation of Turbulent Boundary Layers, II* (D. Coles & Hirst, eds.), 1-45 (1968).
- ⁴⁹ Collins, D. J., Coles, D. E., and Hicks, J. W., "Measurements in the Turbulent Boundary Layer at Constant Pressure in Subsonic and Supersonic Flow. Part I. Mean Flow," AEDC-TR-78-21 (1978).
- ⁵⁰ Liepmann, D., and Gharib, M., "The role of streamwise vorticity in the near-field entrainment of round jets," *J. Fluid Mech.* **245**, 643-668 (1992).
- ⁵¹ Hammer, J. A., *Lifted Turbulent Jet Flames*, Ph.D. thesis, California Institute of Technology (1993).
- ⁵² Roshko, A., "Perspectives on bluff body aerodynamics," 2nd *Int. Coll. on Bluff Body Aerodynamics*, Melbourne, Australia (1992).
- ⁵³ Sreenivasan, K. R., "On the scaling of the turbulent energy dissipation rate," *Phys. Fluids* **27**, 1048-1050 (1984).
- ⁵⁴ Jimenez, J., Wray, A. A., Saffman, P. G., and Rogallo, R. S., "The structure of intense vorticity inhomogeneous isotropic turbulence," *Studying Turbulence Using Numerical Simulation Databases — IV*, Proceedings, 1992 Summer Program (Center for Turbulence Research, NASA Ames & Stanford U.), 21-45 (1992).
- ⁵⁵ J. Jimenez has noted (private communication) an alternate possible explanation for the Reynolds number behavior of the scaled dissipation rate, α (Eq. 11), in

this flow, as well as in grid turbulence.⁵³ He notes the decrease in the energy spectrum wavenumber span, and, therefore, in its integral, u'^2 , with decreasing Reynolds number. In particular, he suggests that scaling the dissipation rate, ε , with an outer flow speed, instead of the velocity rms, u' , could account for the observed Reynolds number behavior of this quantity.

- ⁵⁶ Heslot, F., Castaign, B., and Libchaber, A., "Transitions to turbulence in helium gas," *Phys. Rev. A* **36**, 5870–5873 (1987).
- ⁵⁷ Castaign, B., Gunaratne, G., Heslot, F., Kadanoff, L., Libchaber, L., Thomae, S., Wu, X.-Z., Zaleski, S., and Zanetti, G., "Scaling of hard thermal turbulence in Rayleigh-Bénard convection," *J. Fluid Mech.* **204**, 1–30 (1989).
- ⁵⁸ Lathrop, D. P., Fineberg, J., and Swinney, H. L., "Turbulent flow between Concentric Rotating Cylinders at Large Reynolds Number," *Phys. Rev. Lett.* **68**, 1515–1518 (1992).
- ⁵⁹ Lathrop, D. P., Fineberg, J., and Swinney, H. L., "Transition to shear-driven turbulence in Couette-Taylor flow," *Phys. Rev. A* **46**, 6390–6405 (1992).
- ⁶⁰ Monin, A. S., and Yaglom, A. M., *Statistical Fluid Mechanics: Mechanics of Turbulence II* (Ed. J. Lumley, MIT Press, Cambridge, MA, 1975).
- ⁶¹ Chapman, D. R., "Computational Aerodynamics Development and Outlook," *AIAA J.* **17**, 1293–1313 (1979).
- ⁶² Saddoughi, S. G., "Local isotropy in high Reynolds number turbulent shear flows," *Annual Research Briefs – 1992* (Center for Turbulence Research, NASA Ames & Stanford U., Jan. 1993), 237–262 (1992).
- ⁶³ This calculation is discussed in Ref. 21, where, for the purposes of estimating diffusion-layer thicknesses (transition from high to low values of the diffusing scalar), half this estimate, *i.e.*, $\lambda_\nu \approx \pi/k_\nu \simeq 25 \lambda_K$, was used.
- ⁶⁴ Friehe, C. A., Van Atta, C. W., and Gibson, C. H., "Jet turbulence: Dissipation rate measurements and correlations," *AGARD Turbulent Shear Flows CP-93*, 18.1–7 (1971).
- ⁶⁵ Jimenez, J., Martinez-Val, R., and Rebollo, M., "On the origin and evolution of three-dimensional effects in the mixing layer," *Internal Rept. DA-ERO-70-G-079*, Univ. Politec., Madrid, Spain (1979).

- ⁶⁶ Huang, L.-S., and Ho, C.-M., "Small-scale transition in a plane mixing layer," *J. Fluid Mech.* **210**, 475–500 (1990).

APPENDIX C

LAPPAS, T., LEONARD, A. & DIMOTAKIS, P. E. 1993 "An Adaptive Lagrangian Method for Computing 1-D Reacting and Non-Reacting Flows," *J. Comp. Phys.* **104**(2), 361–376.

An Adaptive Lagrangian Method for Computing 1D Reacting and Non-reacting Flows

TASSO LAPPAS, ANTHONY LEONARD, AND PAUL E. DIMOTAKIS

Graduate Aeronautical Laboratories, California Institute of Technology, Pasadena, California 91125

Received April 5, 1991; revised April 20, 1992

A method for computing one-dimensional unsteady compressible flows, with and without chemical reactions is presented. This work has focused on the accurate computation of the discontinuous waves that arise in such flows. The main feature of the method is the use of an adaptive Lagrangian grid. This allows the computation of discontinuous waves and their interactions with the accuracy of front-tracking algorithms. This is done without the use of additional grid points representing shocks, in contrast to conventional front-tracking schemes. The Lagrangian character of the present scheme also allows contact discontinuities to be captured easily. The algorithm avoids interpolation across discontinuities in a natural and efficient way. The method has been used on a variety of reacting and non-reacting flows in order to test its ability to compute accurately and in a robust way complicated wave interactions. © 1993 Academic Press, Inc.

1. INTRODUCTION

Several methods for computing unsteady inviscid compressible flows have appeared in the literature in recent years. The emphasis has been on the ability of these numerical schemes to compute accurately discontinuous waves which develop and their interactions.

High-resolution shock-capturing methods for hyperbolic conservation laws is one category of such methods which have been used successfully in recent years. A basic feature of these methods is that the conservative formulation is used which allows for shocks and their interactions to be captured automatically without special effort. This is characteristic of all older shock-capturing methods, such as the Lax-Wendroff scheme [8], the MacCormack scheme [10], the original Godunov scheme [5]. In all such methods, discontinuous waves of the solution are represented as steep fronts, i.e., smeared over a finite number of computational cells. A second and more important feature of recent high-resolution schemes is the special effort which is made to achieve higher order spatial and temporal accuracy so as to represent discontinuous waves of the solution as accurately as possible, i.e., to reduce the smearing effect

which is typical of all shock-capturing methods. Such schemes are the TVD schemes [6, 7], the various MUSCL-type schemes [15], the PPM scheme [3] (piecewise parabolic method), etc. A comparative study of some of these schemes for real gases is given in a review article by Montagné *et al.* [11]. The basic high-resolution shock-capturing methods have been developed for nonlinear scalar hyperbolic conservation laws. It is for this case that there exists a sound mathematical theory. For nonlinear hyperbolic systems of equations in one space variable the theory is not as clear and the numerical methods used for these systems apply formally the same techniques as in the scalar case, but with the additional use of exact or approximate Riemann solvers. A classical Riemann problem is solved locally at each computational cell boundary in order to compute the various flux terms required. This is the essential ingredient of the original Godunov scheme and it is present in most successful high-resolution schemes. The various flux-vector splitting techniques [14, 16] have essentially incorporated in them an approximate Riemann solver. Finally, their extension to more than one space dimension is usually done by treating each spatial dimension separately.

Another category of numerical schemes that have been used is that of the shock-fitting or front-tracking methods. Although they have not been used as extensively as the shock-capturing methods, they have been quite successful in one-dimensional problems. A good review of these methods, as well as of many shock capturing methods, is given by Moretti [12]. These schemes are typically based on a non-conservative formulation and an effort is made to detect and identify the various discontinuous waves and compute their interactions explicitly. This is usually accomplished by introducing additional computational elements representing such waves and using the Rankine-Hugoniot jump conditions. This technique leads to complex programming logic. Identifying the waves and computing their interactions accurately is crucial for obtaining a meaningful and stable solution. For flows with complicated wave inter-

actions such schemes may not be as robust as the shock-capturing schemes, even in one space dimension.

The research presented in this paper is part of a greater effort which aims to combine the characteristics of the above two categories of numerical schemes and to develop a method which will share the advantages and eliminate most of the disadvantages of both. This has been accomplished in the case of one-dimensional flow by the scheme presented in this paper. The increased accuracy which is provided in the computation of complicated wave interactions and its robustness have made this scheme especially valuable for the computation of reacting gas flows, where detonation waves are present.

The scheme is based on a conservative shock-capturing Godunov-type scheme, very much like van Leer's MUSCL scheme [15]. The new feature, introduced here, is an adaptive Lagrangian grid which increases the accuracy with which discontinuous waves and their interactions are computed. Without introducing additional computational elements, i.e., refining the grid, or special computational elements to represent these waves, the shocks and contact discontinuities are computed as true discontinuities, without the smearing effect typical of shock-capturing methods. This makes the scheme different from adaptive mesh refinement schemes (e.g., see Berger and Olinger [2]), which smear discontinuities, although on a much finer local grid. The basic conservative shock-capturing capabilities of the scheme are not diminished. The scheme is endowed with the capability to track various fronts and, thus, the shock-capturing and the front-tracking ideas are combined properly. It is important to note that the adaptive grid strategy, to a certain degree, is independent of the particular solver. Any Godunov-type scheme may be used. The Riemann solver is the link that provides the information about local wave interactions needed for the adaptive procedure.

It was deemed interesting to try this scheme on one-dimensional flows of reacting gases in light of the increased accuracy and robustness with which detonation waves and their interactions could be computed. The interest in such flows is evident by the number of papers appearing in the literature. For example, numerical calculations, with increased accuracy, of the one-dimensional instability of plane detonation waves may be of great interest in confirming existing theories which are based on linear stability analysis (e.g., see Lee and Stewart [9]). The present scheme is able to reduce the error caused by the numerical smearing of the leading shock of the detonation wave. This error may be very important in the development of detonation instability.

The computer code developed is also able to compute one-dimensional cylindrically and spherically symmetric flows, as well as plane flows with area change. It is thus possible to compute explosions and implosions and study

the effect of curvature on detonation wave speed and stability. Most of the results presented are basically validation runs and calculations demonstrating the abilities of the method and the potential use for specific one-dimensional problems of interest. All results shown are for a perfect gas. The difficulty of incorporating a general equation of state is the same as in most schemes and independent of the main feature of the present scheme, i.e., the adaptive Lagrangian grid strategy.

2. NUMERICAL METHOD

2.1. Mathematical Formulation

The inviscid flow of a reacting mixture of calorically perfect gases is considered. The assumption of a simplified reacting mixture is made, according to which there are two species present at any time, the reactant and the product. The reactant is converted to the product by a one-step irreversible exothermic chemical reaction. This assumption is made in order to compare with the many theoretical and numerical results which are available in the literature for this case. The chemical reaction rate is given by the standard Arrhenius law

$$\dot{z} = -KzT^\alpha \exp(-E/R_g T), \quad (1a)$$

where z is the mass fraction of unburnt gas, K is a positive constant, which essentially gives a time scale, E is the activation energy of the chemical reaction, R_g is the gas constant, T is the absolute temperature, and α is also a constant. The simplified Arrhenius model, where the reaction rate is a step function depending on the temperature, has also been used. For the simplified model the rate is given by

$$\dot{z} = -KzH(T - T_c), \quad (1b)$$

where

$$H(x) = \begin{cases} 1, & x > 0, \\ 0, & x \leq 0, \end{cases} \quad (2)$$

and T_c is a given critical temperature.

The problem under consideration is a special case of the general problem of solving numerically the nonlinear hyperbolic system of the form

$$\frac{\partial U}{\partial t} + \frac{\partial F(U)}{\partial x} = G(U), \quad (3)$$

where U is the appropriate solution vector. As usual, x denotes the Eulerian space variable. If the Lagrangian formulation is used, a system of exactly the same form is

obtained. The space variable x , then, is replaced by a Lagrangian space variable and the flux vector $F(U)$ is changed appropriately. For non-reacting flow, $G(U) = 0$. Most numerical methods use Eq. (3) as their starting point and, using a finite volume discretization, obtain the scheme of the following general form

$$U_j^{n+1} = U_j^n - \frac{\Delta t}{\Delta x} (\hat{F}_{j+1/2} - \hat{F}_{j-1/2}) + \Delta t \hat{G}_j, \quad (4)$$

giving the solution, in an average sense, in the j th cell at the time level $n + 1$. The numerical flux terms \hat{F} are computed at the boundaries of each cell. An important feature of every numerical method is the calculation of these flux terms in a way that guarantees stability and high-order accuracy.

A slightly different approach will be taken in deriving the present scheme. Eventually, it will be of the general form given in Eq. (4). It is useful to formulate the problem by writing the conservation laws in integral form for an arbitrary control volume $V(t)$, whose bounding surface $S(t)$ moves with a velocity \mathbf{u}_b (Reynolds' transport theorem). These equations will be applied to each computational volume of the discrete numerical scheme. This is done so that the conservation equations and their discrete counterparts are written in a way which is independent of the Eulerian or Lagrangian formulation that will be adopted eventually. Moreover, it is easier to see from these equations how the idea for the adaptive nature of the grid is motivated. The conservation equations in integral form are

$$\frac{d}{dt} \int_{V(t)} \rho dV + \int_{S(t)} \rho(\mathbf{u} - \mathbf{u}_b) \cdot d\mathbf{S} = 0, \quad (5)$$

$$\begin{aligned} \frac{d}{dt} \int_{V(t)} \rho \mathbf{u} dV + \int_{S(t)} \rho \mathbf{u}(\mathbf{u} - \mathbf{u}_b) \cdot d\mathbf{S} \\ + \int_{S(t)} p d\mathbf{S} = 0, \end{aligned} \quad (6)$$

$$\begin{aligned} \frac{d}{dt} \int_{V(t)} \rho e_t dV + \int_{S(t)} \rho e_t(\mathbf{u} - \mathbf{u}_b) \cdot d\mathbf{S} \\ + \int_{S(t)} p \mathbf{u} \cdot d\mathbf{S} = 0, \end{aligned} \quad (7)$$

$$\begin{aligned} \frac{d}{dt} \int_{V(t)} \rho z dV + \int_{S(t)} \rho z(\mathbf{u} - \mathbf{u}_b) \cdot d\mathbf{S} \\ - \int_{V(t)} \dot{z} \rho dV = 0. \end{aligned} \quad (8)$$

equations, e_t is the total specific energy, which includes the chemical energy, i.e.,

$$e_t = e + \frac{1}{2} u^2 + q_0 z, \quad (9)$$

where e is the specific internal energy, q_0 is the heat release of the chemical reaction, and $u = |\mathbf{u}|$ is the magnitude of the fluid velocity. The perfect gas assumption is also made, i.e.,

$$p = (\gamma - 1) \rho e. \quad (10)$$

Since the boundaries of the computational cells will be moving, it is useful to consider the flow map

$$\mathbf{x} = \mathbf{X}(\xi, t), \quad (11)$$

which gives the position of the fluid particle that was initially ($t = 0$) at the position ξ . Thus, ξ is convenient Lagrangian marker for the fluid particles in the flow. If the Lagrangian approach is taken, the local boundary velocity is equal to the local fluid velocity, i.e., $\mathbf{u}_b = \mathbf{u}$ in Eqs. (5)–(8).

2.2. Spatial and Temporal Discretization

Consider now the case of one-dimensional flow. A finite volume formulation is used, i.e., space is discretized by a set of computational cells as shown in Fig. 1. The conservation equations are now written for the j th cell of the computational grid

$$\frac{dm_j}{dt} + (\rho \Delta u_b)_{j+1/2} - (\rho \Delta u_b)_{j-1/2} = 0, \quad (12)$$

$$\begin{aligned} \frac{d}{dt} (m_j u_j) + (\rho u \Delta u_b)_{j+1/2} - (\rho u \Delta u_b)_{j-1/2} \\ + p_{j+1/2} - p_{j-1/2} = 0, \end{aligned} \quad (13)$$

$$\begin{aligned} \frac{d}{dt} (m_j e_j) + (\rho e_t \Delta u_b)_{j+1/2} - (\rho e_t \Delta u_b)_{j-1/2} \\ + (up)_{j+1/2} - (up)_{j-1/2} = 0, \end{aligned} \quad (14)$$

$$\begin{aligned} \frac{d}{dt} (m_j z_j) + (\rho z \Delta u_b)_{j+1/2} \\ - (\rho z \Delta u_b)_{j-1/2} - \dot{z}_j m_j = 0, \end{aligned} \quad (15)$$

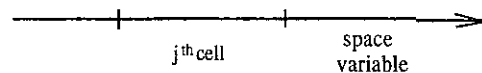


FIG. 1. Finite volume discretization in one space dimension. The space variable can be the Eulerian x or the Lagrangian ξ . The boundaries of the j th cell are denoted by the subscripts $j \pm \frac{1}{2}$.

These are written for an arbitrary control volume $V(t)$, whose bounding surface $S(t)$ has a velocity \mathbf{u}_b . In the above

where

$$\begin{aligned}
 \Delta u_b &\equiv u - u_b, \\
 m_j &\equiv \int_{x_{j-1/2}}^{x_{j+1/2}} \rho \, dx, \\
 m_j u_j &\equiv \int_{x_{j-1/2}}^{x_{j+1/2}} \rho u \, dx, \\
 m_j e_{ij} &\equiv \int_{x_{j-1/2}}^{x_{j+1/2}} \rho \left(e + \frac{1}{2} u^2 + q_0 z \right) dx, \\
 m_j z_j &\equiv \int_{x_{j-1/2}}^{x_{j+1/2}} \rho z \, dx.
 \end{aligned} \tag{16}$$

Average values of all quantities in the j th cell are denoted by the subscript j and values of various quantities at the two boundaries of the cell are denoted by the subscripts $j \pm \frac{1}{2}$. Note that average values are mass-averaged values. By defining

$$\begin{aligned}
 F_m &\equiv \rho \Delta u_b, \\
 F_u &\equiv \rho u \Delta u_b + p, \\
 F_e &\equiv \rho e_i \Delta u_b + \rho u, \\
 F_z &\equiv \rho z \Delta u_b,
 \end{aligned} \tag{17}$$

the equations of motion can be written in the more familiar form

$$\begin{aligned}
 \frac{dm_j}{dt} + (F_m)_{j+1/2} - (F_m)_{j-1/2} &= 0, \\
 \frac{d}{dt} (m_j u_j) + (F_u)_{j+1/2} - (F_u)_{j-1/2} &= 0, \\
 \frac{d}{dt} (m_j e_{ij}) + (F_e)_{j+1/2} - (F_e)_{j-1/2} &= 0, \\
 \frac{d}{dt} (m_j z_j) + (F_z)_{j+1/2} - (F_z)_{j-1/2} &= m_j \dot{z}_j.
 \end{aligned} \tag{18}$$

Note the extra degree of freedom provided in the flux terms by the, as of yet unspecified, term Δu_b . The motion of the cell boundaries is determined by

$$\frac{dx_{j \pm 1/2}}{dt} = (u_b)_{j \pm 1/2} \tag{19}$$

and the average density in each cell is given by

$$\rho_j = \frac{m_j}{x_{j+1/2} - x_{j-1/2}}. \tag{20}$$

The equation of state (10) provides the means for computing the average pressure in the j th cell,

$$p_j = (\gamma_j - 1) \rho_j \left(e_{ij} - q_0 z_j - \frac{1}{2} u_j^2 \right). \tag{21}$$

The exact integral conservation laws have been written for each computational cell. Equations (18) will now be integrated in time explicitly. The basis for the method is a conservative Godunov-type scheme similar to the MUSCL scheme introduced by van Leer [15]. The procedure followed in solving these equations is similar to that used in most methods, which are higher-order extensions of the original Godunov scheme. At every time instant, average values of the solution are known in each computational cell. Linear variations of the primitive variables, i.e., density ρ , pressure p , and velocity u , are assumed in each cell. A Riemann problem is then set up locally at each cell interface. The solution to this problem gives the velocity, pressure and density needed to compute the flux terms (17). The different feature in the present scheme is that the Lagrangian formulation is used instead of the Eulerian and that an adaptive grid is used.

So far, the fact that the Lagrangian formulation is being used, has not appeared explicitly in the description of the method. It is now that this choice is made and all quantities are considered as functions of time t and the Lagrangian space coordinate ξ . The interpolation procedure is carried out in ξ -space and, assuming linear variation, the generic quantity q varies as

$$q(\xi) = q_j + (q_\xi)_j (\xi - \xi_j), \tag{22}$$

in the j th cell, where q_j is the mass-averaged value in the cell, ξ_j is the center of the cell (in Lagrangian space), and $(q_\xi)_j$ is the slope of q in this cell, which is assumed to be constant. Note that discontinuities of these quantities are allowed at the cell interfaces, as shown in Fig. 2.

The slopes are chosen using the van Leer slope limiter [17], but the adaptive nature of the grid, which will be

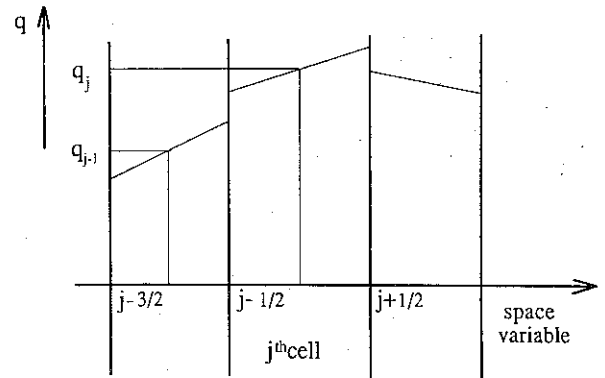


FIG. 2. Linear variation of the generic quantity q in the j th cell. In general, q is discontinuous at the cell interfaces.

described next, makes the choice of limiter less important than in the typical higher-order Godunov-type schemes. In fact, the adaptive grid allows more freedom in choosing the interpolation scheme, because additional information on the location of the various waves is always available at each time instant. The slope $(q_\xi)_j$ is computed, following van Leer [17], by

$$(q_\xi)_j = \text{ave}(q_\xi^-, q_\xi^+), \quad (23)$$

where

$$q_\xi^- = \frac{q_j - q_{j-1}}{\xi_j - \xi_{j-1}}, \quad q_\xi^+ = \frac{q_{j+1} - q_j}{\xi_{j+1} - \xi_j}, \quad (24)$$

$$\text{ave}(x, y) \equiv \frac{x+y}{2} \left[1 - \frac{(x-y)^2}{x^2 + y^2 + c^2} \right], \quad (25)$$

and c^2 is a small constant ($c^2 \ll 1$).

At each cell interface, two constant states q^- and q^+ are required to be used as the initial condition for the Riemann problem. There are many ways of doing this. One way is to specify for the $j + \frac{1}{2}$ interface

$$\begin{aligned} q_{j+1/2}^- &= q_j + (q_\xi)_j (\xi_{j+1/2} - \xi_j), \\ q_{j+1/2}^+ &= q_{j+1} + (q_\xi)_{j+1} (\xi_{j+1/2} - \xi_{j+1}), \end{aligned} \quad (26)$$

i.e., the values of q on either side of the interface, as given by Eq. (22). Using these states does not ensure second-order accuracy in time. The method used in the present scheme is shown in Fig. 3. The domain of dependence of $\xi = \xi_{j+1/2}$ over the time interval Δt is estimated by the characteristics at the time level t . In the Lagrangian formulation of the problem the characteristic speeds are given by

$$c_\pm = \pm \frac{\rho}{\rho_0} a, \quad (27)$$

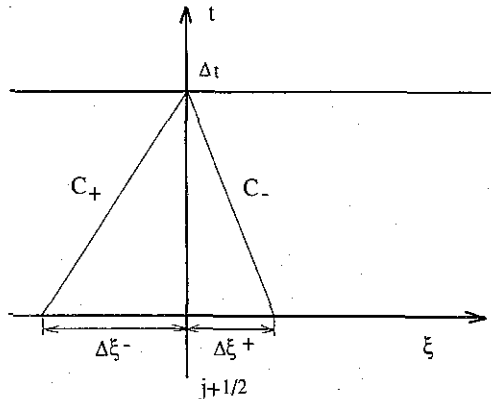


FIG. 3. The constant states q^\pm , which are to be used as the initial condition for the Riemann problem at the interface $j + \frac{1}{2}$, are obtained by averaging the linear interpolant over the domains of dependence $\Delta \xi^\pm$. These domains correspond to the full timestep Δt .

where ρ_0 is the initial density ($t=0$) and a is the speed of sound. The constant states q^\pm are then determined as the averages of Eq. (22) over the domains $\Delta \xi^\pm$; Fig. 3. These domains correspond to the full timestep Δt . This is equivalent to tracing the characteristics back from the time $t + \Delta t/2$ and using the linear profile (22). This ensures second-order accuracy in time.

The discrete scheme, giving the solution at the time level $n+1$ from the solution at the previous time level n , can now be written as

$$\begin{aligned} (m_j)^{n+1} &= (m_j)^n - \Delta t [(\hat{F}_m)_{j+1/2} - (\hat{F}_m)_{j-1/2}], \\ (m_j u_j)^{n+1} &= (m_j u_j)^n - \Delta t [(\hat{F}_u)_{j+1/2} - (\hat{F}_u)_{j-1/2}], \\ (m_j e_v)^{n+1} &= (m_j e_v)^n - \Delta t [(\hat{F}_e)_{j+1/2} - (\hat{F}_e)_{j-1/2}], \\ (m_j z_j)^{n+1} &= (m_j z_j)^n - \Delta t [(\hat{F}_z)_{j+1/2} - (\hat{F}_z)_{j-1/2}] \\ &\quad + \Delta t (m_j \dot{z}_j)^n, \end{aligned} \quad (28)$$

$$x_{j\pm 1/2}^{n+1} = x_{j\pm 1/2}^n + \Delta t (u_b)_{j\pm 1/2},$$

where the numerical fluxes \hat{F}_m , \hat{F}_u , \hat{F}_e , and \hat{F}_z are given by Eqs. (17), using the solution of the Riemann problem. The average boundary velocity u_b for each interface is still unspecified, but for the majority of interfaces $u_b = u$ and the last of Eqs. (28) is second-order accurate in time. The source term in the species equation is shown in Eqs. (28) as being evaluated at the time level n . It is better to integrate the source term in a "split" manner, i.e., integrate the first four equations in (28) without the source term and use this intermediate state to estimate the term $m_j \dot{z}_j$. This splitting has been implemented in the present scheme.

The stability requirement on the timestep is that of a MUSCL scheme in the Lagrangian formulation. No additional stability problems arise due to the adaptive grid strategy presented in the next section.

2.3. Adaptive Grid

The motivation for the adaptive grid comes from the definition of the flux terms, as given by Eqs. (17). The term Δu_b , or, equivalently, the velocity of the cell boundary u_b , is unspecified. The idea is to specify it at each cell interface, so that all important discontinuous waves coincide with cell boundaries, at every discrete time level. The solution of the Riemann problem at a given interface provides all the information needed to identify all the important waves emanating from this interface, as well as their strengths and speeds. This information is enough to specify Δu_b . Since all important waves coincide with cell boundaries, it is guaranteed that, at subsequent time instants, the evolution of these waves will be determined properly by the solution of the

local Riemann problems. In the numerical experiments carried out, shock waves computed by the local Riemann solvers were considered important enough to track if the shock Mach number was greater than 1.01 and contact discontinuities were considered important if the ratio of the densities on either side was greater than 1.05. These parameters are quite conservative. One may want to track only the very strong shock waves in the flow.

The grid is, basically, Lagrangian, i.e., most cell boundaries move with the local fluid velocity and, hence $\Delta u_b = 0$. It is easy to see that the same ideas on the adaptivity of the grid can be used on a grid that is primarily Eulerian. The same equations can be applied directly.

An example of this adaptive procedure is shown in Fig. 4. A strong shock wave moving to the right is computed by the Riemann solver at the interface $i - \frac{1}{2}$ at time t . The decision is made to assign a velocity to the adjacent cell boundary $i + \frac{1}{2}$, so that at time $t + \Delta t$ the shock coincides with the interface $i + \frac{1}{2}$. Another possibility would be to have the interface $i - \frac{1}{2}$ move with the shock. The decision is made depending on which interface would be required to move a shorter distance in Lagrangian space. The shock speeds are assumed constant over the time interval Δt . It is obvious that the local expansion waves can be tracked in the same way. This was not implemented in the present scheme, simply to reduce the complexity of the programming.

It is evident from this example that a relation between the velocities in real space and the velocities in Lagrangian space is needed to update the Lagrangian grid. Consider the motion of a cell boundary given by the trajectory $x = x_b(t)$. This boundary is moving with a velocity $u_b = \dot{x}_b(t)$, which, in general, is different from that of the fluid u . This motion corresponds to a motion in ξ -space given by the trajectory $\xi = \xi_b(t)$ with velocity $v_b = \dot{\xi}_b(t)$. The relation between the two velocities is found with the use of the flow map

$$x = X(\xi, t), \tag{29}$$

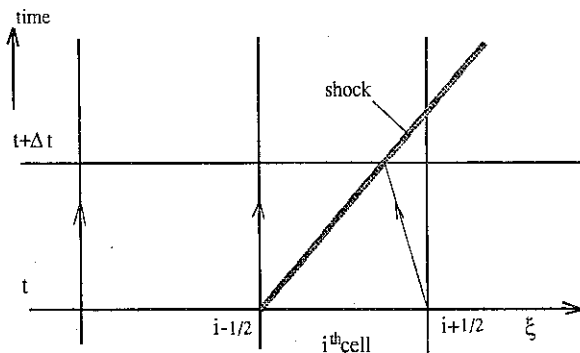


FIG. 4. The appropriate velocity is assigned to the cell interface $i + \frac{1}{2}$ in order to intercept the shock at the subsequent discrete time level.

which is essentially Eq. (11) written here for one-dimensional flow. The cell boundary motion is given by

$$x_b(t) = X(\xi_b(t), t) \tag{30}$$

and, hence,

$$u_b = \left(\frac{\partial X}{\partial t} \right)_{\xi} + \dot{\xi}_b(t) \left(\frac{\partial X}{\partial \xi} \right)_{t} \tag{31a}$$

or

$$u_b = u + v_b \left(\frac{\partial X}{\partial \xi} \right)_{t} \tag{31b}$$

The derivative of the flow map is numerically approximated and assumed constant in each cell, i.e.,

$$\left(\frac{\partial X}{\partial \xi} \right)_j \approx \frac{x_{j+1/2} - x_{j-1/2}}{\xi_{j+1/2} - \xi_{j-1/2}} \tag{32}$$

The velocities of the various waves, which are computed by the Riemann problems, can be translated into velocities in ξ -space by using Eq. (31b). The Lagrangian position of each interface is updated by

$$\xi_{j \pm 1/2}^{n+1} = \xi_{j \pm 1/2}^n + \Delta t (v_b)_{j \pm 1/2} \tag{33}$$

The solution to the Riemann problem at each interface provides sufficient information for the adaptive strategy. Using the exact Riemann solver at every interface is very costly. To reduce the cost, various criteria were found to identify the cell interfaces where a strong discontinuous wave is suspected to be present, before solving the Riemann problem. These interfaces are flagged as critical interfaces. The ratio $\Delta \xi^- / \Delta \xi^+$ has proven useful in detecting developing shocks in the flow. Where the flow is smooth, without steep gradients, the above ratio is

$$\frac{\Delta \xi^-}{\Delta \xi^+} \approx 1. \tag{34}$$

The regions, where this ratio deviates from unity by more than 10%, are considered critical regions. The full nonlinear Riemann solver is used only in these regions. Everywhere else the simple acoustic approximation to the Riemann problem solution is used. It was found in all the numerical experiments performed that, in addition to the above criterion, finding local extrema of the slopes in pressure, density, and velocity was very useful in determining these regions. Other criteria may also be used. It is important that the criteria be conservative enough, so that no critical regions are missed, but they are not crucial in detecting

discontinuous waves. The detection of important discontinuous waves is ultimately done by examining the solutions to the local Riemann problems.

No more than two adjacent critical interfaces are allowed at any given time. In the smooth compression regions, the interfaces at the maxima of the pressure gradients are considered critical. The pressure gradients are estimated using simple finite differences. If the Riemann solver at these locations computes sufficiently strong discontinuous waves, then they are tracked. The critical interfaces, which carry these waves, are treated the same way at the next time level along with other possible critical interfaces that may be detected. When there are two adjacent critical interfaces, the two Riemann problems are solved simultaneously. At this point it is decided if collisions will occur within the timestep Δt . There are six waves resulting from the two Riemann problems and there are four cell interfaces available to do the tracking. The strongest waves are tracked and the others are ignored. This procedure has proven to be very robust in handling all possible wave interactions.

Collisions and reflections from walls can be treated in a straightforward way using this adaptive grid. A typical collision case is shown in Fig. 5. At time t , two strong shock waves at the interfaces $i - \frac{1}{2}$ and $i + \frac{1}{2}$, are moving at each other with speeds that allow for a collision before time $t + \Delta t$. The Riemann problems at the interfaces $i - \frac{1}{2}$ and $i + \frac{1}{2}$ are solved at time t , simultaneously. The solution indicates that there will be a collision within the time interval Δt . The time step is adjusted locally, i.e., only for the three cells $i - 1$, and $i + 1$, so that at the intermediate time instant the collision point coincides with the cell boundary $i + \frac{1}{2}$. The Riemann solver at this interface, at the intermediate time instant, will compute the two shock waves emerging from the collision and the adjacent cell boundaries

will be able to track them in the same way at subsequent times. The fluxes at the interfaces $i - \frac{1}{2}$ and $i + \frac{1}{2}$ are held constant for the whole timestep Δt . This leads to a robust way of handling wave interactions, without loss of accuracy.

3. RIEMANN SOLVER

The Riemann solver is an important ingredient of the numerical scheme. It provides the means for computing the velocity and the pressure at the cell interfaces and, thus, the various flux terms required. It also gives valuable information about the local waves emanating from each cell interface. As explained in the previous section, the Lagrangian grid adapts in such a way that important discontinuous waves and collision points coincide with cell boundaries at each time instant. It is, therefore, necessary to be able to identify the waves emanating from these critical cell boundaries at subsequent times. This is what the Riemann solver accomplishes. A variety of exact and approximate Riemann solvers have appeared in the literature in recent years. In all these solvers the focus is on computing the velocity and pressure of the contact discontinuity, which appears after the breakup of the initial discontinuity of the Riemann problem. In the present scheme it is crucial to identify the exact wave pattern as well. This information is used to assign the appropriate velocities to adjacent cell boundaries so that all important waves are tracked and to adjust the time step locally so that collisions are computed accurately. Moreover, the fluxes at an interface need to be computed along the ray $\xi(t) = v_b$; see Eq. (31b). Most interfaces are Lagrangian and hence, $v_b = 0$.

3.1. Non-reacting Perfect Gas

Consider the case of the Riemann problem for inviscid flow of a perfect gas without chemical reactions. The initial condition at time $t = 0$ consists of two constant states denoted by the subscripts r and l . Note that it is possible to have two different perfect gases on either side of the $\xi = 0$ location, as indicated by the different specific heat ratios, i.e., γ_r and γ_l ; see Fig. 6. The space variable ξ is the

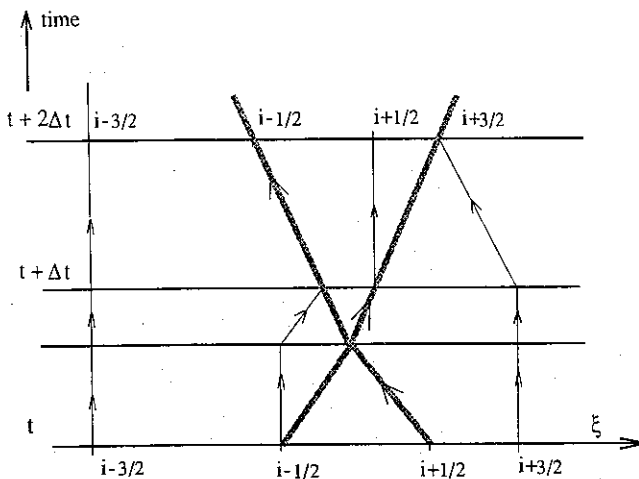


FIG. 5. The typical collision of two shocks is shown. The time step is adjusted locally so that the collision point coincides with the cell interface $i + \frac{1}{2}$ at the intermediate time step.

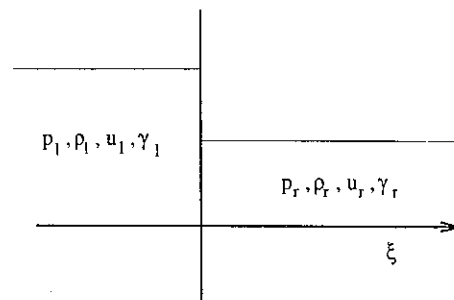


FIG. 6. Initial condition for the Riemann problem. The variable ξ is the Lagrangian space coordinate.

Lagrangian space coordinate. At time $t=0^+$ the general wave pattern shown in Fig. 7 will develop.

There is a wave moving to the right (positive ξ) denoted by R , a wave moving to the left (negative ξ) denoted by L , and a contact discontinuity C which remains at $\xi=0$ for all time, i.e., moves with the local fluid velocity. The waves R and L are either shocks or expansion waves, depending on the initial condition. Across the contact discontinuity C the pressure p_f and velocity u_f are continuous, but the density has a jump discontinuity at $\xi=0$ for all time. The density is ρ_{fl} for $\xi < 0$ and ρ_{fr} for $\xi > 0$. It is known that the solution to this initial value problem exists and is unique for arbitrary initial conditions. Moreover, the solution is self-similar and the shock waves propagate with a constant velocity and strength. That is why they are represented by straight lines in the (ξ, t) diagram.

There are four wave patterns possible for this problem. The solution will be found for each of these wave patterns for the special case of a perfect gas.

(i) *L-shock, R-shock.* Across the shock R the following relationship holds:

$$r \equiv \frac{u_f - u_r}{a_r} = \frac{2}{\gamma_r + 1} \left(M_r - \frac{1}{M_r} \right). \quad (35)$$

M_r is the shock Mach number defined by

$$M_r \equiv \frac{U_r - u_r}{a_r}, \quad (36)$$

where U_r is the shock velocity and $a_r = \sqrt{\gamma_r p_r / \rho_r}$ is the speed of sound in the undisturbed region r . Similarly for the shock L ,

$$\frac{u_i - u_f}{a_i} = \frac{2}{\gamma_i + 1} \left(M_i - \frac{1}{M_i} \right). \quad (37)$$

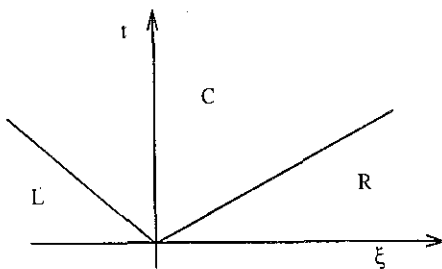


FIG. 7. General wave pattern resulting from the breakup of the original discontinuity of the Riemann problem. C is a contact discontinuity. L and R can be either shocks or expansion waves.

where M_i is the shock Mach number for L . Equations (35) and (37) can be solved for the shock Mach numbers to give

$$M_r = \frac{\gamma_r + 1}{4} r + \sqrt{\left(\frac{\gamma_r + 1}{4} \right)^2 r^2 + 1}, \quad (38)$$

$$M_i = \frac{\gamma_i + 1}{4} \frac{u_i - u_f}{a_i} + \sqrt{\left(\frac{\gamma_i + 1}{4} \right)^2 \left(\frac{u_i - u_f}{a_i} \right)^2 + 1}. \quad (39)$$

The pressure ratios across the two shocks are given by the equations

$$\frac{p_f}{p_r} = 1 + \frac{2\gamma_r}{\gamma_r + 1} (M_r^2 - 1), \quad (40)$$

$$\frac{p_f}{p_i} = 1 + \frac{2\gamma_i}{\gamma_i + 1} (M_i^2 - 1). \quad (41)$$

From Eqs. (38)–(41) one obtains a single equation for the unknown r ,

$$G(r) \equiv 1 - \frac{p_i}{p_r} + \gamma_r \frac{\gamma_r + 1}{4} r^2 + \gamma_r r \sqrt{\left(\frac{\gamma_r + 1}{4} \right)^2 r^2 + 1} - \frac{p_i}{p_r} \gamma_i \frac{\gamma_i + 1}{4} \left(\frac{u_i - u_r}{a_i} - \frac{a_r}{a_i} r \right)^2 - \frac{p_i}{p_r} \gamma_i \left(\frac{u_i - u_r}{a_i} - \frac{a_r}{a_i} r \right) \times \sqrt{\left(\frac{\gamma_i + 1}{4} \right)^2 \left(\frac{u_i - u_r}{a_i} - \frac{a_r}{a_i} r \right)^2 + 1} = 0. \quad (42)$$

This equation is solved numerically using a Newton-Raphson method. Once r is obtained, all other quantities of interest follow from Eqs. (35)–(41). The densities are determined by

$$\frac{\rho_{fi}}{\rho_i} = \frac{(\gamma_i + 1) M_i^2}{2 + (\gamma_i - 1) M_i^2}, \quad i = r, l. \quad (43)$$

It is important to be able to determine if this wave pattern will develop for a given initial condition. For this solution to be possible, certain compatibility conditions must hold. These are easily found by noticing that in Eqs. (35) and (37) the shock Mach numbers M_r and M_i must be greater than 1. It then follows that the following compatibility condition

$$u_r \leq u_f \leq u_i \quad (44)$$

must hold or, equivalently,

$$\begin{aligned} u_r - u_l &\leq 0, \\ 0 \leq r &\leq \frac{u_l - u_r}{a_r}. \end{aligned} \tag{45}$$

(ii) *L-expansion wave, R-shock*. In this case, Eqs. (35), (36), (38), and (40), derived previously, still hold for the shock wave *R*. In addition to these equations, the following equation gives the pressure ratio across the isentropic expansion wave,

$$\begin{aligned} \frac{p_f}{p_l} &= \left(1 + \frac{\gamma_l - 1}{2} \frac{u_l - u_f}{a_l}\right)^{2\gamma_l/(\gamma_l - 1)} \\ &= \left(1 + \frac{\gamma_l - 1}{2} \frac{u_l - u_r}{a_l} - \frac{\gamma_l - 1}{2} \frac{a_r}{a_l} r\right)^{2\gamma_l/(\gamma_l - 1)}, \end{aligned} \tag{46}$$

where *r* is defined in Eq. (35). Combining Eqs. (38), (40), and (46), a single equation in *r* is obtained, as in the previous case,

$$\begin{aligned} F(r) &\equiv 1 + \gamma_r \frac{\gamma_r + 1}{4} r^2 + \gamma_r r \sqrt{\left(\frac{\gamma_r + 1}{4}\right)^2 r^2 + 1} \\ &- \frac{p_l}{p_r} \left(1 + \frac{\gamma_l - 1}{2} \frac{u_l - u_r}{a_l} - \frac{\gamma_l - 1}{2} \frac{a_r}{a_l} r\right)^{2\gamma_l/(\gamma_l - 1)} = 0, \end{aligned} \tag{47}$$

which is solved numerically. The densities are determined by Eq. (43) across the shock and by the isentropic relation

$$\frac{\rho_f}{\rho_l} = \left(\frac{p_f}{p_l}\right)^{1/\gamma}$$

across the expansion wave.

The compatibility conditions are found by noting that across the expansion wave *L*, $0 \leq p_f/p_l \leq 1$ and across the shock *R*, $p_f/p_r \geq 1$. Using Eqs. (40) and (46) the following relations are found, after some algebra,

$$\begin{aligned} p_r/p_l &\leq 1, \\ u_r - u_l &< \left(\frac{2}{\gamma_l - 1}\right) a_l, \end{aligned} \tag{48}$$

and

$$\begin{aligned} \frac{u_l - u_r}{a_r} &\leq r < \frac{u_l - u_r}{a_r} + \left(\frac{2}{\gamma_l - 1}\right) \frac{a_l}{a_r} \\ 0 &\leq r. \end{aligned}$$

(iii) *L-shock, R-expansion wave*. This case is exactly the same as case (ii) with the transformation $\xi \rightarrow -\xi$.

(iv) *L-expansion wave, R-expansion wave*. In this case, there are two expansion waves and the pressure ratios across them are given by

$$\begin{aligned} \frac{p_f}{p_l} &= \left(1 + \frac{\gamma_l - 1}{2} \frac{u_l - u_f}{a_l}\right)^{2\gamma_l/(\gamma_l - 1)}, \\ \frac{p_f}{p_r} &= \left(1 + \frac{\gamma_r - 1}{2} \frac{u_f - u_r}{a_r}\right)^{2\gamma_r/(\gamma_r - 1)}. \end{aligned} \tag{50}$$

From Eqs. (50) the following single equation in *r* is obtained,

$$\begin{aligned} S(r) &\equiv \left(1 + \frac{\gamma_r - 1}{2} r\right)^{2\gamma_r/(\gamma_r - 1)} \\ &- \frac{p_l}{p_r} \left(1 + \frac{\gamma_l - 1}{2} \frac{u_l - u_r}{a_l} - \frac{\gamma_l - 1}{2} \frac{a_r}{a_l} r\right)^{2\gamma_l/(\gamma_l - 1)} = 0, \end{aligned} \tag{51}$$

which is solved numerically with the Newton-Raphson method. The compatibility conditions are once again found by noting that across the expansion waves $0 \leq p_f/p_l \leq 1$ and $0 \leq p_f/p_r \leq 1$, which, using Eqs. (50), give

$$0 \leq u_r - u_l < 2 \left(\frac{a_r}{\gamma_r - 1} + \frac{a_l}{\gamma_l - 1}\right) \tag{52}$$

and

$$\begin{aligned} -\frac{2}{\gamma_r - 1} &< r \leq 0, \\ \frac{u_l - u_r}{a_r} &\leq r < \frac{u_l - u_r}{a_r} + \left(\frac{2}{\gamma_l - 1}\right) \frac{a_l}{a_r}. \end{aligned} \tag{53}$$

3.2. Acoustic Approximation

The solution to the Riemann problem becomes easier to obtain when the initial conditions are such that the waves *R* and *L* shown in Fig. 7 are so weak that linear acoustic theory can be used. This happens when the distance, in some sense, between the two constant states *r* and *l* is small. The waves *R* and *L* can then be treated as acoustic waves with the pressure ratios across them given by the simple relations,

$$p_f = p_r + \sqrt{\gamma_r p_r \rho_r} (u_f - u_r), \tag{54a}$$

$$p_f = p_l - \sqrt{\gamma_l p_l \rho_l} (u_f - u_l). \tag{54b}$$

Combining Eqs. (54a) and (54b), one finds

$$\begin{aligned} u_f &= (p_l - p_r + \sqrt{\gamma_r p_r \rho_r} u_r \\ &+ \sqrt{\gamma_l p_l \rho_l} u_l) / (\sqrt{\gamma_r p_r \rho_r} + \sqrt{\gamma_l p_l \rho_l}). \end{aligned} \tag{55}$$

The densities behind these waves are given by

$$\rho_{fi} = \rho_i(p_f + \mu_i^2 p_i)/(p_i + \mu_i^2 p_i), \quad (56)$$

where

$$\mu_i^2 \equiv (\gamma_i - 1)/(\gamma_i + 1), \quad i = r, l. \quad (57)$$

3.3. Reacting Mixture of Calorically Perfect Gases

So far, the classical Riemann problem for non-reacting inviscid flow has been considered. The solution to this problem, as mentioned before, is a self-similar solution, i.e., depending on x/t only. For the case of a simple reacting mixture the nonlinear system of equations, that needs to be solved, is of the form

$$\frac{\partial U}{\partial t} + \frac{\partial F(U)}{\partial x} = G(U), \quad (58)$$

where

$$U = \begin{pmatrix} \rho \\ \rho u \\ \rho(e + \frac{1}{2} u^2) \\ \rho z \end{pmatrix}, \quad F(U) = \begin{pmatrix} \rho u \\ \rho u^2 + p \\ \rho u(e + \frac{1}{2} u^2) + pu \\ \rho zu \end{pmatrix} \quad (59)$$

and

$$G(U) = \begin{pmatrix} 0 \\ 0 \\ 0 \\ -\rho \dot{z} \end{pmatrix}. \quad (60)$$

This is written using the Eulerian formulation, but one obtains a system of exactly the same form, if the Lagrangian formulation is used. The Riemann problem solution,

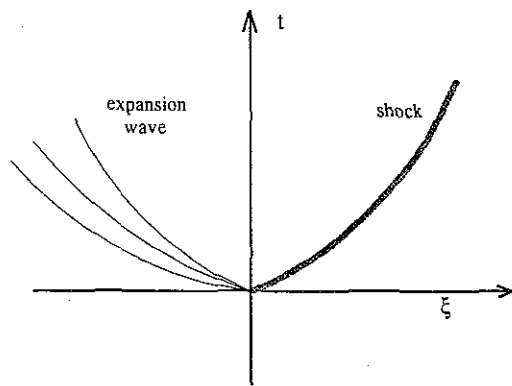


FIG. 8. This is a typical wave pattern resulting from the breakup of the initial discontinuity of the Riemann problem for the case of a simple reacting mixture. The solution is no longer self-similar.

described so far, is for the non-reacting case, i.e., $G(U) = 0$. For the reacting case, jumps in the concentration of unburnt gas z are allowed only across contact discontinuities, but not across shocks. The solution to this problem is more complicated and no longer self-similar. In Fig. 8, a typical wave pattern is shown. The shock and expansion waves are curved in the (ξ, t) plane; i.e., they are accelerating. The solution to this generalized Riemann problem has been worked out by Matania Ben-Artzi [1]. It is shown that the solution approaches the solution of the classical Riemann problem for the non-reacting case in the limit $\xi \rightarrow 0$ and $t \rightarrow 0$. The more complicated generalized Riemann solver given by Ben-Artzi provides higher order accuracy over the usual non-reacting solver. Numerical experiments were performed using the present adaptive Lagrangian scheme with both Riemann solvers. It was found that the simpler solver gave results which were just as good. The acceleration of the various waves was captured numerically quite accurately.

4. NUMERICAL RESULTS

A number of test cases were run using this numerical scheme. The cases were chosen primarily to validate the code and to demonstrate its potential for solving 1D problems with complicated wave interactions. The scheme is particularly useful for computing unsteady reacting flows involving detonation waves and their interactions.

4.1. Sod's Shock-Tube Problem

The first case is the classical shock-tube problem. It is an important validation run for the code. The initial conditions used are those proposed by Sod [13]. At time $t = 0$ a diaphragm at the location $x = 0.5$ separates the two constant states

$$\begin{aligned} p_l = 1.0, \quad \rho_l = 1.0, \quad u_l = 0.0, \quad x < 0.5 \\ p_r = 0.1, \quad \rho_r = 0.125, \quad u_r = 0.0, \quad x > 0.5, \end{aligned} \quad (61)$$

for a perfect gas with $\gamma = 1.40$. $N = 150$ computational cells are used in this calculation. In all the results presented, the solutions are given as functions of the Eulerian space variable x , even though the calculation is done in Lagrangian space. The Lagrangian aspect of the scheme is evident by the increased density of computational points in compression regions. The comparison between the numerical solution and the exact solution shown in Fig. 9 is excellent. Note that the expansion wave is computed with the accuracy of typical shock-capturing schemes, since no effort is made to track expansion waves. The shock wave and the contact discontinuity are computed with no smearing.

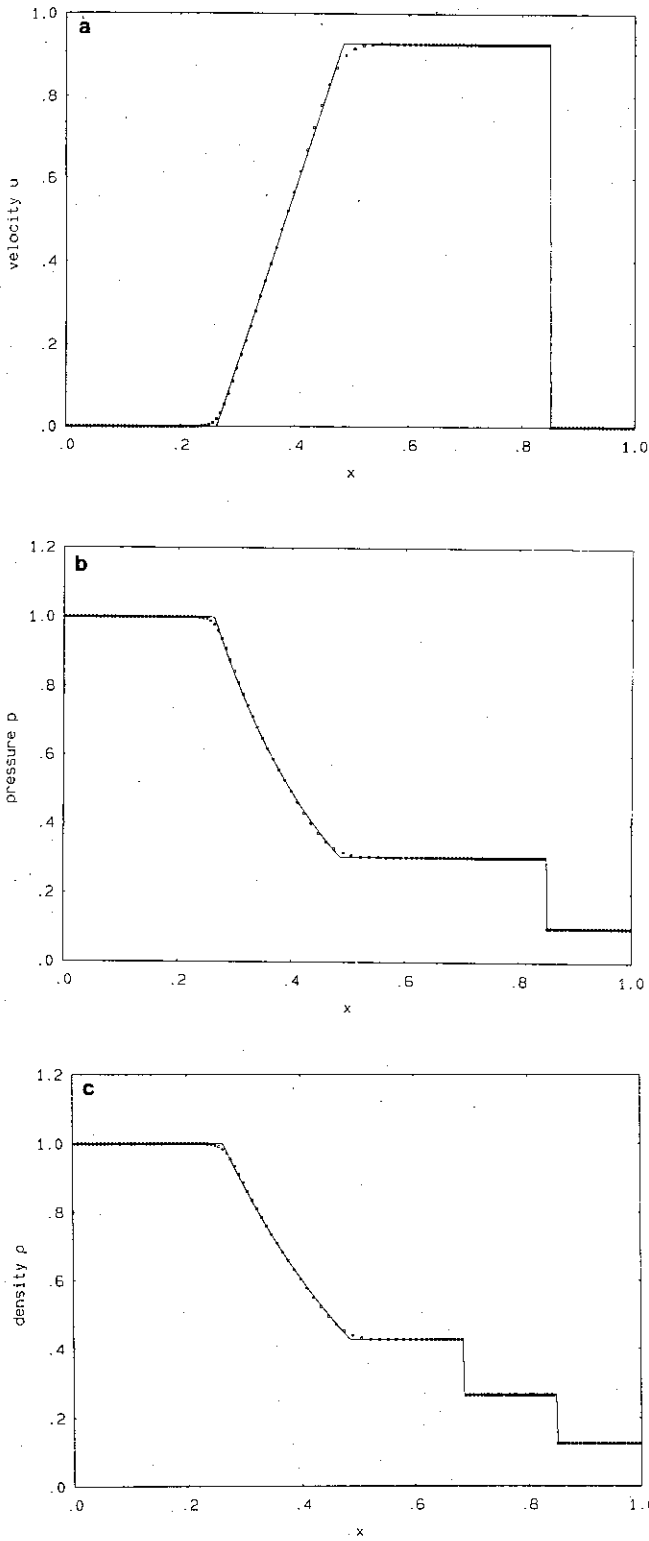


FIG. 9. (a) Velocity profile at time $t=0.20$ for Sod's shock tube problem with $N=150$ computational cells. (b) Pressure profile at time $t=0.20$ for Sod's shock tube problem with $N=150$ computational cells. (c) Density profile at time $t=0.20$ for Sod's shock tube problem with $N=150$ computational cells. The solid lines represent the exact solutions and the boxes represent the numerical solutions.

In order to demonstrate the ability of the scheme to compute complicated wave interactions accurately, the shock tube problem is carried a step further. Reflecting walls are assumed present at the locations $x=0$ and $x=1$. The computation is continued to see how the multiple reflections of the shock from the walls and its collisions with the contact discontinuity are calculated. In Fig. 10, the solution is shown after the first reflection of the shock wave from the wall at $x=1$, which occurs at $t=0.285$. In Fig. 11, the reflected shock has collided with the contact discontinuity and a new shock wave has been generated. The solution at a later time is shown in Figs. 12. The computation was carried out until time $t=7.88$. That corresponds to many reflections of the original shock. In a real experiment viscous effects would have made the process die down much sooner. In Fig. 13, the entropy of the system is shown as a function of time. The entropy is defined by

$$s \equiv \ln(p/\rho^\gamma). \tag{62}$$

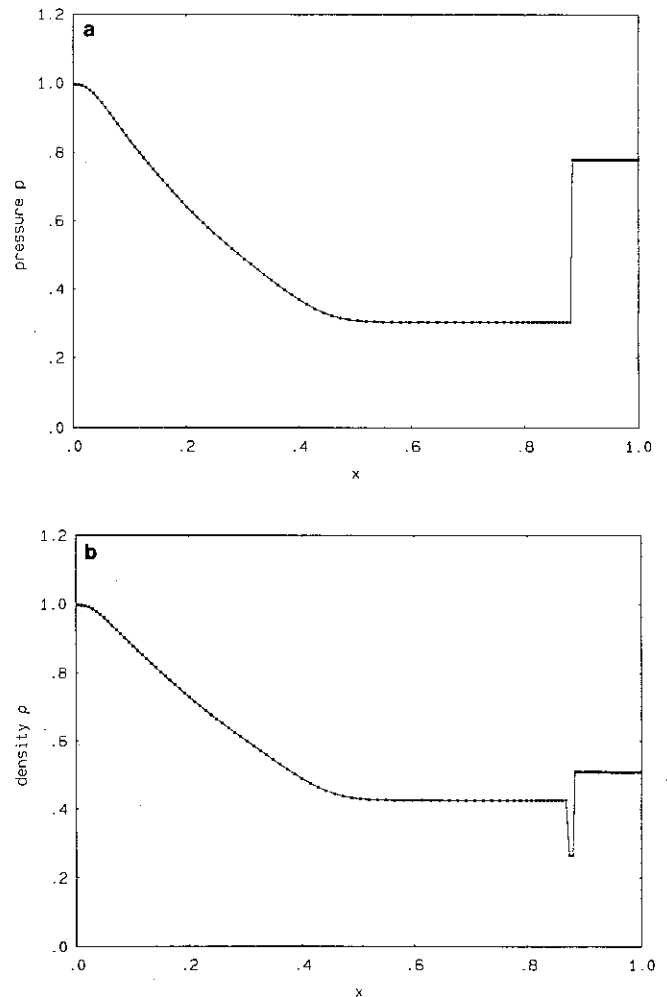


FIG. 10. (a) Pressure profile at time $t=0.40$. (b) Density profile at time $t=0.40$. The shock has reflected from the wall at $x=1$.

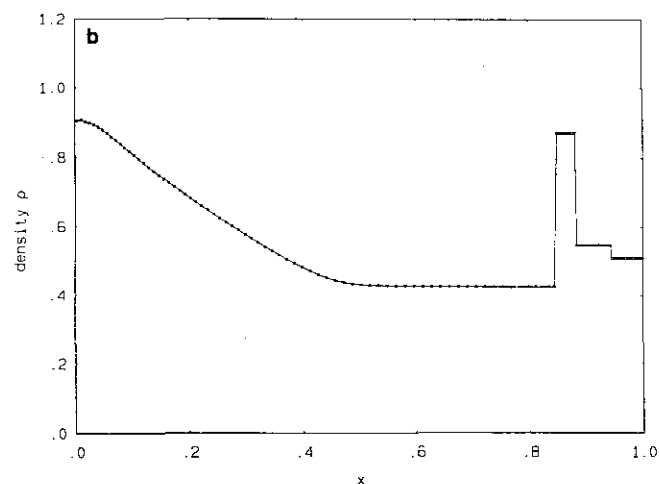
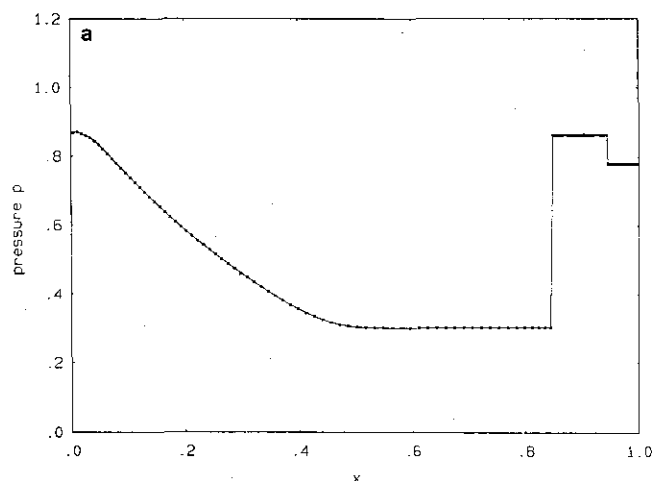


FIG. 11. (a) Pressure profile at time $t=0.45$. (b) Density profile at time $t=0.45$. The reflected shock has collided with the contact discontinuity. A secondary shock has been generated.

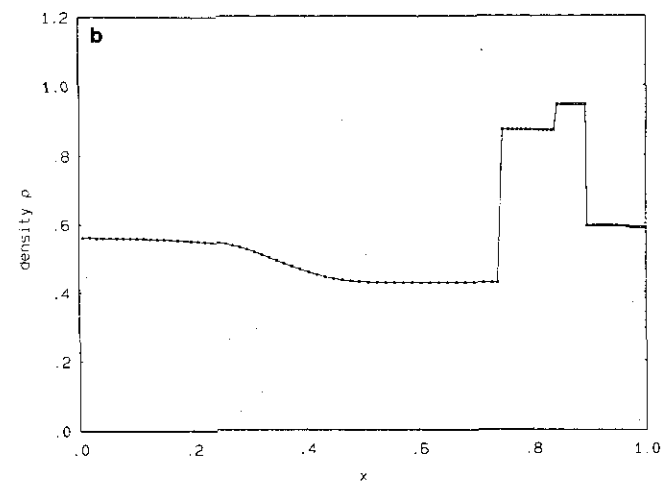
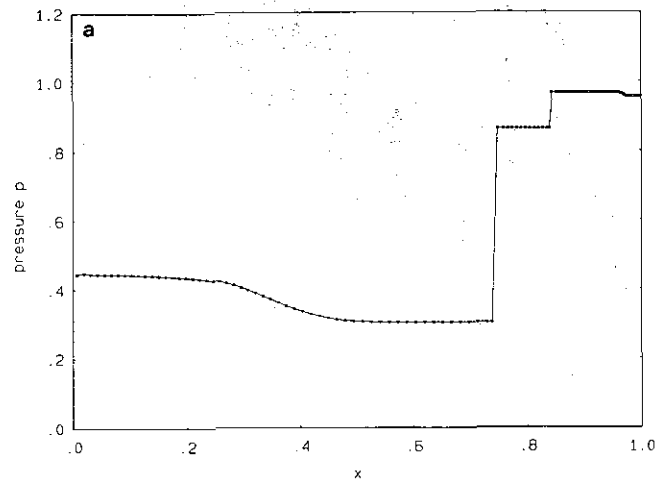


FIG. 12. (a) Pressure profile at time $t=0.61$. (b) Density profile at time $t=0.61$. An acoustic wave has been generated from the collision of the secondary shock with the contact discontinuity.

As $t \rightarrow \infty$, the system approaches the state predicted by thermodynamics, since the scheme is fully conservative. Any scheme which conserves total mass and energy will give the correct final entropy. In this case it is $s=0.1168$ in the appropriate dimensionless units. This is an important point worth repeating here. The conservative character of the scheme is not compromised by the use of the adaptive grid technique.

4.2. Strong Shock Wave Problem

The strong shock wave problem used by Woodward and Colella [18] is computed with the present scheme. This problem is a good test case because of the strong interacting discontinuous waves. The initial condition is that of a gas

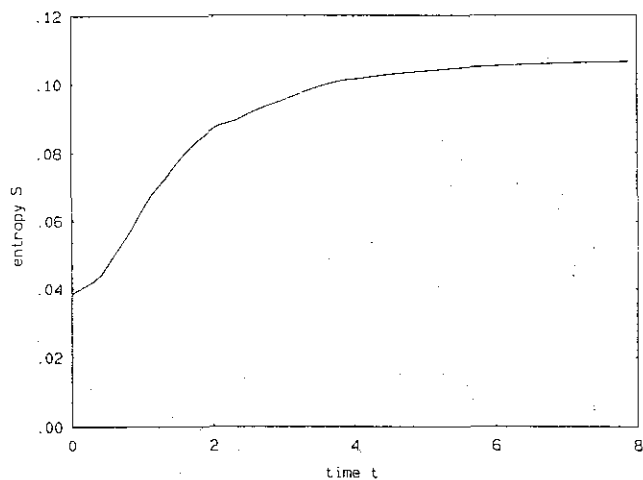


FIG. 13. Entropy $s = \ln(p/\rho^\gamma)$ of the system as a function of time for the shock tube problem with multiple reflections.

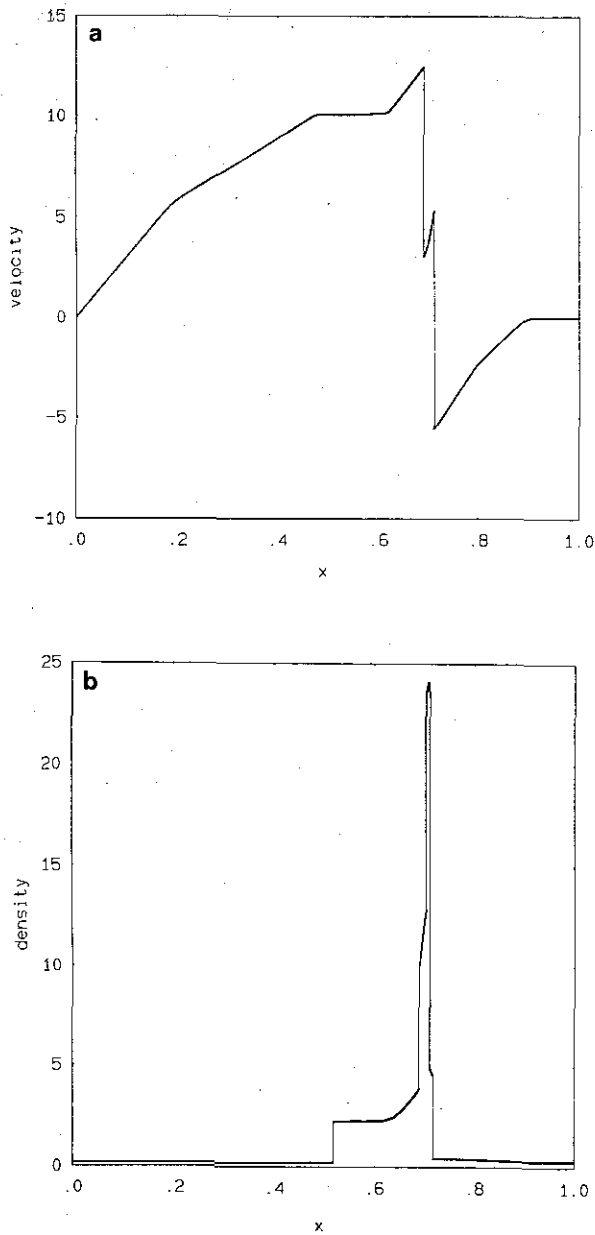


FIG. 14. (a) Velocity profile and (b) density profile at time $t = 0.030$ for the strong shock wave problem.

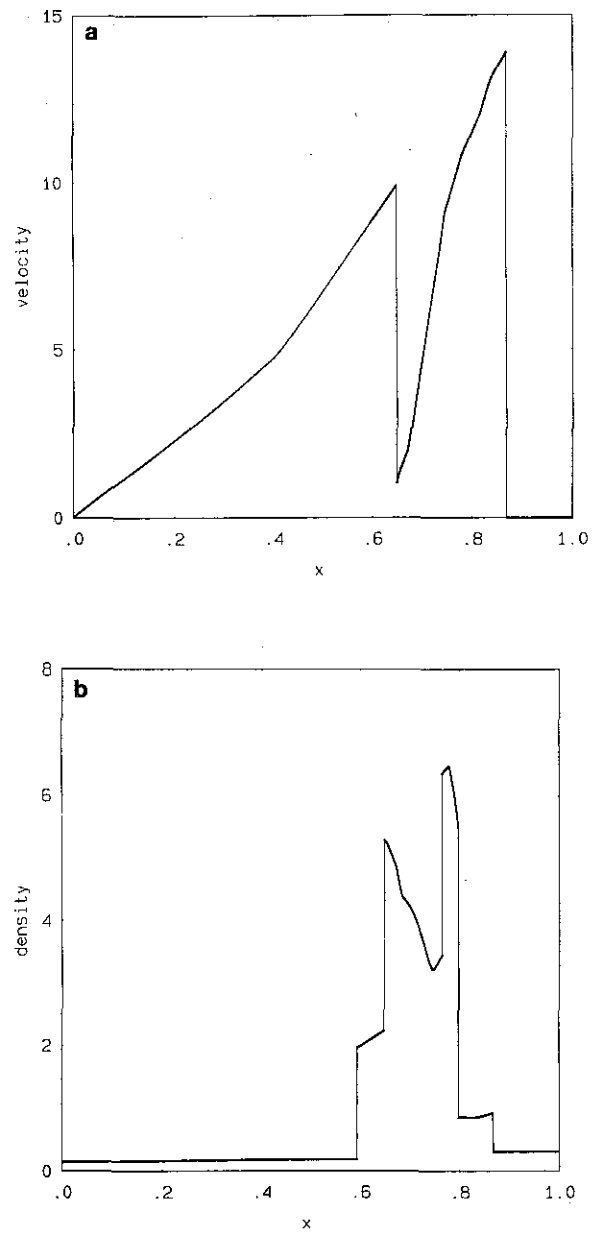


FIG. 15. (a) Velocity profile and (b) density profile at time $t = 0.038$ for the strong shock wave problem.

with specific heat ratio $\gamma = 1.4$ at rest in the tube $0 \leq x \leq 1$. The initial density is $\rho = 1$ and the pressure is

$$\begin{aligned} p &= 1000, & x < 0.1, \\ p &= 0.01, & 0.1 < x < 0.9, \\ p &= 100, & 0.9 < x < 1. \end{aligned} \tag{63}$$

The results are shown in Figs. 14 and 15 for the times $t = 0.030$ and $t = 0.038$, respectively; 800 computational cells were used for this calculation.

4.3. ZND Detonation Waves

Another test case is that of a steady detonation wave. The well-known ZND theory (Zel'dovich-VonNeumann-Doering) for a steady detonation is used to compare with the numerical solution obtained using this scheme. As a first check, the profile of a steady detonation wave, computed using the ZND theory, is given as the initial condition to the unsteady code. The solution after time $t = 10$ (10,000 time steps) is then superimposed on the ZND solution and compared. The comparison, shown in Fig. 16, is excellent.

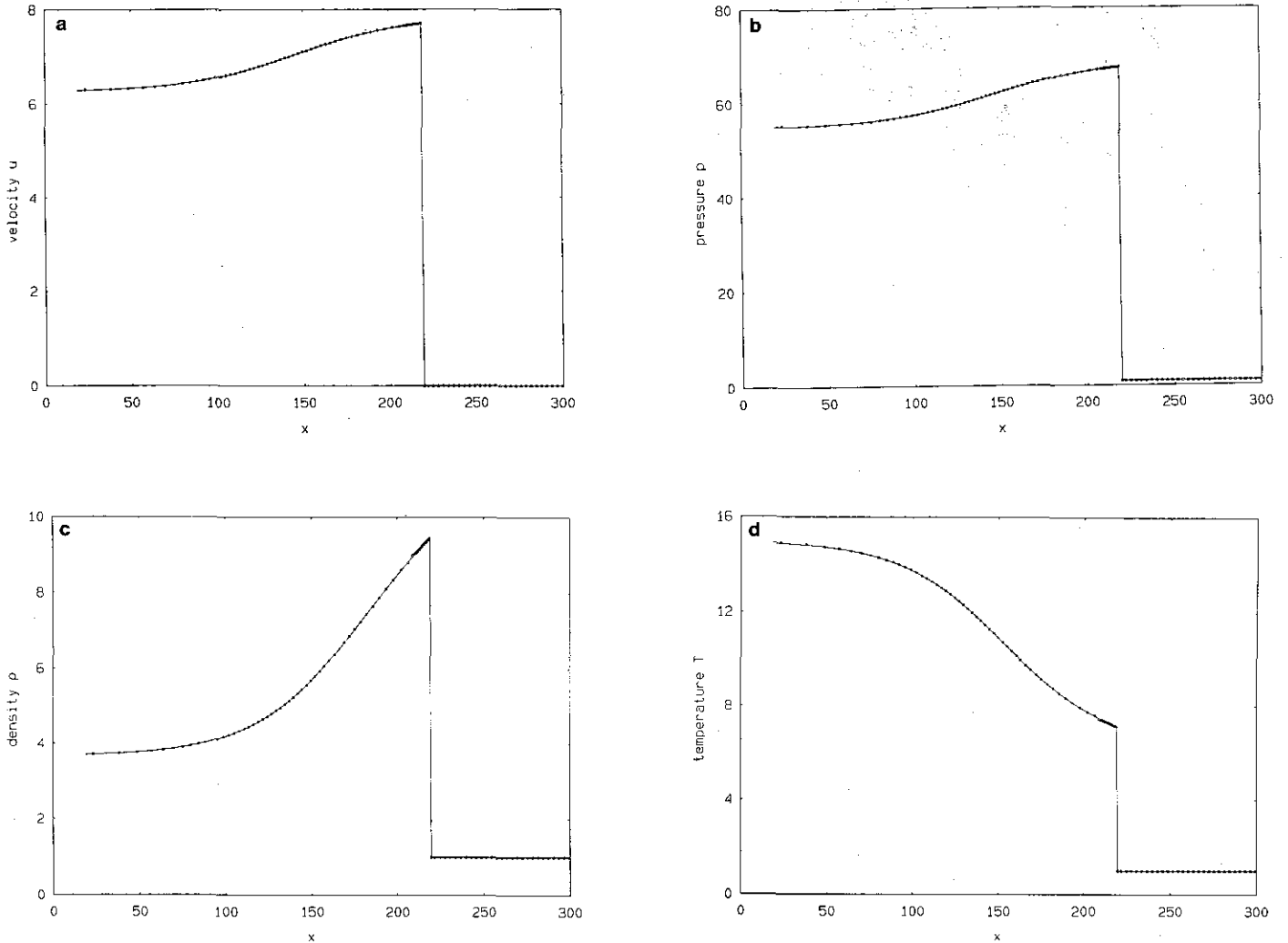


FIG. 16. (a) Velocity profile at $t = 10$. (b) Pressure profile at $t = 10$. (c) Density profile at $t = 10$. (d) Temperature profile at $t = 10$. The solid lines are the solutions given by the ZND theory. The boxes are the numerical solutions.

The standard Arrhenius law, given by Eq. (1a), is used for the chemical reaction rate with $\alpha = 0$, i.e.,

$$\dot{z} = -KzT^\alpha \exp(-E/R_g T).$$

The parameters used for this test run are

$$\gamma = 1.2, \quad q_0/R_g T_0 = 50, \quad E/R_g T_0 = 40,$$

where the subscript zero denotes the undisturbed region into which the detonation propagates. This steady detonation wave corresponds to an overdrive factor of $f = 1.6$. The overdrive factor is defined by

$$f = D^2/D_{CJ}^2,$$

where D is the detonation wave speed and D_{CJ} is the detona-

tion speed corresponding to the Chapman–Jouguet point. For details on the ZND theory see the book by Fickett and Davis [4].

The case of unsteady detonation waves will now be considered. For the following cases the simplified Arrhenius chemical rate law is used (Eq. (1b)), i.e.,

$$\dot{z} = -KzH(T - T_c),$$

where T_c is a critical temperature above which the chemical reaction begins. Figure 17 shows the evolution of an unsteady detonation propagating in an undisturbed region. It is the well-known piston problem. The motion of the piston, starting at $x = 0$, generates a shock which raises the temperature of the gas above the critical value T_c . The chemical reaction begins and the detonation wave

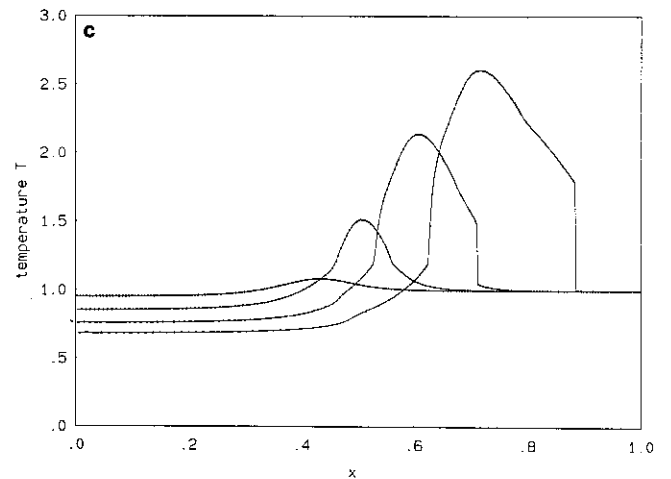
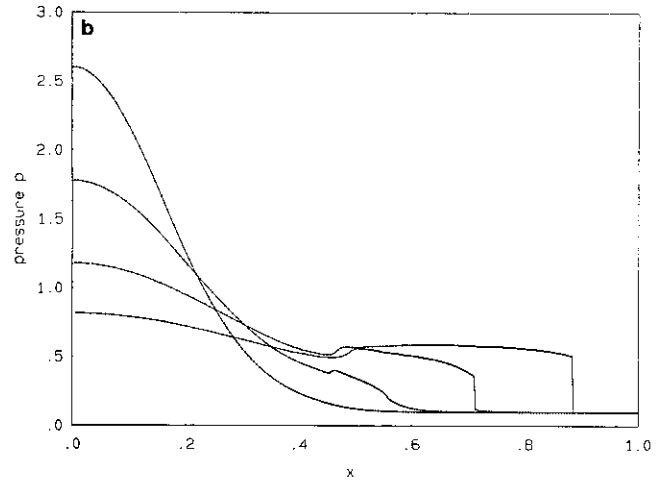
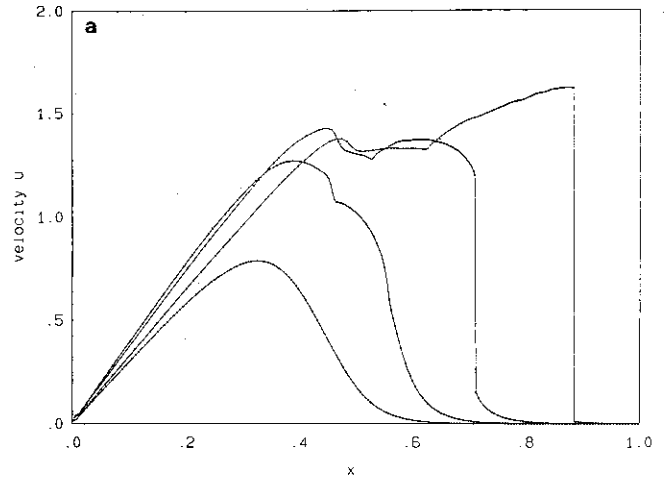
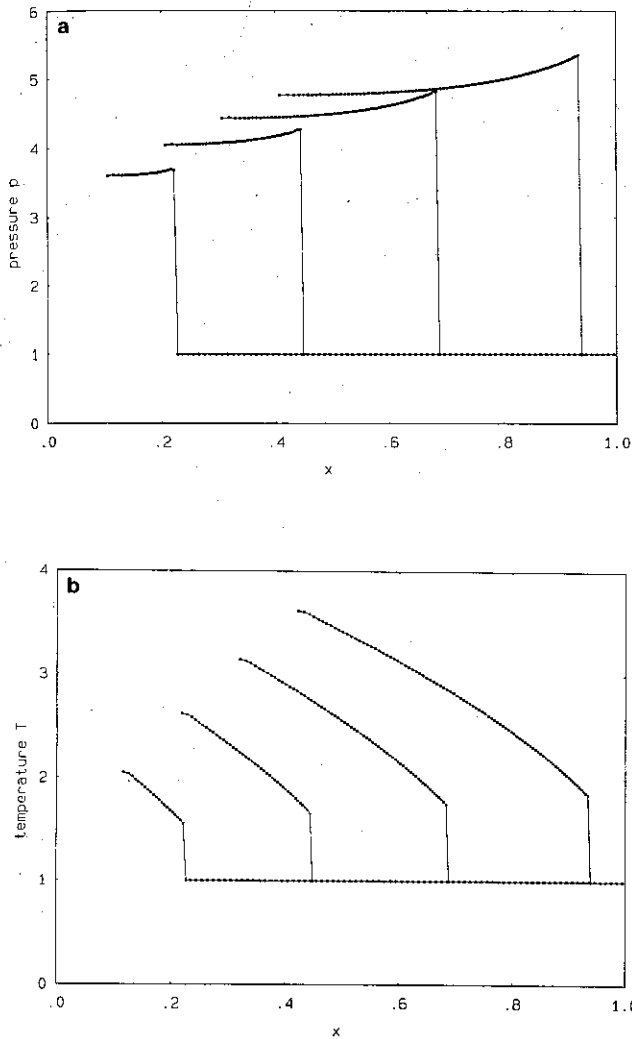


FIG. 17. (a) Pressure profiles for the piston problem. (b) Temperature profiles for the piston problem. The detonation waves generated accelerate into the undisturbed region. In this case the critical temperature is $T_c = 1.3$; times $t = 0.1, 0.2, 0.3, 0.4$.

accelerates into the undisturbed region. The numerical values used in this run are

$$\gamma = 1.4, \quad q_0 = 20, \quad T_c = 1.3,$$

where all quantities are normalized with the corresponding values in the undisturbed region. The piston velocity is taken to be $u_p = 1$.

A more interesting case is shown in Fig. 18. The initial condition is a smooth pressure distribution with zero initial velocity, which leads to isentropic compression and, eventually, shock formation. If in this compression the temperature of the gas becomes larger than T_c , then the chemical reaction starts and a detonation wave is generated. The formation of the shock from a smooth flow is captured

FIG. 18. (a) Velocity profiles for a smooth compression. (b) Pressure profiles for a smooth compression. (c) Temperature profiles for a smooth compression. When the compression raises the temperature above the critical value $T_c = 1.2$ the reaction begins and a detonation wave is formed; times $t = 0.075, 0.150, 0.225, 0.300$.

very well by this scheme. $N = 200$ computational cells were used. The numerical values used in this run are

$$\gamma = 1.4, \quad q_0 = 20, \quad T_c = 1.2, \quad K = 1,$$

where all quantities are normalized appropriately. The normalization is such that the initial temperature of the gas at rest is $T_0 = 1$ or, equivalently, $\rho_0 = p_0$ in dimensionless units. The initial pressure distribution is given by

$$p_0(x) = 0.10 + 3.0 \exp(-25x^2).$$

5. CONCLUSIONS

An adaptive numerical scheme has been presented for the computation of flows with complicated interactions of discontinuous waves. Its accuracy and robustness, as demonstrated by numerical experiments make it a valuable tool, especially for the study of unsteady reacting flows with detonation waves. The conservative formulation gives the method all the advantages of higher-order shock-capturing schemes and its adaptive characteristic allows for good accuracy near shocks with no smearing effect. The advantages of the conservative shock-capturing schemes are combined with the advantages of the front-tracking methods very well to give a useful computational scheme.

The drawback is that the extension of this scheme to multidimensional flows is not straightforward. The main idea of the scheme is the conservative front-tracking of shocks and contact discontinuities on a Lagrangian grid. The Lagrangian aspect of the method is the most difficult

to extend. The conservative front-tracking aspect can be extended and work in this area is in progress.

ACKNOWLEDGMENTS

This work is part of a larger effort to investigate mixing and combustion, sponsored by the Air Force Office of Scientific Research Grant Nos. 88-0155 and 90-0304, whose support is gratefully acknowledged. The comments and suggestions of the referees are also greatly appreciated.

REFERENCES

1. M. Ben-Artzi, *J. Comput. Phys.* **81**, 70 (1989).
2. M. J. Berger and J. Olinger, *J. Comput. Phys.* **53**, 484 (1984).
3. P. Colella and P. R. Woodward, *J. Comput. Phys.* **54**, 174 (1984).
4. W. Fickett and W. C. Davis, *Detonation* (Univ. of California Press, Berkeley, 1979).
5. S. K. Godunov, *Mar. Sb.* **47**, 271 (1959).
6. A. Harten, *J. Comput. Phys.* **49**, 357 (1983).
7. A. Harten, *SIAM J. Numer. Anal.* **21**, 1 (1984).
8. P. D. Lax and B. Wendroff, *Commun. Pure Appl. Math.* **13**, 217 (1960).
9. H. I. Lee and D. S. Stewart, *J. Fluid Mech.* **216**, 103 (1990).
10. R. W. McCormack, AIAA Paper No. 69-354 (unpublished).
11. J.-L. Montagné, H. C. Yee, and M. Vinokur, *AIAA J.* **27** (10), 1332 (1989).
12. G. Moretti, *Annu. Rev. Fluid Mech.* **19**, 313 (1987).
13. G. A. Sod, *J. Comput. Phys.* **27**, 1 (1978).
14. J. L. Steger and R. F. Warming, *J. Comput. Phys.* **40**, 263 (1981).
15. B. van Leer, *J. Comput. Phys.* **32**, 101 (1979).
16. B. van Leer, in *Lecture Notes in Phys.*, Vol. 170 (Springer-Verlag, New York/Berlin, 1982), p. 507.
17. B. van Leer, *SIAM J. Sci. Stat. Comput.* **5**(1), 1 (1984).
18. P. R. Woodward and P. Colella, *J. Comput. Phys.* **54**, 115 (1984).

APPENDIX D

TOKUMARU, P. T. & DIMOTAKIS, P. E. 1992 "Image correlation velocimetry,"
GALCIT Report FM92-1.

GRADUATE AERONAUTICAL LABORATORIES
CALIFORNIA INSTITUTE of TECHNOLOGY
Pasadena, California 91125

Image correlation velocimetry

By P. T. TOKUMARU AND P. E. DIMOTAKIS

Abstract

This paper focuses on the correlation of two successive scalar images for the purpose of measuring imaged fluid motions. A method is presented for deforming, or transforming, one image to another. Taylor series expansions of the Lagrangian displacement field are used, in conjunction with an integral form of the equations of motion, to approximate this transformation. The proposed method locally correlates images for displacements, rotations, deformations, and higher order displacement gradient fields, and applies a global minimization procedure to insure a global consistency in the results. An integral form of the equations of motion is employed and, as a consequence, no spatial or temporal differentiation of the image data is required in estimating the displacement field. Successive two-dimensional digital CCD images of fluid motion marked with dye, are used to verify the capabilities of the method. The utility of the method is also illustrated using a pair of Voyager 2 images of Jupiter.

GALCIT Report FM92-1

20 November 1992

1. Introduction

The application of photographic, CCD, and other forms of imaging for the purpose of estimating flow velocities, has been investigated by many researchers in fields ranging from fluid mechanics to vision research. In the most common methods for measuring fluid flow velocities, the flow is seeded with particles, or markers, that can be easily imaged and tracked. An extensive review of methods using particle and speckle images for fluid flow measurement is presented by Adrian (1991). The estimation of the motion and deformation of solids is closely related to that of fluids. A method of determining displacements and stress intensity factors in solids, using white light speckle images and image correlation techniques, is presented in McNeill *et al.* 1987. In the absence of particles, flows have also been tagged with a line or grid, *e.g.*, using laser-induced photochemical reactions (Falco & Chu 1987), or laser-induced fluorescence (Miles *et al.* 1989). When this is not possible, one can use markers that occur naturally in the flow, *e.g.*, Bindschadler and Scambos (1991) have correlated the translation of distinct surface features in ice flows to determine flow velocities.

Determining motion from successive images is also of interest in animation, as well as the study of biological and robotic vision. Most investigations along these lines have taken the form of extracting the motion of objects in an image and, as a consequence, they focus on the motion of rigid objects and their representations. See Hildreth & Koch (1987) for a review and Murray & Buxton (1990). This approach is somewhat different from the interests of Fluid Mechanics where the object of interest is a fluid, highly deformable and often compressible. Nevertheless, many results from object motion research apply directly to the motion of fluids and solids.

The proposed Image Correlation Velocimetry (ICV) method that will be developed in the present discussion has roots in both the correlation methods used in measuring fluid flow and the deformation of solids, outlined in Sec. 1.1, and the gradient methods used in measuring optical flows, outlined in Sec. 1.2.

1.1 Correlation methods

Several techniques for determining fluid flow velocities from particle image pairs (*e.g.*, Willert & Gharib 1991) employ an optimization that relies on some form of a cross-correlation function, *e.g.*,

$$\max_{\mathbf{a}} \int_A E_0(\mathbf{x}) E_1(\boldsymbol{\xi}) d^2\mathbf{x}, \quad (1)$$

with

$$\boldsymbol{\xi} = \mathbf{x} + \mathbf{a}, \quad (2)$$

where \mathbf{a} is a vector parameter to be determined by the optimization procedure and A is the correlation region. The distribution of the image irradiance, $E(\mathbf{x}, t)$, is known at times t_0 and t_1 , *i.e.*,

$$E_0(\mathbf{x}) \equiv E(\mathbf{x}, t_0) \quad \text{and} \quad E_1(\mathbf{x}) \equiv E(\mathbf{x}, t_1) . \quad (3)$$

The average velocity, \mathbf{u}_A , within the correlation region is then approximated by,

$$\mathbf{u}_A \approx \frac{\mathbf{a}}{t_1 - t_0} . \quad (4)$$

The drawback of this method, having only two parameters to quantify the motion, is that it cannot resolve displacements properly where there are large displacement gradients within the correlation region. Anticipating this problem, and being very interested in displacement gradients, researchers in Solid Mechanics, apply techniques which include higher order deformations of the displacement field within a correlation volume. For example, McNeill *et al.* (1987) describe a method whereby a model of the image displacement field (mapping) is used in a least squares optimization procedure, *i.e.*,

$$\min_{\mathbf{a}, \nabla \mathbf{a}} \int_A [E_0(\mathbf{x}) - E_1(\xi)]^2 d^2\mathbf{x} . \quad (5)$$

The affine mapping,

$$\xi = \mathbf{x} + \mathbf{a} + (\nabla \mathbf{a}) \cdot d\mathbf{x} , \quad (6)$$

is used as an example of such a function, and the displacement \mathbf{a} and the four components of $\nabla \mathbf{a}$ are treated as parameters to be determined by the optimization procedure. However, any physically motivated mapping can be used in place of Eq. 6.

In both these methods, the image data are integrated over a region and require no spatial differentiation. Since, for two-dimensional images, only a few parameters are extracted from the optimization, these methods are relatively immune to noise and lend themselves to fast solutions.

1.2 Gradient methods

A method for determining the velocities of visual features in an image was presented by Horn & Schunck (1981). This visual velocity is termed "optical flow" to differentiate it from the velocities of (material) objects in an image, *e.g.*, a shadow moving across the ground has a perceived velocity that is markedly different from that of the ground, and a rotating featureless disk will have no visual velocity at all. The fundamental equation used by Horn & Schunck to determine the optical flow was,

$$\frac{\partial E}{\partial t} + \mathbf{u} \cdot \nabla E = 0 , \quad (7)$$

where E is the image irradiance (a scalar) and \mathbf{u} is the optical flow velocity. The differential terms, $\partial E/\partial t$ and ∇E , can be estimated from the image data and the component of \mathbf{u} along ∇E is calculated using Eq. 7. Methods employing equations of this type are called gradient schemes. Note that no velocity can be calculated using Eq. 7 if there are no features or gradients in the image, *i.e.*, if $\nabla E = 0$. In addition, because Eq. 7 employs only the component of \mathbf{u} along ∇E , velocity components along the equi-scalar contours of E cannot be determined using Eq. 7 alone. This limitation was designated the ‘‘aperture problem’’ by Wallach (1976). The terminology is somewhat misleading and is only used here in reference to the convention. More appropriate names might be the ‘‘characteristic problem,’’ or the ‘‘direction problem,’’ because the problem is finding the velocity along the characteristic direction, $E = \text{constant}$. Gradient schemes also have the problem that finite difference approximations of the spatial and temporal derivatives are necessary. A problem with such approximations for the derivatives is related to the Nyquist sampling criterion, where aliasing in the image data can effect the velocity estimates. To minimize this problem in taking the gradient, the motion between images should be less than half the smallest local spatial scale, λ_E , of the E -field, *i.e.*,

$$\frac{|\mathbf{u}| (t_1 - t_0)}{\lambda_E} < \frac{1}{2} \quad (8)$$

(*cf.* Eq. 7), where $(t_1 - t_0)$ is the time between images.

The uncertainty of the so-called aperture problem can be solved in some cases by applying constraints to the motion, *e.g.*, the motion is of a rigid body (see Murray & Buxton 1990, for example), or a limited class of deformable bodies (see Terzopoulos & Metaxas 1991).

Horn & Schunck (1981) applied a global constraint to Eq. 7 (in two dimensions), by solving for $\mathbf{u}(\mathbf{x}, t)$ using an optimization, *i.e.*,

$$\min_{\mathbf{u}(\mathbf{x}, t)} \int_A \left(\left[\frac{\partial E}{\partial t} + \mathbf{u} \cdot \nabla E \right]^2 + k \sigma^2 \right) d^2\mathbf{x}, \quad (9)$$

where σ represents the constraint cost function in the optimization process, and k balances the relative cost of σ and Eq. 7. In particular, Horn & Schunck chose smoothness as a constraint, *i.e.*,

$$\sigma^2 = \sum_{i,j=1,2} \left(\frac{\partial u_i}{\partial x_j} \right)^2. \quad (10)$$

The idea of including constraints in the optimization process that determines the velocity field, over an area, is important in the context of the method to be discussed below. Note that the constraint in Eq. 9 need not be included in the optimization integral. Instead, it could be included as a feature of the optimization technique. See Murray & Buxton (1990).

2. Proposed methodology

A succession of images can represent anything from the motion of cars on a highway to the transport of a dye marker in water. We take the view that given successive image representations, there exists a transformation, or mapping, of the local image intensity data that takes one image to the next. In many cases, while the equation of motion of the imaged field may be known, the mapping taking one image to another may not be. Successive images combined with the equations of motion, however, often allow us to approximate the mapping.

The mapping of one image to the next can be developed by considering the Lagrangian displacement field $\xi(\mathbf{x}, t)$ of the image sequence. Specifically, if \mathbf{x} is the coordinate of a point on an image at some initial time t_0 , $\xi(\mathbf{x}, t)$ represents the coordinate of this point in a subsequent image recorded at a later time t . If we imagine the image sequence as the result of a continuous recording process, we can assign a Lagrangian *image-flow* velocity field, referred to as “optical flow” in the discussion and literature cited above, *i.e.*,

$$\mathbf{u}[\xi(\mathbf{x}, t), t] = \frac{d}{dt}\xi(\mathbf{x}, t) , \quad (11)$$

to the continuous displacement field $\xi(\mathbf{x}, t)$ that takes an initial point \mathbf{x} in the image recorded at time t_0 , to the point $\xi(\mathbf{x}, t)$ on the image recorded at time t . We recognize that, for the case where the images represent fluid flow, *e.g.*, successive images of a convected scalar, the image-flow velocity field, $\mathbf{u}(\mathbf{x}, t)$, may be quite different from the *fluid-flow* velocity field $\mathbf{u}_f(\mathbf{x}, t)$. The extent to which the former represents a good approximation for the latter is a separate issue that can only be addressed in the context of the details of the particular imaging process and the fluid-flow field.

In the proposed implementation, local series approximations for the displacement mapping are used in conjunction with an integral form of the equations of motion. A global nonlinear correlation (optimization) process is employed to estimate the image-flow velocity, vorticity, deformation rate, *etc.*, of the imaged data field. “Series,” in this discussion, will denote “Taylor series.”

In the context of fluid mechanics measurements, we will focus on images of continuous, passive, convected scalars, *e.g.*, dye markers, carried by a fluid. As will be illustrated using a pair of Voyager 2 images of Jupiter (Sec. 5), however, any marker in the flow can be used.

The method will be developed for three dimensions and can yield three-dimensional velocity fields. The method can also obtain two-dimensional velocity fields from images of two-dimensional flows. In a concession to the limitations of typical data acquisition systems today, however, the method will be applied here

to a two-dimensional flow and also to two-dimensional slices of three-dimensional flows. We note that in some cases, two-dimensional imaging devices can be used to obtain approximations to three-dimensional image data, *e.g.*, Dahm, *et al.* 1991. A short discussion of the implications of correlating two-dimensional slices of three-dimensional data is presented in Sec. 4.

2.1 Fluid displacement and equations of motion

To see how the image-flow velocity field can be calculated from three-dimensional image data sets, spaced in time, first consider a Lagrangian description of a flow being imaged. Figure 1 illustrates the motion of fluid particles within a volume, V . Fluid elements at \mathbf{x} , in a neighborhood V , at time t_0 , are convected to locations $\xi(\mathbf{x}, t)$ at a later time t . The displacement field, $\xi(\mathbf{x}, t)$, can be thought of as a transformation of the field \mathbf{x} , at time t_0 , to $\xi(\mathbf{x}, t)$. Given the image displacement field $\xi(\mathbf{x}, t)$, the image-flow velocity field is then given by Eq. 11.

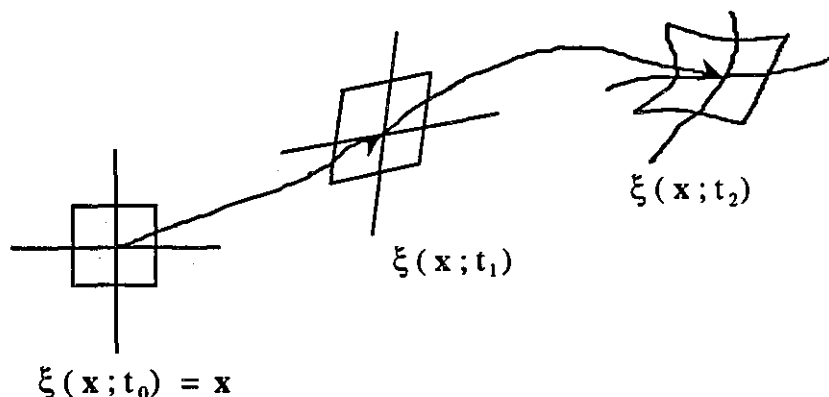


FIG. 1 Motion of a fluid volume.

Using this Lagrangian field, $\xi(\mathbf{x}, t)$, one could, in principle, integrate the equation of motion of the imaged scalar, *i.e.*,

$$\frac{\partial c}{\partial t} + \mathbf{u} \cdot \nabla c = \mathcal{D} \nabla^2 c, \quad (12)$$

to obtain

$$c_1[\xi(\mathbf{x}, t_1)] - c_0[\xi(\mathbf{x}, t_0)] - \mathcal{D} \int_{t_0}^{t_1} \nabla^2 c[\xi(\mathbf{x}, \tau), \tau] d\tau = 0, \quad (13)$$

where

$$c_0(\mathbf{x}) \equiv c(\mathbf{x}, t_0) \quad \text{and} \quad c_1(\mathbf{x}) \equiv c(\mathbf{x}, t_1) \quad (14)$$

represent the $c(\mathbf{x}, t)$ -field at times t_0 and t_1 , respectively, and \mathcal{D} is the appropriate diffusion coefficient.

In the first two examples, the motion of food coloring in glycerine (Sec. 3) and dilute fluorescein in water (Sec. 4), are examined. In these flows, the diffusion of the dye markers, in the time interval between successive images, is relatively small and may be neglected, *i.e.*,

$$\frac{(t_1 - t_0) \mathcal{D}}{\ell^2} \ll 1, \quad (15)$$

where, $t_1 - t_0 = 0.1$ s is the time between images, $\ell = 50$ to $80 \mu\text{m}$ is the imaging resolution, and the diffusion coefficients are no larger than $\mathcal{D} = 10^{-9} \text{m}^2/\text{s}$. In addition, we note that the Schmidt number is large in both flows, *i.e.*,

$$S_c \equiv \nu/\mathcal{D} > 10^3, \quad (16)$$

where ν is the kinematic viscosity. In the first example of the dye marker in glycerine, the fluid flow is two-dimensional, as is the image, and the image-flow velocity field, $\mathbf{u}(\mathbf{x}, t)$, is a good representation of the fluid-flow velocity field, $\mathbf{u}_f(\mathbf{x}, t)$. In the second example, both the flow velocity and the imaged scalar field are three-dimensional, while the image is two-dimensional. As we will discuss, the image-flow field need not necessarily represent the flow velocity field, in that case. In the third example, the motion of the imaged quantity in the Jovian atmosphere (Sec. 5) does not follow any simple equation of motion. In that example, the derived image-flow velocity field can be expected to be an even poorer representation of the fluid-flow velocity field.

In cases where the diffusion of the imaged scalar can be ignored, Eq. 13 becomes

$$c_1[\xi(\mathbf{x}, t_1)] - c_0[\xi(\mathbf{x}, t_0)] = 0. \quad (17)$$

Equation 17 represents a significant simplification over Eq. 12, its differential counterpart. It contains no spatial, or temporal, derivatives and suffers few of the drawbacks associated with the gradient methods discussed earlier (Sec. 1.2).

Using the integral equation of motion (Eq. 17) in place of the differential equation of motion (Eq. 7) in the optimization (Eq. 9), and generalizing the optimization to three dimensions then yields an expression for determining $\xi(\mathbf{x}, t_0)$ and $\xi(\mathbf{x}, t_1)$, *i.e.*,

$$\min_{\xi(\mathbf{x}, t_0), \xi(\mathbf{x}, t_1)} \int_V \left(\left\{ c_1[\xi(\mathbf{x}, t_1)] - c_0[\xi(\mathbf{x}, t_0)] \right\}^2 + k \sigma^2 \right) d^3\mathbf{x}. \quad (18)$$

In the spirit of the correlation methods discussed in Sec. 1.1, where the type of motion within the correlation volume is limited to translation alone, the present method restricts $\xi(\mathbf{x}, t_0)$ and $\xi(\mathbf{x}, t_1)$ to the first few terms of a series approximation for $\xi(\mathbf{x}, t)$. While many representations of the displacement field could be employed, a (Taylor) series representation is used because the first two orders in the series expansion correspond to physical fluid mechanical quantities, *i.e.*, the velocity vector and the velocity gradient tensor. More importantly, the series approximation has the additional benefit of enforcing smoothness in the displacement and displacement gradient fields within a correlation volume.

2.2 Displacement field and kinematic quantities

In the case of fluid-flow images, the quantity $\xi(\mathbf{x}, t)$ is a complicated nonlinear function of the imaging process, the nonlinear convection dynamics, and \mathbf{x} . Local estimates of this function can be made by Taylor series, expanding $\xi(\mathbf{x}, t)$ in space, at some time t , in an image correlation volume, V . This yields,

$$\xi(\mathbf{x}, t) = \xi(\mathbf{x}_c; t) + (\mathbf{x} - \mathbf{x}_c) \cdot \nabla \xi(\mathbf{x}_c; t) + \frac{1}{2!} [(\mathbf{x} - \mathbf{x}_c) \cdot \nabla]^2 \xi(\mathbf{x}_c; t) + \dots \quad (19)$$

In this expression, \mathbf{x}_c denotes the center of the image correlation volume, V , at time t_0 , and $\nabla \xi(\mathbf{x}_c; t)$ denotes the gradient of $\xi(\mathbf{x}, t)$ with respect to \mathbf{x} , evaluated at \mathbf{x}_c . Figure 2 plots the number of parameters used in the optimization process as a function of the order used in the series expansion, for two and three dimensions. Figure 3 illustrates the effect of the various orders of the expansion on a two-dimensional square "volume."

Using a finite difference approximation in time for the velocity, Eq. 11, and the series representation, Eq. 19, evaluated at times t_0 and t_1 , yields an estimate for the velocity within the correlation volume, *i.e.*,

$$\mathbf{u}[\xi(\mathbf{x}; t), t] \simeq \frac{\xi(\mathbf{x}; t_1) - \xi(\mathbf{x}; t_0)}{t_1 - t_0} \quad (20)$$

where $t_0 \leq t \leq t_1$. Similarly, taking the spatial gradient of Eq. 20 yields an expression for the velocity gradient tensor within the correlation volume, *i.e.*,

$$\nabla \mathbf{u}[\xi(\mathbf{x}; t), t] \equiv \frac{\partial}{\partial \mathbf{x}} \mathbf{u}[\xi(\mathbf{x}; t), t] \simeq \frac{\nabla \xi(\mathbf{x}; t_1) - \nabla \xi(\mathbf{x}; t_0)}{t_1 - t_0} \quad (21)$$

Vorticity, divergence, and strain rate can then be obtained from the components of the estimated velocity gradient tensor, Eq. 21.

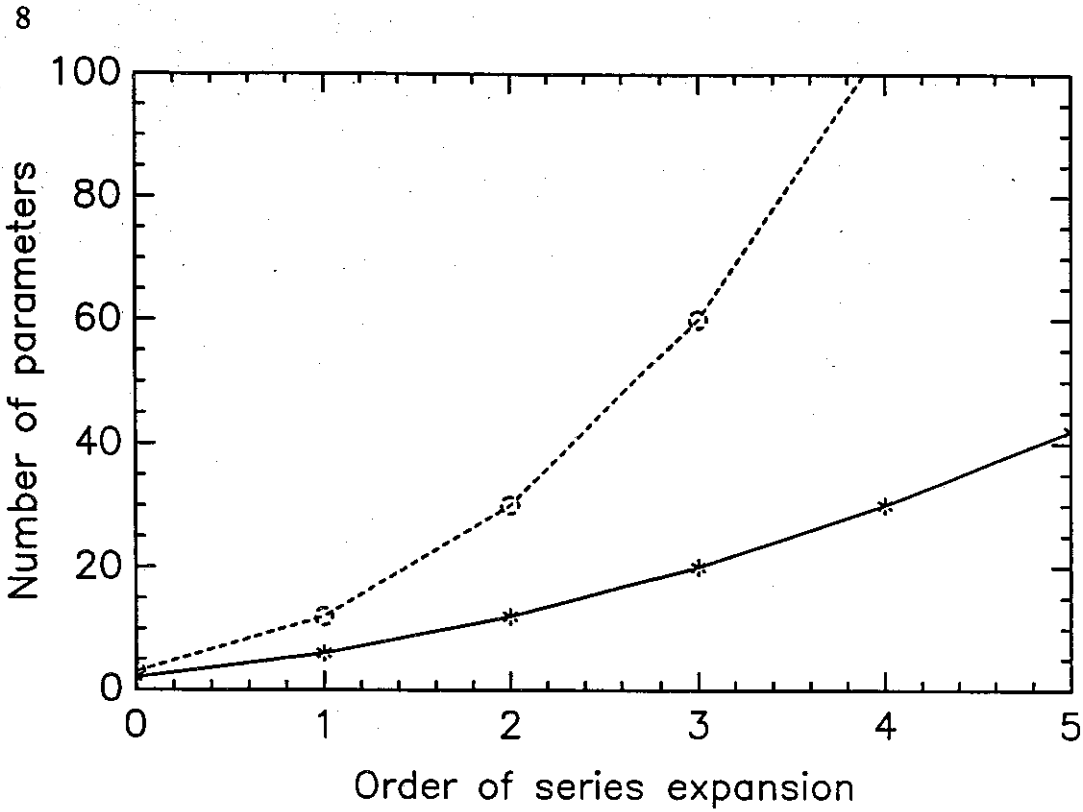


FIG. 2 This plot shows the rapid increase in the number of parameters used in the optimization procedure with increasing order of the series expansion. “*” is for a 2-D expansion and “o” for 3-D.

There is some freedom in choosing the coordinate transformation at the initial time t_0 , $\xi(\mathbf{x}, t_0)$. Our choice is to have the coordinate description at the initial time t_0 correspond with the local Eulerian coordinates at that time, *i.e.*,

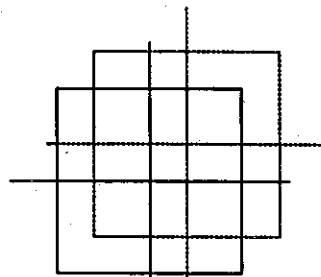
$$\xi(\mathbf{x}, t_0) = \mathbf{x} . \quad (22)$$

In terms of the series expansion, Eq. 19, this means that

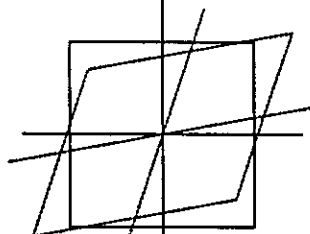
$$\nabla \xi(\mathbf{x}_c; t_0) \equiv \mathbf{I} , \quad (23)$$

where \mathbf{I} is the identity tensor, and all other higher order derivative terms are identically zero.

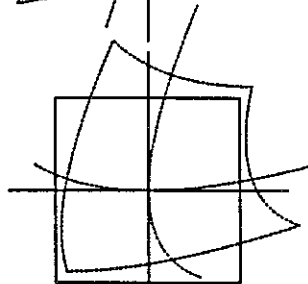
Translation (no deformation)



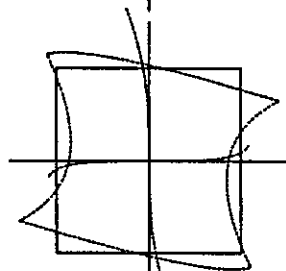
Linear deformation



Quadratic deformation



Cubic deformation



Combined translation and deformation

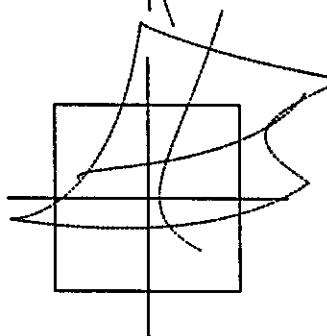


FIG. 3 The effect if translation and various orders of deformation on a two-dimensional square "volume." See Sec. 2.2.

2.3 Seeking a global solution

A solution for the coefficients of the series expansion, *i.e.*, $\xi(\mathbf{x}_c; t)$, $\nabla\xi(\mathbf{x}_c; t)$, *etc.*, can be obtained in a neighborhood around \mathbf{x}_c using the expansions for $\xi(\mathbf{x}, t_0)$ and $\xi(\mathbf{x}, t)$ from Sec.2.2. The unknown coefficients of the series expansion, $\xi(\mathbf{x}_c; t)$, $\nabla\xi(\mathbf{x}_c; t)$, *etc.*, are treated as parameters in an optimization process. To minimize the difference between two data sets (images), in a least squares sense, for a single correlation volume, we use the optimization, Eq.18, in conjunction with the series approximations developed in Sec.2.2, *i.e.*,

$$\min_{\xi(\mathbf{x}_c; t_1), \nabla\xi(\mathbf{x}_c; t_1), \dots} \int_V \left(\left\{ c_1 [\xi(\mathbf{x}_c; t_1) + (\mathbf{x} - \mathbf{x}_c) \cdot \nabla\xi(\mathbf{x}_c; t_1) + \dots] - c_0[\mathbf{x}] \right\}^2 + k\sigma^2 \right) d^3\mathbf{x} . \quad (24)$$

The optimization implied in Eq.24, combines many of the best features of correlation methods and gradient methods, while eliminating many of the deficiencies. Specifically, this optimization method has high immunity to noise, uses the equations of motion, can incorporate constraints, requires no differentiation to calculate the displacement field, and can capture displacement gradients within a correlation volume.

In principle, a single correlation volume covering the entire image and a series approximation of a high enough order can be used to capture the entire image displacement field. In practice, however, employing a series approximation beyond the third order (cubic) term is impractical because of the rapid increase in the number of parameters in the optimization process with increasing order (see Fig. 2), and the associated increase in the computational time and complexity. In the present calculations, when the quadratic term is not sufficient to capture the image deformation over the entire flow field using a single volume, as is usually the case, several series expansions residing in smaller, adjacent, correlation volumes are used in place of the single large volume.

To construct a global optimization using a number of local series expansions, we require that neighboring correlation volumes, with independent series expansions, must yield consistent results. In the present method, we use the expansion for the displacement field about one correlation volume to estimate those of its neighbors. The displacement field of these neighbors is also estimated in terms of their own series expansions. The root-mean-square difference between displacements estimated by neighboring correlation volumes is applied as a constraint cost function. Since it is necessary to refer to a number of series expansions, it is useful to define the

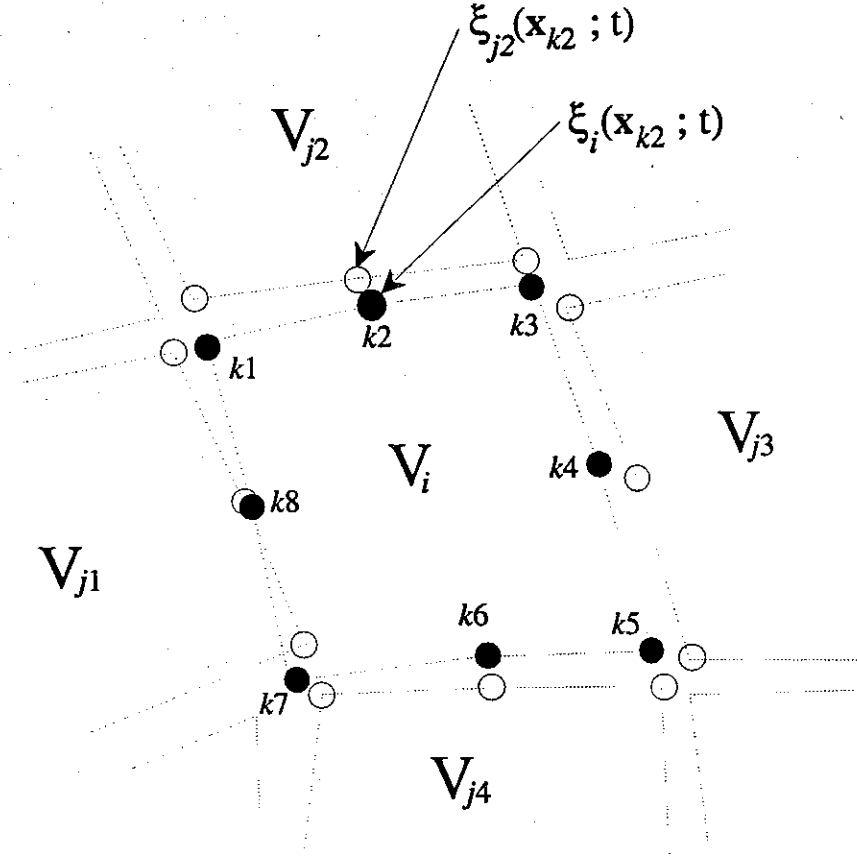


FIG. 4 The $k_1 - k_8$ solid circles denote the points in V_i used by the constraint cost function σ_i . The empty circles denote their counterparts estimated by the neighbors $V_{j1} - V_{j4}$.

taylor series for $\xi(\mathbf{x}, t)$ in a neighborhood V_i centered about \mathbf{x}_{c_i} , as

$$\xi_i(\mathbf{x}; t) \equiv \xi(\mathbf{x}_{c_i}; t) + (\mathbf{x} - \mathbf{x}_{c_i}) \cdot \nabla \xi(\mathbf{x}_{c_i}; t) + \frac{1}{2!} [(\mathbf{x} - \mathbf{x}_{c_i}) \cdot \nabla]^2 \xi(\mathbf{x}_{c_i}; t) + \dots \quad (25)$$

When series expansions about multiple points are then employed, the minimization, Eq. 24, is modified, *i.e.*,

$$\min_{\xi(\mathbf{x}_{c_i}; t_1), \nabla \xi(\mathbf{x}_{c_i}; t_1), \dots} \int_{V_i} \left(\left\{ c_1 [\xi_i(\mathbf{x}; t_1)] - c_0[\mathbf{x}] \right\}^2 + k \sigma_i^2 \right) d^3 \mathbf{x}, \forall i. \quad (26)$$

This minimization is performed within all the V_i , simultaneously, and the square of the constraint cost function,

$$\sigma_i^2 = \sum_j \sum_k |\xi_i(\mathbf{x}_k; t) - \xi_j(\mathbf{x}_k; t)|^2 \quad (27)$$

is applied to provide global continuity of the solution. ξ_j denotes the series expansion about the “ j ” neighbors of V_i , and \mathbf{x}_k denotes the “ k ” points of comparison between the solutions ξ_i and ξ_j . See Fig. 4. In the present method, eight points about each correlation volume are used for comparison, three with each of four neighbors. These eight points are sufficient to define the series expansion coefficients of the correlation volume, up to quadratic order.

The present implementation of the method can solve Eq. 26 for two-dimensional flow up to the cubic term in the local series expansions, but the series is usually truncated at quadratic order. The optimization of Eq. 24 is accomplished using a multidimensional minimization process, with image data between pixels estimated using bilinear interpolation. See for example Press, *et al.* (1988).

2.4 Minimization parameters in two dimensions

Typical CCD imaging technologies today are limited to two-dimensional (spatial) data. This is not a problem if the flow being imaged is also two-dimensional. This section describes how the method is applied in two dimensions. First, we develop the terms of the series expansion, Eq. 19, for two-dimensional flow. With the two-dimensional vector

$$\begin{bmatrix} \delta_1 \\ \delta_2 \end{bmatrix} \equiv \mathbf{x} - \mathbf{x}_c \quad , \quad (28)$$

as the position, \mathbf{x} , relative to the center of the correlation volume, \mathbf{x}_c , the terms of the series expansion at a time t_1 appear as a constant term,

$$\xi(\mathbf{x}_c; t_1) = \begin{bmatrix} \alpha_1 \\ \alpha_0 \end{bmatrix} \quad , \quad (29)$$

where the α_i are the vector coordinates of the center of the correlation volume at the time t_1 , *i.e.*,

$$\alpha_i \equiv \xi_i(\mathbf{x}_c; t_1) \quad , \quad (30)$$

a linear term,

$$(\mathbf{x} - \mathbf{x}_c) \cdot \nabla \xi(\mathbf{x}_c; t_1) = \begin{bmatrix} \alpha_{1,1} & \alpha_{1,2} \\ \alpha_{2,1} & \alpha_{2,2} \end{bmatrix} \cdot \begin{bmatrix} \delta_1 \\ \delta_2 \end{bmatrix} \quad , \quad (31)$$

where the $\alpha_{i,j}$ represent the first order deformations and rotations of the image field within the correlation volume, *i.e.*,

$$\alpha_{i,j} \equiv \frac{\partial \xi_i(\mathbf{x}_c; t_1)}{\partial x_j} \quad , \quad (32)$$

a quadratic term,

$$\frac{1}{2!} [(\mathbf{x} - \mathbf{x}_c) \cdot \nabla]^2 \xi(\mathbf{x}_c; t_1) = \begin{bmatrix} \alpha_{1,11} & \alpha_{1,12} & \alpha_{1,22} \\ \alpha_{2,11} & \alpha_{2,12} & \alpha_{2,22} \end{bmatrix} \cdot \begin{bmatrix} \delta_1^2 \\ \delta_1 \delta_2 \\ \delta_2^2 \end{bmatrix} \quad , \quad (33)$$

where

$$\alpha_{i,jk} \equiv \frac{1}{2!} \binom{2}{j+k-2} \frac{\partial^2 \xi_i(\mathbf{x}_c; t_1)}{\partial x_j \partial x_k}, \quad (34)$$

a cubic term,

$$\frac{1}{3!} [(\mathbf{x} - \mathbf{x}_c) \cdot \nabla]^3 \xi(\mathbf{x}_c; t_1) = \begin{bmatrix} \alpha_{1,111} & \alpha_{1,112} & \alpha_{1,122} & \alpha_{1,222} \\ \alpha_{2,111} & \alpha_{2,112} & \alpha_{2,122} & \alpha_{2,222} \end{bmatrix} \cdot \begin{bmatrix} \delta_1^3 \\ \delta_1^2 \delta_2 \\ \delta_1 \delta_2^2 \\ \delta_2^3 \end{bmatrix}, \quad (35)$$

with

$$\alpha_{i,jkl} \equiv \frac{1}{3!} \binom{3}{i+j+k-3} \frac{\partial^3 \xi_i(\mathbf{x}_c; t_1)}{\partial x_j \partial x_k \partial x_l}, \quad (36)$$

and so on for higher order terms. The $\alpha_{i,jk}$ and $\alpha_{i,jkl}$ are, respectively, related to the second and third derivatives of the displacement field within the correlation volume, *i.e.*, by Eqs. 34 and 36.

The velocity and velocity gradient (Eqs. 20 and 21), can also be written in terms of the parameters of Eqs. 29 and 31 and the series expansions at times t_0 and t_1 , *i.e.*,

$$\mathbf{u}(\mathbf{x}_c, t) \equiv \begin{bmatrix} u \\ v \end{bmatrix} = \frac{1}{t_1 - t_0} \begin{bmatrix} \alpha_1 - x_c \\ \alpha_2 - y_c \end{bmatrix}, \quad (37)$$

where

$$\mathbf{x}_c = \begin{bmatrix} x_c \\ y_c \end{bmatrix} \quad (38)$$

and

$$\nabla \mathbf{u}(\mathbf{x}_c, t) \equiv \begin{bmatrix} \partial u / \partial x & \partial u / \partial y \\ \partial v / \partial x & \partial v / \partial y \end{bmatrix} = \frac{1}{t_1 - t_0} \begin{bmatrix} \alpha_{1,1} - 1 & \alpha_{1,2} \\ \alpha_{2,1} & \alpha_{2,2} - 1 \end{bmatrix}. \quad (39)$$

Alternatively, the velocity gradient can be written in terms of the in-plane vorticity and rate-of-strain tensor, *i.e.*,

$$\nabla \mathbf{u}(\mathbf{x}_c, t) = \begin{bmatrix} 0 & -\omega_z/2 \\ \omega_z/2 & 0 \end{bmatrix} + \begin{bmatrix} s_{xx} & s_{xy} \\ s_{xy} & s_{yy} \end{bmatrix}, \quad (40)$$

where ω_z is the vorticity, *i.e.*,

$$\omega_z = \frac{\alpha_{2,1} - \alpha_{1,2}}{t_1 - t_0}, \quad (41)$$

and s_{xx} , s_{yy} , and s_{xy} , are the components of the rate-of-strain tensor, *i.e.*,

$$s_{xx} = \frac{\alpha_{1,1} - 1}{t_1 - t_0}, \quad (42)$$

$$s_{yy} = \frac{\alpha_{2,2} - 1}{t_1 - t_0}, \quad (43)$$

and

$$s_{xy} = \frac{1}{2} \frac{\alpha_{1,2} + \alpha_{2,1}}{t_1 - t_0}. \quad (44)$$

An interesting quantity to consider is the second invariant of the rate-of-strain tensor (see Cantwell 1992, for example), *i.e.*,

$$-2q_s \equiv s_{xx}^2 + 2s_{xy}^2 + s_{yy}^2. \quad (45)$$

3. Couette flow between concentric cylinders

An apparatus to generate a Couette flow between concentric cylinders was fabricated for the purpose of testing the method. The cylinders were made from 248 mm lengths of stock Plexiglas tubing. The inner and outer radii of the annular region between the cylinders were nominally 25.2 mm and 40.9 mm. The cylinders were from stock Plexiglas tubing, so the uncertainties in the radii were ± 1 mm. The outer cylinder was rotated with a rotation rate of 1.1 rad/s, with the inner cylinder stationary. In this example, employing a dye marker in glycerine, the fluid flow is nominally two-dimensional and the marker follows the flow. Hence, the image-flow velocity field, \mathbf{u} , can be accepted as a good representation of the fluid-flow velocity field, \mathbf{u}_f .

Images were recorded using a Texas Instruments Multicam MC-1134GN Multi-Mode B/W Camera. The data were stored digitally using an in-house multiple frame grabber (12-bit A/D), designed by Dan Lang and Paul Dimotakis of GALCIT, set to record up to 28 of the 1134×468 pixel gray level images from the camera, spaced by 100 msec (adjustable between 33 and 267 msec). Because the horizontal and vertical spacing of the pixels were not equal on this CCD, grid spacings and image correlation volumes with a ratio of 1:1.74 (vertical:horizontal pixels) were used to yield a uniform spacing of the data in the real image plane. Flow visualization was performed by randomly distributing red food coloring (dye) on the surface of the fluid. To provide backlighting for the dye marker, the fluid beneath the surface contained a translucent white suspension of $3 \mu\text{m}$ aluminum oxide (Al_2O_3) particles in glycerine. When illuminated from the side, this provided nearly uniform white backlighting for the dye being imaged on the surface. Because of the depth of field of the imaging and the high density and uniform distribution of the aluminum oxide, scattering from individual particles was not detectable in the video images.

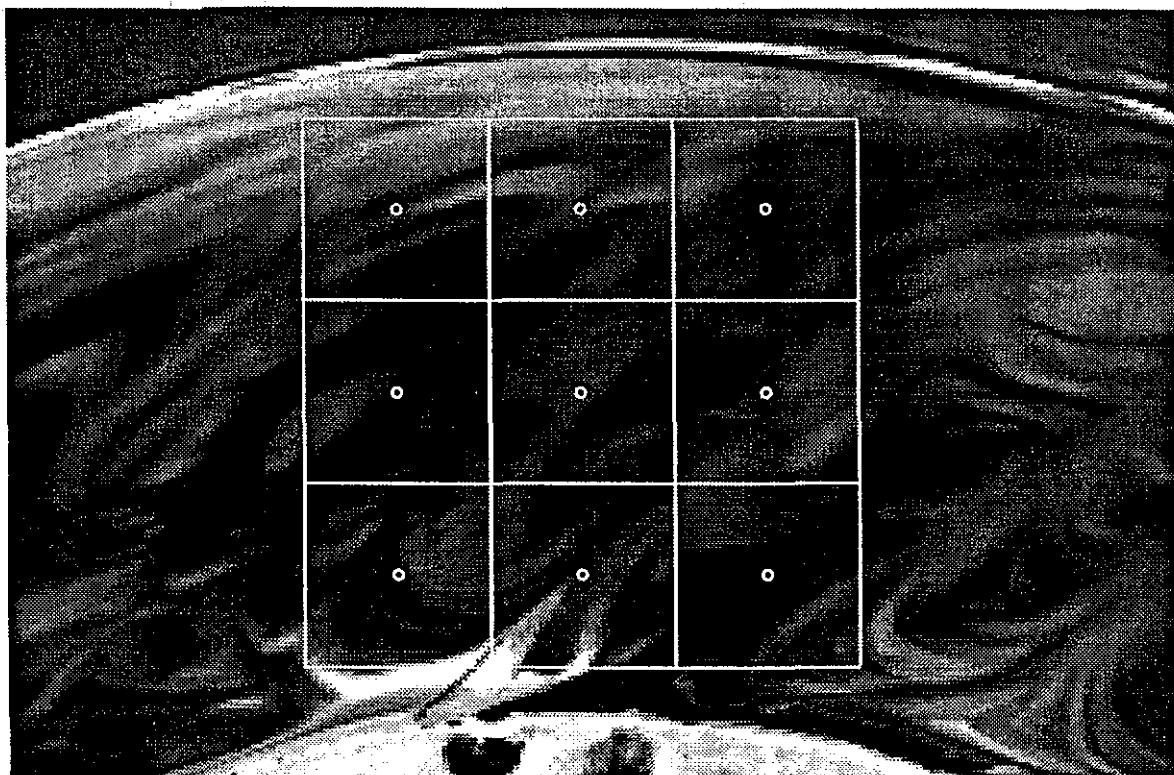


FIG. 5 Initial placement of series expansion neighborhoods. Each square denotes a control volume. The small circle at the center of each control volume denotes the center, or control point, of a series expansion.

In the present investigations, only the outer cylinder was rotated, hence the velocity field can be written as (*e.g.*, Schlichting 1979),

$$\frac{u_r(r, \theta)}{\Omega_o r_o} = 0 \quad \text{and} \quad \frac{u_\theta(r, \theta)}{\Omega_o r_o} = \frac{r/r_i - r_i/r}{r_o/r_i - r_i/r_o}, \quad (46)$$

where r , θ , u_r , and u_θ are the radial and angular positions and velocities, respectively, Ω_o is the rotation rate of the outer cylinder, and r_i and r_o are the inner and outer radii of the cylinders. In this flow, the divergence is zero, *i.e.*,

$$\nabla \cdot \mathbf{u} = 0, \quad (47)$$

and the vorticity is uniform, *i.e.*,

$$\omega_z(r, \theta) \equiv \mathbf{e}_z \cdot \nabla \times \mathbf{u}(r, \theta) = \frac{2 \Omega_o}{1 - (r_i/r_o)^2}. \quad (48)$$

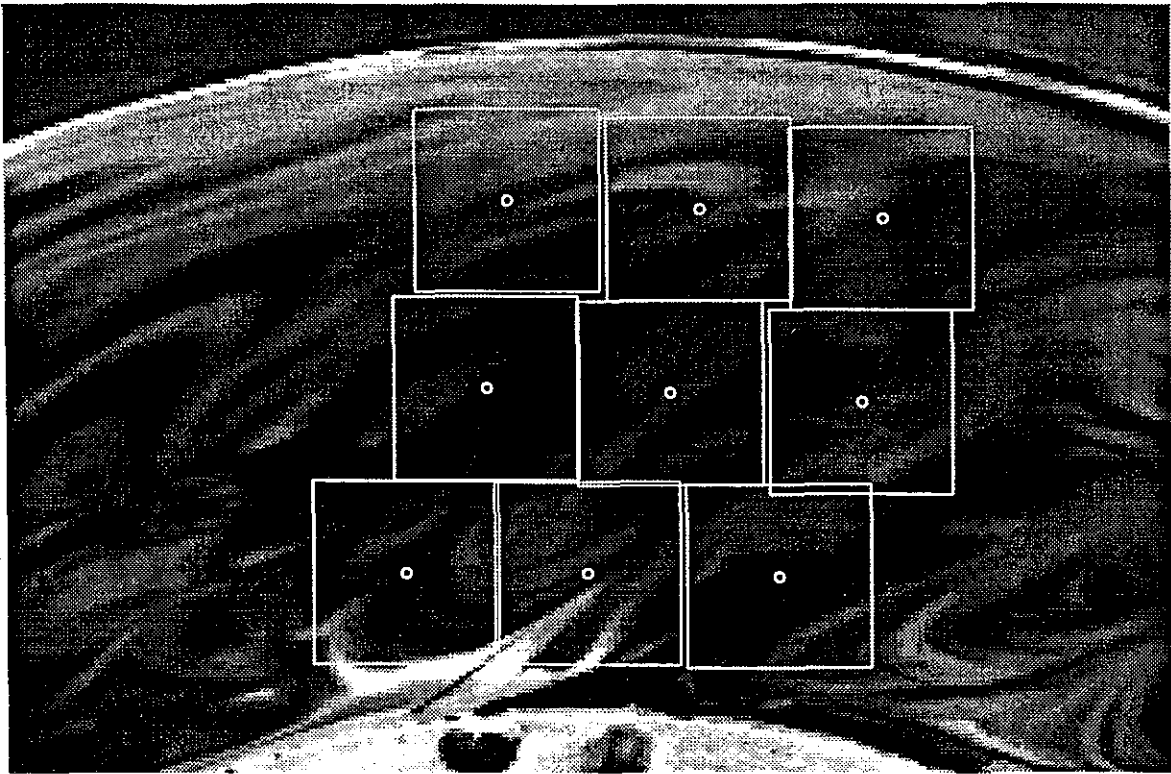


FIG. 6 Displacement of series neighborhoods, 100ms later, allowing only translation.

For this simple test case, nine correlation volumes spaced by 45 pixels vertically and 78.3 pixels horizontally, were used to capture the flow. The locations of the image correlation volumes at the initial time are depicted in Fig. 5. The results of the correlation process, allowing only displacement of the correlation volume (zeroth order series expansion) is shown in Fig. 6. Figure 7 demonstrates how the flow is captured when the correlation process is extended to include higher order terms in the series expansion. To quantify this improvement, the value of the minimization functional, not including the contribution of the constraints, is plotted in Fig. 8 as a function of the order of the series expansion. As can be seen, the greatest improvement is realized with the introduction of linear deformations in the correlation process.

The results using the correlation method are compared with the theoretical (analytical) two-dimensional values for the vorticity and divergence in Table 1. Since both the vorticity and the divergence are uniform in the analytical solution, only a single value is presented. The uncertainty in the theoretical vorticity is a result of the eccentricity of the cylinders used in the experiment. The uncertainties in the experimental values are one standard deviation. Because this flow has a nearly linear velocity profile, we saw only small changes in these estimates, beyond the linear order. Some of the "uncertainty" in the experimental results for the

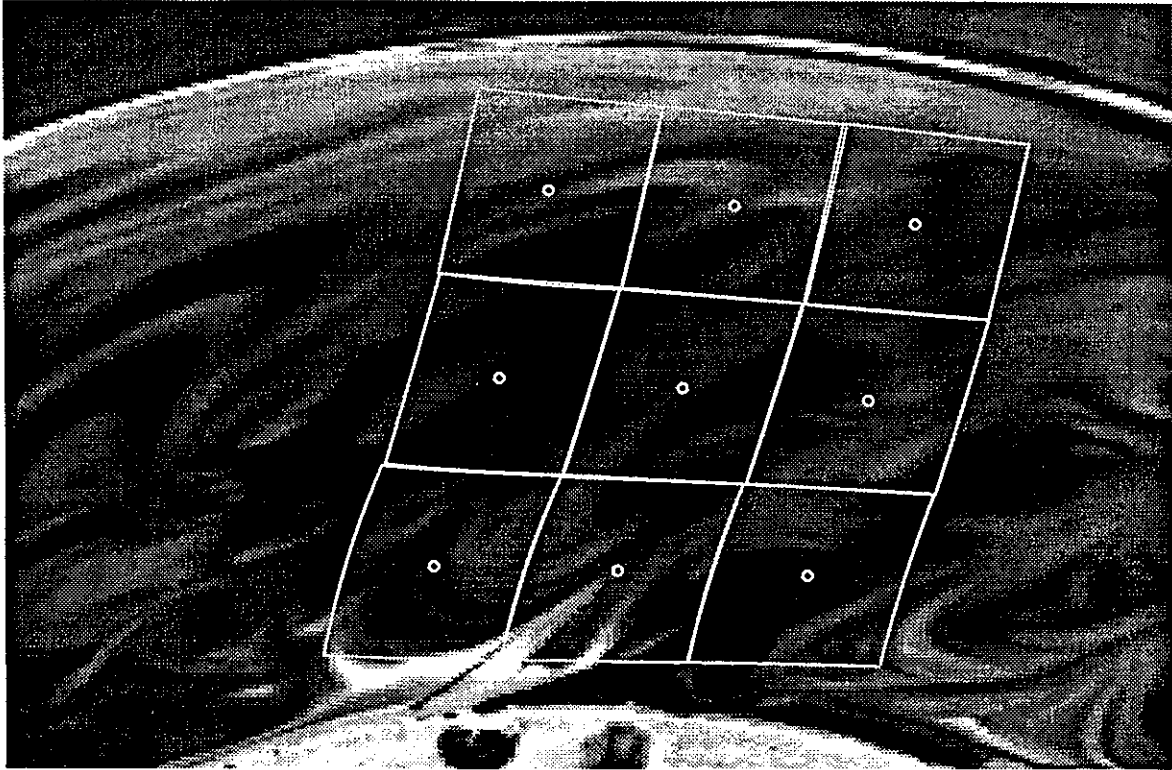


FIG. 7 Displacement of series neighborhoods estimated using higher order terms in the correlation process.

vorticity reflect the expected variations of the vorticity within the flow.

	$\omega_z [\text{sec}^{-1}]$	$\nabla \cdot \mathbf{u} [\text{sec}^{-1}]$
Theoretical:	-3.6 ± 0.1	0.0
Experimental:	-3.6 ± 0.3	-0.1 ± 0.1

TABLE 1. Comparison of theoretical and experimental vorticity and divergence.

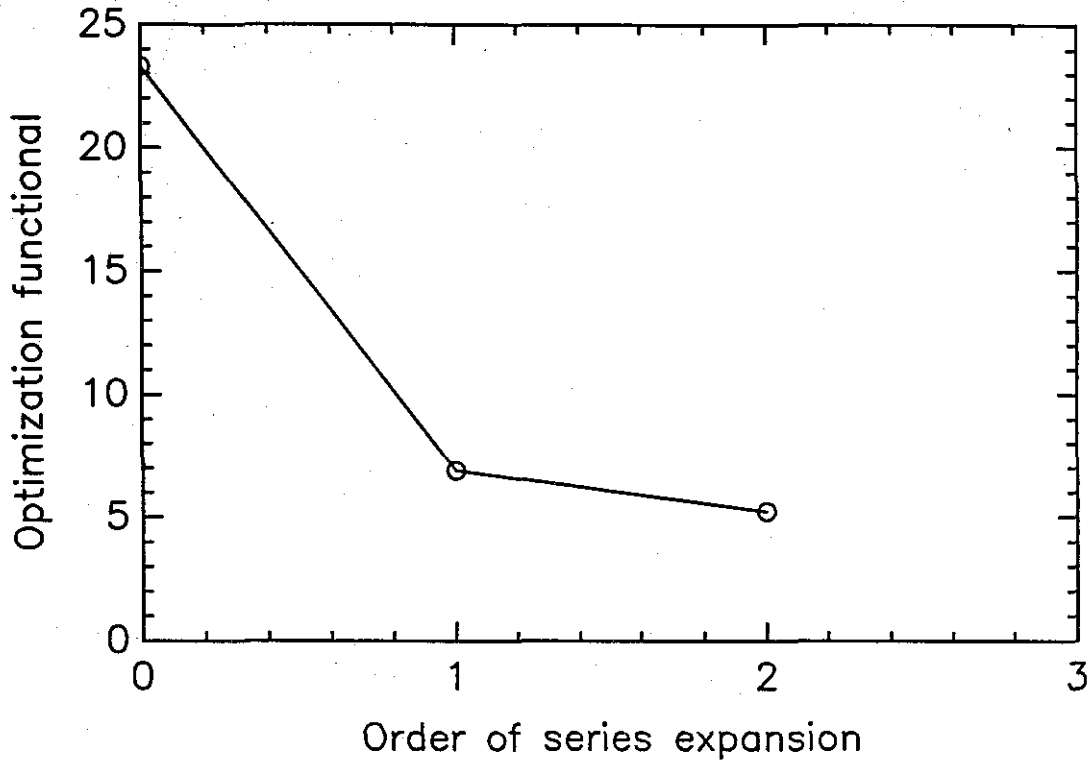


FIG. 8 Difference between Couette flow images under the mapping, quantified by the value of the optimization functional (arbitrary units), as a function of the number of terms in the two-dimensional series expansion.

4. Cylinder wake flow. Two-dimensional slices of three-dimensional data

In this section, we present the results of applying the two-dimensional correlations to two-dimensional slices of a three-dimensional flow in the wake of an impulsively started circular cylinder. Here, the cylinder is 1.75 cm in diameter and 45.5 cm long. It is drawn through a distribution of fluorescein dye in water at a speed of 1.27 cm/s. The Reynolds number in this case is,

$$Re \equiv \frac{U d}{\nu} \approx 220 , \quad (49)$$

where U is the cylinder speed, d is the cylinder diameter, and ν is the kinematic viscosity.

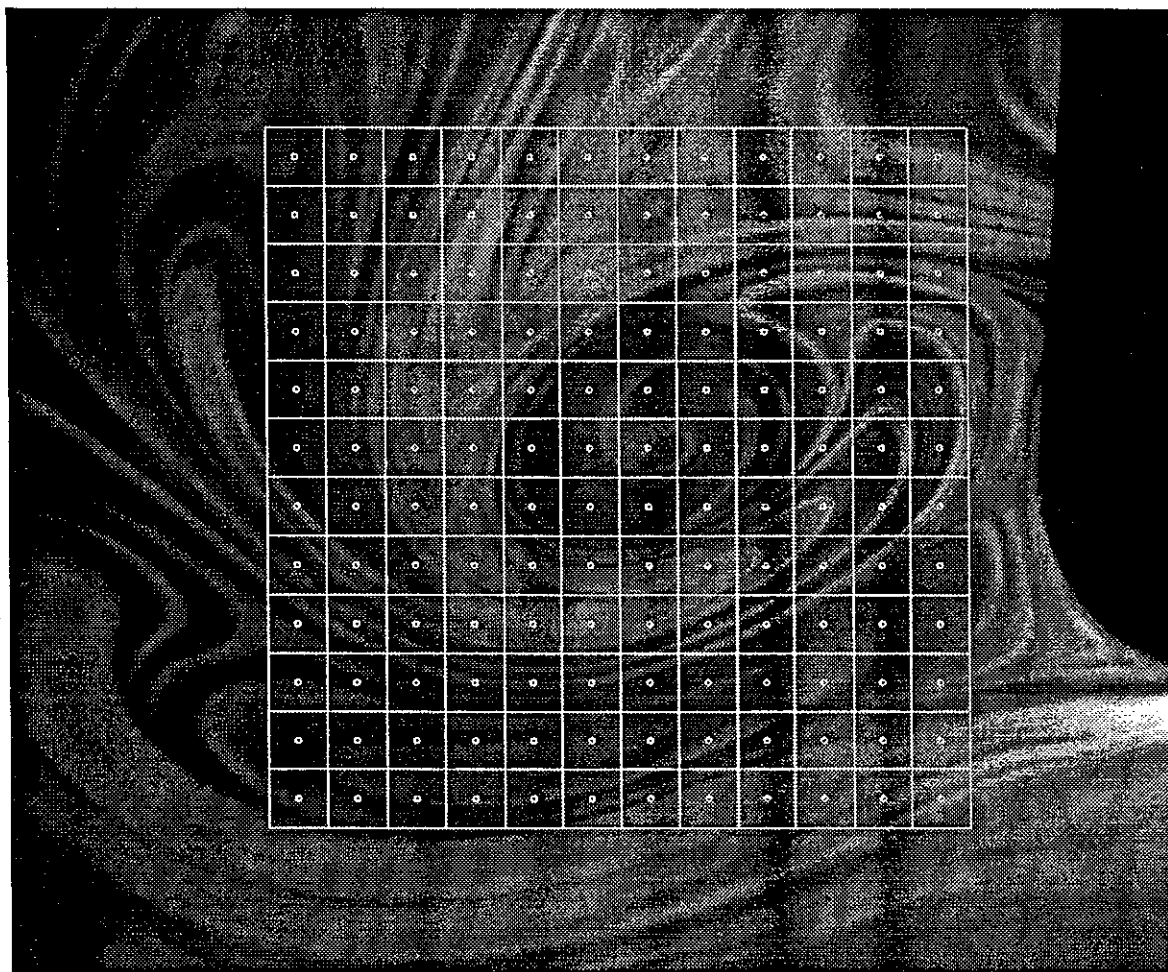


FIG. 9 Initial placement of series expansion neighborhoods. Each square denotes a control volume. The small circle at the center of each control volume denotes the center, or control point, of a series expansion.

The CCD camera and data acquisition system are the same as for the Couette flow test case (Sec. 3). Laser sheet illumination is provided by a Continuum model YG661-10 frequency-doubled YAG laser. The laser was operated at 532 nm, 300 mJ, 5 ns pulses width, at a rate of 10 Hz. The flow here is three-dimensional in both the velocity field and scalar distribution.

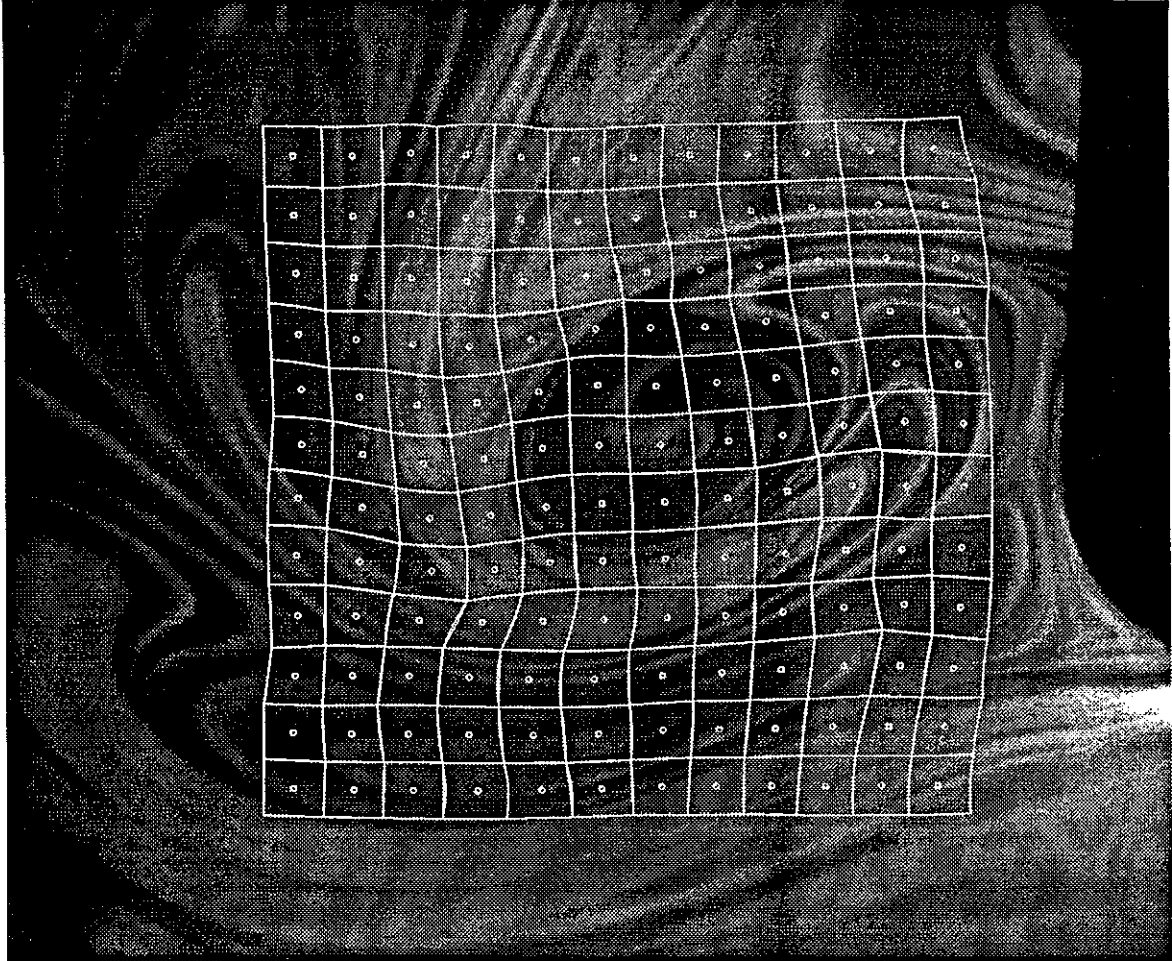


FIG. 10 Displacement of grid after 100 ms, estimated using the nonlinear correlation process.

Figures 9 - 14 demonstrate the method on images of a vortical structure forming in the wake of the cylinder. These images were taken after the cylinder had traveled about 8 diameters. The image at the initial time is shown in Fig. 9, and 100 ms later, in Fig. 10. In this case, the series approximation used in the correlation process was expanded to quadratic order. Figure 11 shows the displacement of the centers of the correlation volumes.

The two-dimensional vorticity is displayed in Fig. 12. A large vortical region can be seen in the wake of the cylinder. The two-dimensional divergence, presented



FIG. 11 Displacement of centers of grid over 100 ms.

in Fig. 13, exposes the three-dimensionality in the flow. Figure 14 plots the second invariant of the rate-of-strain tensor. Note the region of strain (rate) that seems to follow the periphery of the large vortical structure. This could be a region of vorticity, from the previously shed vortical structure, that is being strained around the current one.

As a general observation, an important issue arises when imaging a two-dimensional (planar image) slice of a three-dimensional field of a continuous scalar, $c(\mathbf{x}, t)$, as in the previous example. An out-of-plane component of the fluid-flow velocity, \mathbf{u}_f , coupled with an out-of-plane component of the scalar gradient, $\nabla c(\mathbf{x}, t)$, will contribute to the in-plane image-flow velocity \mathbf{u} . In this case, the equation for the in-plane image flow can still be written as,

$$\frac{\partial c}{\partial t} + \mathbf{u} \cdot \frac{\partial c}{\partial \mathbf{x}} \equiv \frac{\partial c}{\partial t} + u \frac{\partial c}{\partial x} + v \frac{\partial c}{\partial y} = 0, \quad (50)$$

where we have assumed that the image irradiance $E(\mathbf{x}, t)$ is proportional to the two-dimensional slice of the scalar concentration, $c(\mathbf{x}, t)$, and where the in-plane image-

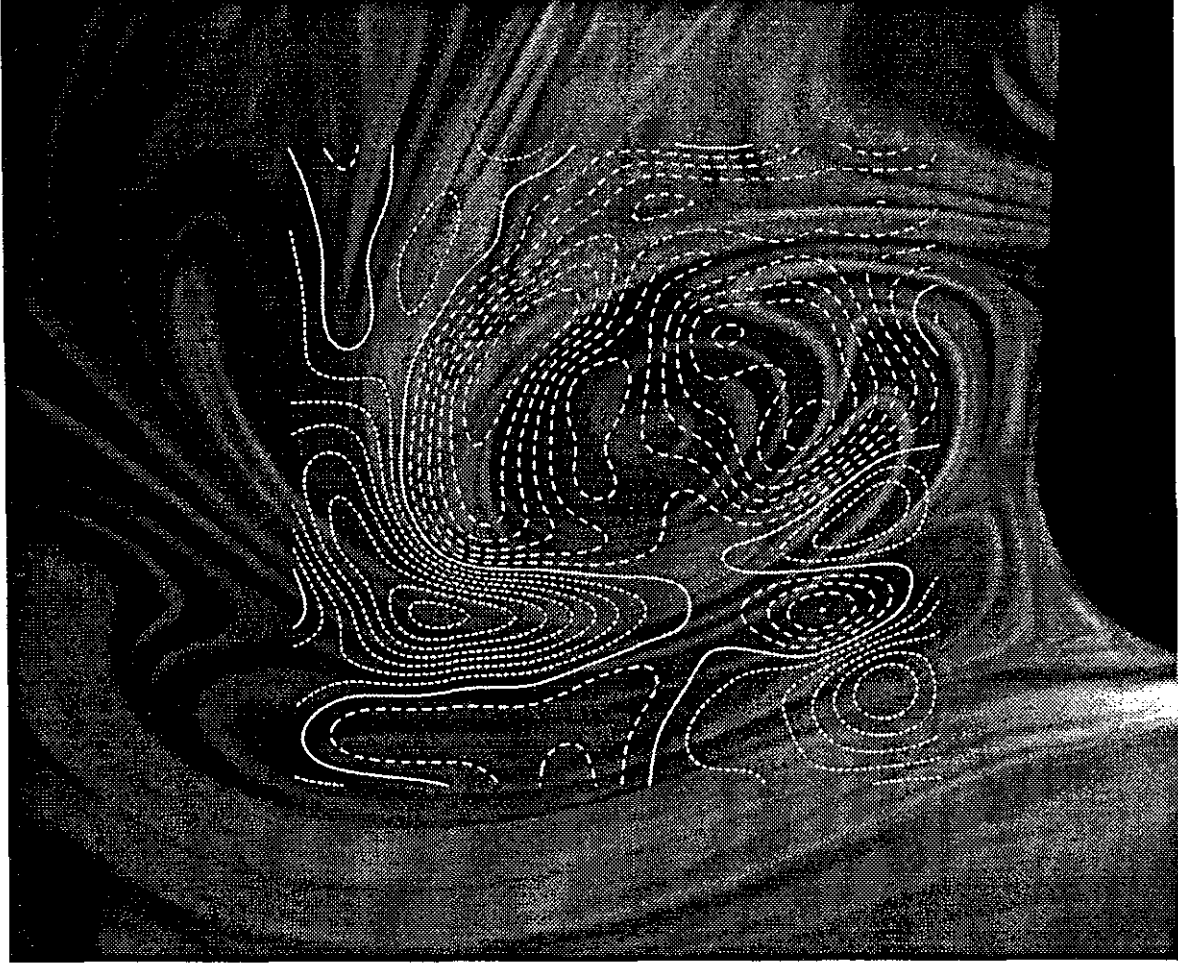


FIG. 12 Contours of constant plane-normal vorticity, $\nabla \times \mathbf{u} = \frac{\partial v}{\partial x} - \frac{\partial u}{\partial y}$. Solid contours denote zero-vorticity. Long dashes denote positive values and short dashes negative. Contours spaced by 0.5 s^{-1} .

flow velocity, $\mathbf{u} = (u, v) = d\xi/dt$ (Eq. 11), is the one derived from the minimization function, as described above.

Considering the transport of the three-dimensional iso-scalar surfaces (see Fig. 15), we find that the two-dimensional $\mathbf{u} = (u, v)$ in-plane image-flow velocity components are related to the three-dimensional $\mathbf{u}_f = (u_f, v_f, w_f)$ fluid-flow velocity and the three-dimensional scalar gradient components. In particular, we have,

$$\begin{aligned} u &= u_f + w_f \frac{\partial c}{\partial z} \frac{\partial c / \partial x}{(\partial c / \partial x)^2 + (\partial c / \partial y)^2} , \\ v &= v_f + w_f \frac{\partial c}{\partial z} \frac{\partial c / \partial y}{(\partial c / \partial x)^2 + (\partial c / \partial y)^2} . \end{aligned} \quad (51)$$

As can be seen, by substituting Eq. 51 in Eq. 50, these relations recover the three-dimensional transport equation for a conserved scalar field $c(\mathbf{x}, t)$, in the case of



FIG. 13 Contours of constant divergence, $\nabla \cdot \mathbf{u} = \frac{\partial u}{\partial x} + \frac{\partial v}{\partial y}$. As in Fig. 12, the contours are spaced by 0.5 s^{-1} .

negligible diffusion, *i.e.*,

$$\frac{\partial c}{\partial t} + \mathbf{u}_f \cdot \frac{\partial c}{\partial \mathbf{x}} \equiv \frac{\partial c}{\partial t} + u_f \frac{\partial c}{\partial x} + v_f \frac{\partial c}{\partial y} + w_f \frac{\partial c}{\partial z} = 0 .$$

These results provide us with the criteria for when the in-plane image-flow velocity can be regarded as a good approximation to the in-plane fluid-flow velocity. In particular, we will have,

$$u \simeq u_f , \quad \text{if} \quad \frac{u_f}{w_f} \gg \left(\frac{\partial c / \partial z}{(\partial c / \partial x)^2 + (\partial c / \partial y)^2} \right) \frac{\partial c}{\partial x} , \quad (52a)$$

and

$$v \simeq v_f , \quad \text{if} \quad \frac{v_f}{w_f} \gg \left(\frac{\partial c / \partial z}{(\partial c / \partial x)^2 + (\partial c / \partial y)^2} \right) \frac{\partial c}{\partial y} . \quad (52b)$$



FIG. 14 Contours of constant second invariant of the rate-of-strain tensor (Eq. 45), $q_s = -\frac{1}{2} \left[\left(\frac{\partial u}{\partial x} \right)^2 + \left(\frac{\partial v}{\partial y} \right)^2 - \frac{1}{2} \left(\frac{\partial u}{\partial y} + \frac{\partial v}{\partial x} \right)^2 \right]$. Contours spaced by 0.5 s^{-2} .

We can see that if w_f is small, or if $\partial c / \partial z$ is small, or both, by the measure in Eq. 52, then the in-plane image-flow velocity field can be accepted as a good representation of the in-plane fluid-flow velocity field.

Finally, since this method estimates the in-plane image-flow velocity \mathbf{u} , and not the fluid-flow velocity \mathbf{u}_f , its application to two-dimensional image slices of three-dimensional scalar field data is identical to its application to two-dimensional scalar data.

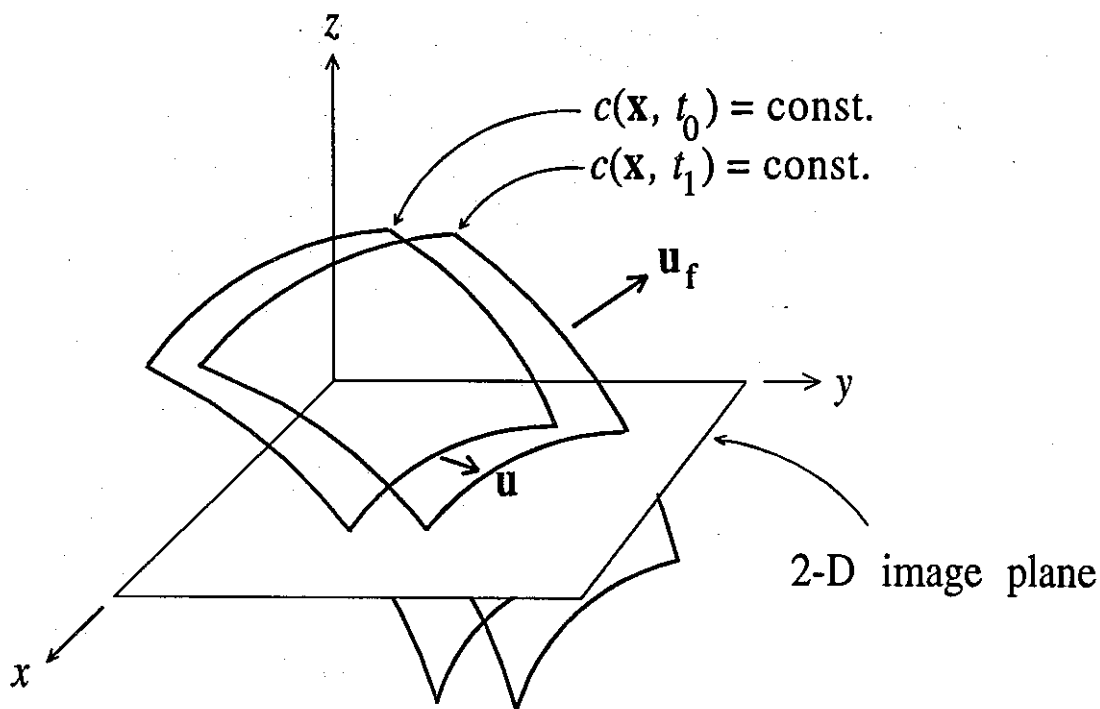


FIG. 15 Two-dimensional slices of a three-dimensional scalar field $c(\mathbf{x}, t)$. \mathbf{u}_f indicates the 3-D fluid-flow velocity and \mathbf{u} is the resulting two-dimensional in-plane image-flow velocity.

5. Voyager 2 images of Jupiter

The method is also illustrated on a pair of the images of the atmospheric dynamics of Jupiter taken by Voyager 2. These images were taken from the "Voyager Time-Lapse, Cylindrical-Projection Jupiter Mosaics," by Avis & Collins (1983). 640×350 pixel subimages of rotations 349 and 350 were used in the correlation process. The subimage spans 168° to 97° longitude and 0° to -46° latitude (the equator is at the top of the image). The subimage from rotation 349 is shown in Fig. 16, with an overlay of the initial placement of the correlation volume neighborhoods. The vertical line on the left is a reference line which is to be deformed using the mean zonal velocities of Jupiter from Limaye (1985). Figure 17 shows the same region, one rotation later, with the associated grid deformed by the nonlinear correlation method. On the left is the reference line from Fig. 16, carried by the mean zonal flow. The displacement of the centers of the correlation volumes is shown in Fig. 18.

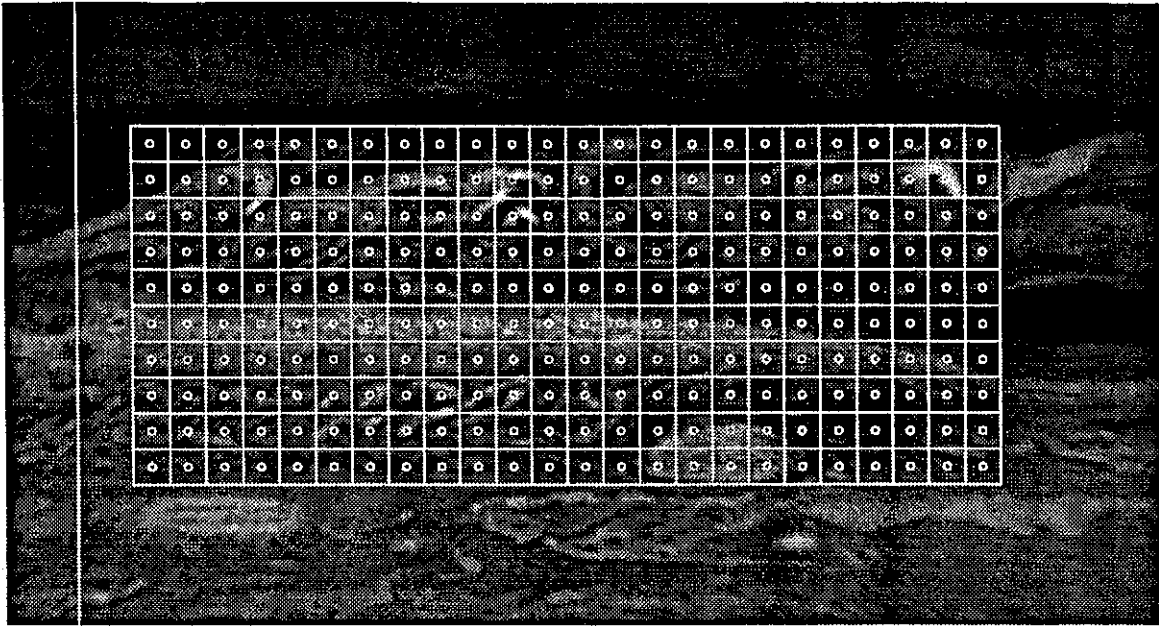


FIG. 16 Initial placement of correlation volumes overlaid on a sub-image of rotation 349 from the "Voyager Time-Lapse, Cylindrical-Projection Jupiter Mosaics." Each square of the grid denotes a correlation volume. The vertical line on the left is a reference line to be carried with the mean zonal velocity of Jupiter (see Fig. 17).

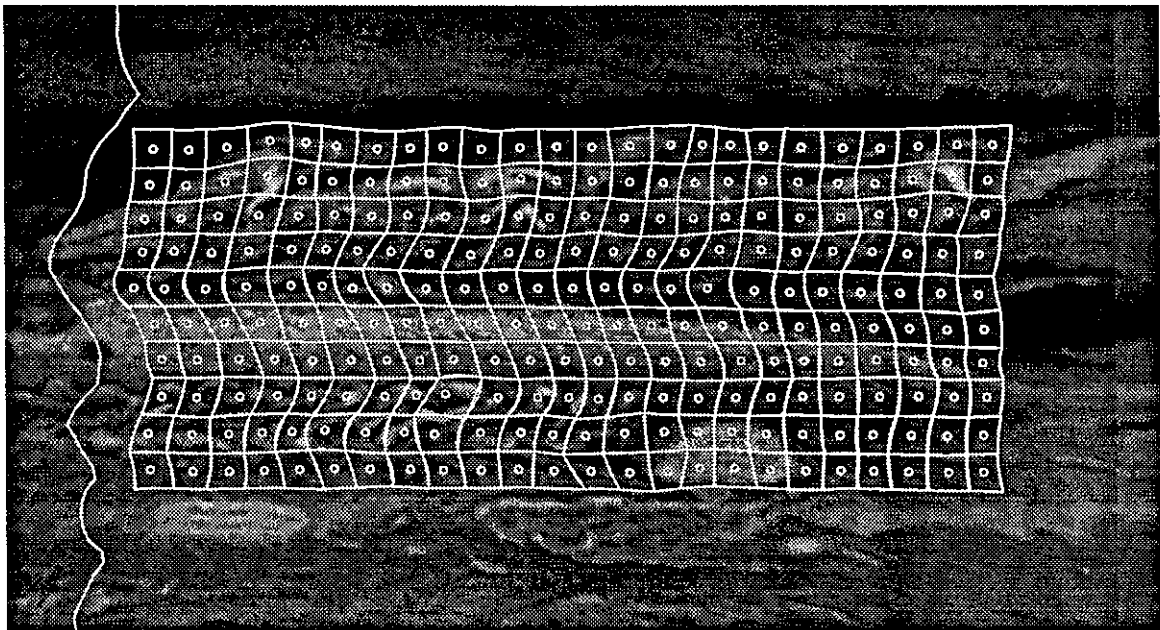


FIG. 17 Deformation of the correlation volumes (see Fig. 16), after one rotation. The line on the left was deformed from the vertical line in Fig. 16 using the mean zonal velocity of Jupiter.

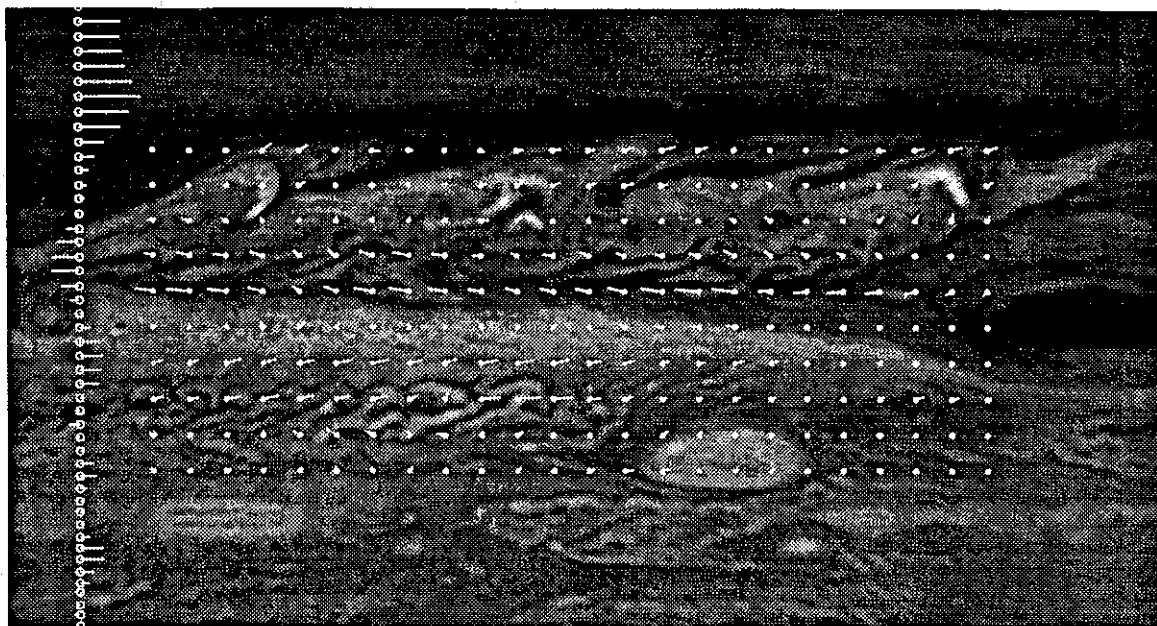


FIG. 18 Displacement of grid control points (centers of correlation volumes) after one rotation. The lines on the left denote the displacement *via* the mean zonal flow of Jupiter.

6. Conclusions

Series expansions of image displacement, in conjunction with a global nonlinear correlation method, can be used to measure fluid velocities, and velocity gradients, from pairs of continuous, convected, scalar images. It is shown that increasing the order of the expansion can improve the accuracy of the results. The proposed method does not require discrete particles and may also be used in situations where there is a natural marker already in the flow, *e.g.*, species concentration can be used to measure velocities in compressible flows. The method is developed for three-dimensional data sets and demonstrated on two-dimensional images of fluid flow.

Acknowledgements

This research was supported by AFOSR Grant Nos. 90-0304 and F49620-92-J-0290, and in a joint contract with M. Gharib of UCSD by DARPA/Navy Grant No. N00014-91-J-1968. We would also like to thank Stewart (Andy) Collins and his group at JPL for their collaboration.

References

- ADRIAN, R. J. [1991] "Particle-imaging techniques for experimental fluid mechanics," *Annu. Rev. Fluid Mech.* **23**, 261-304.
- AVIS, C. C. and COLLINS, S. A. [1983] "Voyager Time-Lapse, Cylindrical-Projection Mosaics," Report D-541, Jet Propulsion Laboratory, Pasadena, CA.
- BINDSCHADLER, R. A. and SCAMBOS, T. A. [1991] "Satellite-Image-Derived Velocity Field of an Antarctic Ice Stream," *Science* **252**, 181-344.
- CANTWELL, B. J. [1992] "Exact solution of a restricted Euler equation for the velocity gradient tensor," *Phys. Fluids A* **4** (4), 782-793.
- DAHM, W. J. A., SOUTHERLAND, K. B. and BUCH, K. A. [1991] "Direct, high resolution, four-dimensional measurements of the fine scale structure of $Sc \gg 1$ molecular mixing in turbulent flows," *Phys. Fluids A* **3**(5, Pt. 2), 1115-1127.
- FALCO, R. E. and CHU, C. C. [1987] "Measurement of two-dimensional fluid dynamic quantities using photochromic grid tracing technique," *SPIE* **814**, 706-710.
- HILDRETH, J. and KOCH, C. [1987] "The Analysis of Visual-Motion - from Computational theory to Neuronal Mechanisms," *Ann. Rev. Neur.* **10**(), 477-533.
- HORN, B. K. P. and SCHUNCK, B. G. [1981] "Determining Optical Flow," *Artificial intelligence* **17**, 185-203.
- HUTCHINSON, J., KOCH, C., LUO, J. and MEAD, C. [1988] "Computing Motion Using Analog and Binary Resistive Networks," *Computer* **21**(3), 52-63.
- LIMAYE, S. S. [1986] "Jupiter: New Estimates of the Mean Zonal Flow at the Cloud Level," *Icarus* **65**, 335-352.
- MCNEIL, S. R., PETERS, W. H. and SUTTON, M. A. [1987] "Estimation of stress intensity factor by digital image correlation," *Engineering Fracture Mechanics* **28**(1), 101-112.
- MILES, R.B., CONNERS, J.J., MARKOVITZ, E.C., HOWARD, P.J. and ROTH, G. J. [1989] "Instantaneous profiles and turbulence statistics of supersonic free shear layers by Raman excitation plus laser-induced electronic fluorescence (Relief velocity tagging of oxygen)," *Exp. in Fluids* **8**, 17-24.
- MURRAY, D. W. and BUXTON, B. F. [1990] *Experiments in the Machine Interpretation of Visual Motion*. (The MIT Press).

PRESS, W. H., FLANNERY, B. P., TEUKOLSKY, A. A. and VETTERLING, W. T. [1986] *Numerical Recipes. The Art of Scientific Computing.* (Cambridge Univ. Press).

ROSENTHAL, S. L. [1990] "Summary of the Special Sessions on Hurricane Hugo 70th Annual Meeting of the American Meteorological Society 4-9 February 1990, Anaheim, California," *Bull. Am. Met. Soc.* 71(9), 1339-1342.

SCHLICHTING, H., (TR. J. KESTIN) [1978] *Boundary-Layer Theory (Seventh Edition,* McGraw-Hill Pub. Co.).

TERZOPOULOS, D. and METAXAS, D. [1991] "Dynamic 3D Models with Local and Global Deformations: Deformable Superquadrics," *IEEE Trans. on Patt. Anal. and Mach. Int.* 13(7), 703-714.

WILLERT, C.E. and GHARIB, M. [1991] "Digital particle image velocimetry," *Exp. in Fluids* 10, 181-193.